Rijksuniversiteit Groningen

Master thesis
December 2, 2022

Noise, spectral, and optical characterisation of far-infrared transition-edge sensor bolometers with frequency-domain multiplexing read-out

kapteyn astronomical institute

SRON
Netherlands Institute for Space Research

Author:
G. F. Huijser
S3177777

Supervisor:
G. de Lange
Second reader:
P. R. Roelfsema

Contents

1 Introduction

Far-infrared (FIR) astronomy is the study of the Universe in the wavelength regime 30 – 300 µm or in the frequency regime 1 – 10 THz. The absorbing properties of Earth's atmosphere make observations of these frequencies challenging and therefore competitive FIR observatories are often balloon-borne (in Earth's stratosphere) or can be found in space. FIR observatories reach the highest sensitivities when they can deliver background-limited performance. That is, when the noise budget of the overall system (optics and electronics) is dominated by external photon shot noise. The photon noise is the Poissonian statistical fluctuation in the incoming photon count from the background sky or the target source. For background-limited performance it is necessary that the thermal radiation, not just the electronic noise level, from the electronics and optics is minimised. In practice, this implies that the optics of the telescope are actively cooled, next to the electronics, which is an operation scheme only feasible in space.

A promising background-limited detection scheme in space-based FIR astronomy is the direct detection[1] of the light with transition-edge sensors (TESs). In short, TESs are cryogenically cooled (< 100 mK) ultra-sensitive thermometers. The working principle relies on the sharp increase in electrical resistance with temperature in the TES bilayer superconducting-to-normal transition region. When FIR photons are absorbed in the TES absorber the TES bilayer changes temperature and it is seen how a relatively minute input optical power (of the order of 10^{-15} watts) causes large excursions in the TES resistance and the (measurable) voltages across it. This makes the TES one of the most sensitive detection units in the field of astronomy (with applications from the millimeter waves to the gamma rays) with typical noise equivalent powers (NEPs) of the order of 10^{-19} – 10^{-18} W/$\sqrt{\text{Hz}}$.

Current research endeavours involve the application of TES devices in arrays of continuously growing size. This requires a thorough understanding of the physical principles behind the workings of the TES and proper application of this knowledge in the design so that the performance of the pixels in the narrow superconducting-to-normal transition state is ensured. Of course, the TES fabrication procedures, system architecture and read-out technology must also experience similar development to meet the demands. The *Netherlands Institute for Space Research* (SRON) is developing TES arrays for FIR and X-ray astronomy.

The FIR performance of TES bolometers has been demonstrated before, but single pixel read-out was considered. In this thesis the spectral and optical performance of TES pixels in a prototype 8×8 TES array[2] are presented. Moreover, the array is read out by use of frequency-domain multiplexing which adds to the novelty of the research. The experiments are performed in a recently developed and flexible optical test-bed configuration housed in a large and new cryostat. Modifications had to be made to the TES array to limit cross-talk effects and, in general, ensure stability of the TES array and the read-out system during the experiments which in turn ensures good experimental results. Unfortunately the array modifications do limit the usable pixel count to four.

One aim of the thesis is to demonstrate an end-to-end noise analysis of the system that reads out the prototype TES array by using frequency-domain multiplexing. The noise sources can be broadly categorised as the read-out noise and detector (TES) noise. The second goal is to qualitatively determine the spectral sensitivity of the pixels for which they were designed. In this case this corresponds to SPICA's short-band: 34 – 60 µm (5.0 – 8.8 THz). Finally the optical noise is studied to quantitatively determine the background-limited performance of the system.

[1] Or, homodyne detection. The counterpart is indirect (heterodyne) detection.
[2] Originally designed and manufactured for the, now cancelled, SPICA mission.

1.1 Thesis outline

Section 2 offers descriptions of superconducting quantum interference devices (SQUIDs), transition-edge sensors (TESs), and multiplexing read-out architectures. The SQUID is a key component in the read-out system and therefore the physics behind the workings of this ultra-sensitive flux-to-voltage transducer are described. This is followed by an explanation on how SQUIDs are suitable for small-signal read-out, by using it together with a flux-locked loop, in particular in the context of multiplexed TES read-out. The TES is central to this work, so the main theory is treated together with a description of TES bolometer applications under negative electrothermal feedback. Various multiplexing read-out schemes are described and compared. Frequency-division multiplexing is discussed in more detail as this is the working principle for the TES array read-out in this thesis.

Section 3 outlines the design of the TES pixel and the prototype array into which they are embedded. Design choices are motivated and compared to other design choices in line with the physical working principles of TES bolometers and optics. The TES array is experimented on in a cryostat-housed optical test-bed which was still in the development stage at the start of this thesis. During this thesis, in the background, the system was gradually improved. Section 4 describes the main features and relevant components of this flexible configuration. Section 5 follows with brief descriptions of the main three experiments that are enabled by the experimental configuration. Sections 6 and 7 provide the complete details of the experiments and also present the results. The former section treats the dark noise characterisation of the read-out system and the four available TES pixels under multiplexed read-out. The latter section concerns the spectral and optical characterisation of the available pixels.

Section 8 analyses in-depth the experimental results obtained in this thesis. Conclusions are drawn and possible implications and future research opportunities and improvements are discussed. Finally, section 9 provides an overview of the work performed in this thesis and outlines the main results.

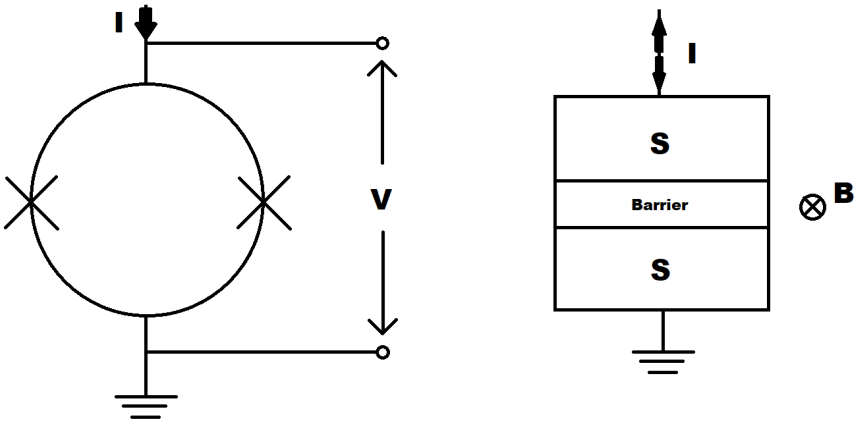

Figure 1: *(**left**) Schematic of a SQUID which consists of a current-carrying superconducting loop with two built-in Josephson junctions as denoted by the two crosses. (**right**) The typical geometry of a Josephson junction with two slabs of superconducting material separated by an electrically isolating barrier. The direction of the magnetic field under working conditions is also shown.*

2 Theoretical background

In this section background knowledge is presented on non-trivial topics that are relevant and may prove useful to the understanding of the various components and phenomena involved in the experiments and the set-up that are described later in this work. Section 2.1 describes superconducting quantum interference devices and their role in astronomical applications and in particular in this work. Generalities and relevant characteristics of transition-edge sensors are treated in section 2.2. The final subject in this section, in section 2.3, concerns the idea behind the simultaneous read-out of multiple signals (in this case from the transition-edge sensors), i.e. multiplexing, and in particular the motivation for opting for a frequency-domain multiplexing architecture including baseband feedback.

2.1 Superconducting quantum interference devices (SQUIDs)

In the schematic in Fig. 1 is shown a superconducting quantum interference device, or SQUID for short. The working principle of such a device is governed by (1) the superconductive properties of the loop and (2) the presence of the two Josephson junctions. Firstly, consider the superconducting loop with the macroscopic wavefunction

$$\Psi(\vec{x},t) = |\Psi(\vec{x},t)| \exp(i\phi(\vec{x},t)) \ . \tag{1}$$

The dominant charge carriers in superconductors are Cooper pairs, as first described by Bardeen, Cooper and Schrieffer in their BCS theory in 1957 [Rohlf 1994]. The sub-dominant quasiparticles in the superconductor, in this case superpositions of holes and electrons, also transport charge. In short, Cooper pairs are created in metals where the temperature has dropped below the critical temperature T_C which depends on the metal. Below T_C, weak interactions between two free electrons and disturbances in the material lattice (phonons) can exist. This quantum mechanical interaction between the two electrons, with the phonon as the gateway, allows the creation of Cooper pairs where the two electrons behave like a single particle with charge -2e. Now, the phase $\phi(\tilde{x}, t)$ in Eq. 1 describes the common center-of-mass (COM) of the Cooper pairs and is well defined [Clarke and Braginski 2004]. Consequently, the Cooper pairs move in a so-called supercurrent through the loop where: no potential difference is created; the Cooper pairs lose no energy in the material via inelastic scattering; and all Cooper pairs share the same COM velocity.

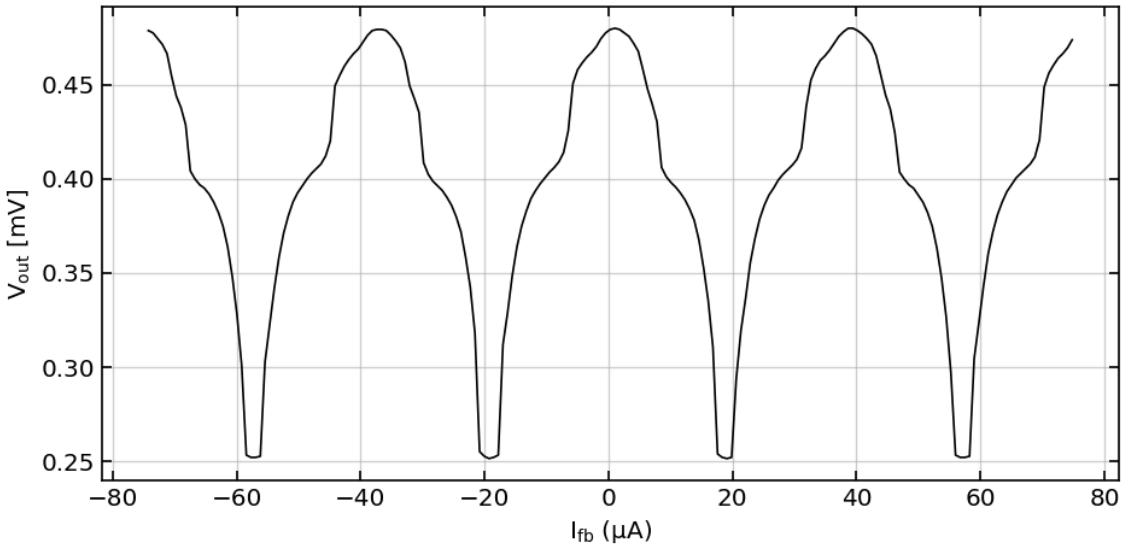

Figure 2: *Periodical response of the SQUID used in this work, operating at 53.5 mK with an applied bias current of 13.0 μA. Shown is the output voltage, V_{out}, versus the current sent through the feedback circuit, I_{fb}. This current is directly proportional to the flux, Φ, through the SQUID. The period of the SQUID response is roughly 40 μA which by construction corresponds to $1 \cdot \Phi_0$. Flux biasing the SQUID will cause the periodical response of the SQUID to shift horizontally, while additional voltage or current biasing causes a shift in the vertical direction in the graph next to changing the shape of the modulation.*

Given these properties and the fact that the wavefunction Ψ must be uniquely defined at any point along the loop, one can derive that the magnetic flux Φ through the loop, for small supercurrent densities, is quantized: $\Phi \approx n\Phi_0$, where n is an integer, in terms of the flux quantum $\Phi_0 = h/2e$ [Clarke and Braginski 2004].

The two Josephson junctions in the SQUID are accompanied by the Josephson tunneling phenomenon which is the quantum tunneling of the Cooper pairs across the barrier. In the case when a sufficiently large bias current is applied to the junction (or, through the loop, see Fig. 1), quasiparticles start to tunnel as well and the potential difference across the SQUID becomes non-zero. This onset occurs when the bias current equals the Josephson junction critical current I_0. This current follows a distinct Fraunhofer pattern as the magnetic flux Φ through the SQUID loop changes, i.e. $I_0 \propto \mathrm{sinc}(\pi\Phi/\Phi_0)$. On top of this slow modulation is superimposed a rapid modulation due to the quantum interference of the wave functions at the Josephson junctions, hence the SQUIDs name.

In the context of astronomical instrumentation, SQUIDs act as ultra-sensitive flux-to-voltage transducers and simultaneously as current amplifiers. SQUIDs have desirable properties when it comes to small-signal (in the μV or μA regime) read-out. As mentioned before, at bias currents above the critical current the voltage across the SQUID is nonzero. In fact, the voltage-flux (V/Φ) behaviour of the SQUID is modulated with a period corresponding to integer numbers of the flux quantum Φ_0, see Fig. 2. Clearly such non-linear behaviour is unwanted and makes for a poor read-out instrument. To resolve this issue the response of the SQUID is linearised with a flux-locked loop (FLL) circuit, more on this in section 2.3. The SQUID is embedded in such a circuit and contains a feedback coil that can provide an opposing magnetic flux Φ_{fb}. This flux is chosen such that the SQUID is locked at a point on the V/Φ curve where the (local) response is linear and the transfer function $\frac{\partial V}{\partial \Phi}$ is the largest — providing optimal sensitivity. Further voltage-biasing is applied to the SQUID to null its output voltage at this point.

With the FLL circuit the SQUID response, amplification factor, and dynamic range are maximized. Note that to effectively measure the output response of the SQUID to an input flux from the input coil (i.e. the device to be read out) one can measure what feedback voltage is required for the feedback loop to null the SQUID's output voltage.

The choice of the SQUID working point via the bias voltage and the bias flux seems arbitrary, however each working point comes with unique SQUID parameters, noise performance and dynamic range. The ideal working point is not straightforward to compute theoretically so in practice the noise performance of the SQUID is analysed across a suitable frequency range for various bias settings and feedback loop voltages.

It is important that the magnetic flux from the input coil does not push the SQUID too far away from its working point where its response is still linear. To avoid non-linearity and distortion in the SQUID response it is, for example, taken that the input signal should not exceed $\pm\Delta\Phi/2$ where $\Delta\Phi$ is taken to be Φ_0/π [Drung et al. 2009]. The input signal frequencies for which the SQUID response is sufficiently clean and linear define the SQUID's dynamic range, which has been demonstrated to reach 10 MHz with fast FLL circuitry [Drung et al. 2009]. In the case of the Athena mission [Ravera et al. 2014] and the cancelled SPICA mission [Roelfsema et al. 2014] the maximum allowed flux excursion was taken to be $\Phi_0/4$ where SQUID performance should be proper at signal frequencies between 1 – 5 MHz [Gottardi et al. 2014a].

Ultra-low noise SQUIDs are the most suitable for reading out the small signals coming from large arrays of transition-edge sensors (TESs) in a frequency-division multiplexing (FDM) read-out system. In the sections 2.2 and 2.3 that follow, the advantage of small-signal read-out with SQUIDs will become more apparent.

2.2 The transition-edge sensor (TES)

2.2.1 Generalities

Shown in Fig. 3 is a transition-edge sensor (TES) bolometer which is able to absorb radiation via an absorber. This component is thermally well connected with a superconducting layer which accepts the heat from the absorber and in turn slowly funnels this energy to the bath via a weak thermal link. In principle a TES can be used under two operation modes: a calorimeter or a bolometer. TES calorimeters are used in high-energy astrophysical applications (X-ray and gamma-ray detection) whereas TES bolometers occupy a niche in radio to far-infrared astronomy. One could narrow down that the distinction comes from the TES' response time or thermal time constant $\tau_{\rm th}$ and its relation to the photon arrival rate described by the time constant τ_γ. The former time constant equals the ratio of the TES heat capacity to the thermal conductance, C/G. Detection of >keV photons with TES' imply $\tau_{\rm th} \gg \tau_\gamma$ while for radio to far-IR detection it holds that $\tau_{\rm th} \ll \tau_\gamma$.

TES devices are, among others, used in the low-frequency regime to study the Cosmic Microwave Background (CMB) which allows a better understanding of the initial conditions of cosmic structure formation and the evolution of its various constituents, and of the inflationary epoch in the earliest days of our universe. One TES bolometer application in CMB research is found in the third generation South Pole Telescope (SPT-3G) which scans a 1500 deg^2 portion of the southern hemisphere and studies the CMB with 16000 TES bolometers operating at microwave wavelengths [Montgomery et al. 2020]. Moreover, the LiteBird space mission is planned for take-off in 2028 and will survey the whole sky between 34 – 448 GHz, mapping the CMB with 4500 on-board TES bolometers [Jaehnig et al. 2020]. Another example of TES application is in the SCUBA-2 instrument on the James Clerk Maxwell telescope which is used for wide-field submillimeter sky surveys for studying the evolution of galaxies, stars, and planets using two 5120 pixel TES arrays at 450 and 850 µm wavelengths [Holland et al. 2013].

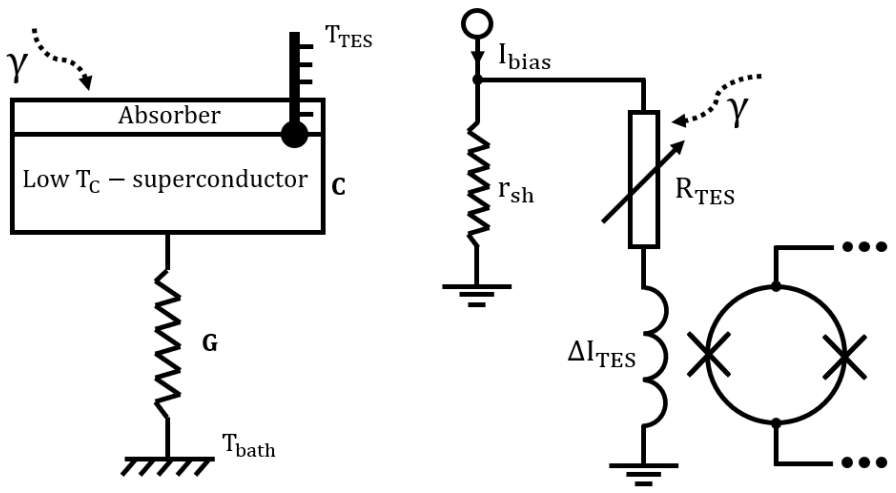

Figure 3: *(**left**) General schematic of a TES bolometer. It is shown how radiation is incident on the bolometer which has an absorber layer and a superconductor layer with a combined heat capacity C. The bolometer with temperature T_{TES} is connected via a resistive path with conductance G to a bath at a temperature $T_{bath} < T_{TES}$. (**right**) For stable operation at maximum sensitivity, the TES is voltage biased into its transition (between the superconductive and the normal-metal state) and the general lay-out of the required circuitry is shown here where a SQUID is used for TES read-out. Voltage bias is achieved with a bias current I_{bias} and a small shunt resistance ($r_{sh} \ll R_{TES}$) connected in parallel with the TES.*

At higher frequencies, in the far-infrared, TES bolometers are applied in the second iteration of the High-resolution Airborne Wide-band Camera (HAWC), called HAWC+, at the Stratospheric Observatory for Infrared Astronomy (SOFIA) [Harper et al. 2018]. HAWC+ is currently armed with two 32×40 TES arrays. As the name suggests, SOFIA is airborne in the Earth's stratosphere, allowing precise (polarization-sensitive) detection of cold, magnetically aligned dust grains in the interstellar medium in the otherwise opaque $40 - 400\,\mu$m range. This offers an accurate probe for studying the interstellar magnetic field which is assumed to significantly affect star formation. At even higher frequencies, TES devices in the form of calorimeters have been used in the field of particle physics and cosmology concerning the determination of the absolute mass scale of the three flavours of neutrinos in the HOLMES experiment [Nucciotti et al. 2018]. Furthermore, TES calorimeter arrays are being developed for the ATHENA/XIFU space mission which will study the hot plasma in galaxy clusters and accretion disk, jets, outflows and winds of black holes in galaxies and supermassive black holes in active galactic nuclei (AGN) in the $1 - 10$ keV range [Barret et al. 2018]. TES calorimeters for high-energy astrophysics are also being developed for the HUBS mission which will study the soft X-ray emission from diffuse and warm-hot media (WHIMs) in the circumgalactic medium, close to galaxies, in an attempt to better understand WHIMs and thereby constraining galaxy evolution models [Cui et al. 2020]. Lastly, at the highest frequencies, the *511 keV gamma-ray CAmera using Micro-calorimeters* (511-CAM) mission is proposed by Shirazi et al. 2022 to study the origin and physical processes involved of the emission of these high-energy gamma rays from the direction of the galactic centre by using TES microcalorimeter arrays as detector technology. The authors claim increases of energy resolution of at least a factor 11 compared to the current state-of-the-art gamma-ray Compton telescopes with germanium-based microcalorimeters.

In this work the TES' form the detection unit of a far-IR receiver system (30 – 300 µm), so TES bolometers are the only operation mode considered here. Then, the following equation describes the temperature change across the TES:

$$\Delta T = \frac{\Phi_\gamma}{G} \frac{1}{1 - i\omega\tau_{th}} \ , \tag{2}$$

for some incoming radiation flux Φ_γ with angular fluctuation frequency ω (for a DC flux: $\omega = 0$). Ideally one would want (1) a fast detector as well as one where (2) the total temperature excursion can be large while at the same time (3) having minimal thermal noise — this thermal fluctuation noise or phonon noise is proportional to $\sqrt{G}$, see Eq. 10. To exploit the three mentioned perks the heat capacity and/or the thermal conductance will have to be minimized and since these parameters are proportional to the operating temperature it holds that: the colder, the better.

Regardless of the operation mode the following coupled differential equations describe the TES response in terms of its state variables $\mathrm{T_{TES}}$ and $\mathrm{I_{TES}}$ (cf. Fig. 3) [Irwin and Hilton 2005]:

$$C\frac{\mathrm{d}T_{TES}}{\mathrm{d}t} = -P_{bath} + P_J + P_{IR} \ ; \tag{3}$$

$$L\frac{\mathrm{d}I_{TES}}{\mathrm{d}t} = V_{TH} - IR_L - IR_{TES}(T_{TES}, I_{TES}) \ . \tag{4}$$

$\mathrm{V_{TH}}$ is the Thévenin equivalent bias voltage applied to the TES, $\mathrm{R_L}$ is any combination of resistances loading the TES circuit, and L is the inductance associated with this circuit. The power flow to the bath, in Eq. 3, is accurately described by a simple power-law model [Irwin and Hilton 2005]:

$$P_{bath} = K(T_{TES}^n - T_{bath}^n) \ , \tag{5}$$

with $K \equiv \frac{G}{nT_{TES}^{n-1}}$ and n describes the strength of the thermal conductance through the resistive path and is a material and geometry dependent property. It is generally assumed that the bath temperature, $\mathrm{T_{bath}}$, is unaffected by the energy flow coming from the TES bolometer, so it is considered a constant factor. $\mathrm{P_{IR}(t)}$ is the radiation power absorbed by the TES at some point in time and $\mathrm{P_J(t)}$ refers to the Joule heating. One can see now through Eqs. 3-5 that the minimisation of both TES capacitance and thermal conductance comes with a trade-off between the aforementioned three perks and the ability for the TES to remain stable in the case of large incident radiation powers, i.e. affecting the dynamic range. In the particular case of voltage biasing as in Fig. 3 the dynamic range may be described by [Irwin and Hilton 2005]:

$$P_{sat} = \left(1 - \frac{R_{TES}}{R_N}\right) P_{bath} \ , \tag{6}$$

which is in terms of the saturation power $\mathrm{P_{sat}}$. It can be seen that large temperature excursions that drive $\mathrm{R_{TES}}$ too high limit the magnitude of radiation power that can be absorbed before the TES is driven to the normal-metal state. In fact, TES bolometers that are too fast because of low heat capacities and high conductances may experience unwanted oscillations in their response at operating points in the superconducting-to-normal transition that correspond to $\mathrm{R_{TES}} < 0.5\mathrm{R_N}$ [Wang et al. 2022], see Fig. 4.

The balance between the radiation power absorbed, $\mathrm{P_{IR}}$, and the Joule power, $\mathrm{P_J}$, in Eq. 3 is involved in the phenomenon of electrothermal feedback (ETF) which can either be positive or negative depending or whether the TES is current or voltage biased, respectively. Generally speaking, a TES must be electrically biased into its transition state between superconductor and normal metal since the operating temperature of the TES is well below its critical temperature, $\mathrm{T_C}$, see Fig. 4.

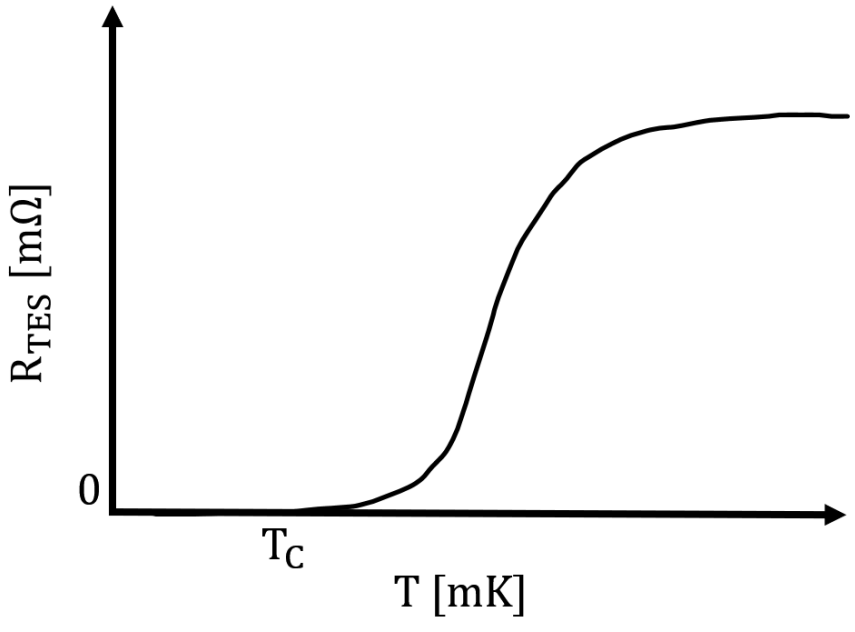

Figure 4: *A sketch showing the typical resistance-temperature behaviour of a TES device. The bottom of the resistance axis is 0 Ω. The transition width near T_C is of the order of 1 mK. The resistance quickly approaches the TES normal resistance, R_N, at temperatures above the critical temperature.*

In this transition the gradient of the electrical resistance is considerable as TES resistance goes from effectively zero to its normal-state value, R_N, in a temperature width of the order of ∼1 milliKelvin (mK). A TES, then, can be considered an ultra-sensitive resistive thermometer. The transition width is affected by several factors [Irwin and Hilton 2005]: T_C non-uniformity across the TES; externally applied magnetic fields; transport current densities in the TES; temperature variations in the TES; and geometry and imperfections of the TES device. In Fig. 4 is shown the resistive thermometer behaviour of the TES where the resistance changes with temperature. The parameter α describes the temperature sensitivity of the TES and is an important parameter concerning TES performance:

$$\alpha = \frac{T}{R}\frac{\partial R}{\partial T} \ . \tag{7}$$

For brevity the TES subscript on the temperature and resistance has been dropped. Similarly, and equally important, and in tandem with Eqs. 3 and 4, we have the current sensitivity:

$$\beta = \frac{I}{R}\frac{\partial R}{\partial I} \ . \tag{8}$$

Eq. 2 implies that incident radiation raises the TES temperature, in turn increasing the electrical resistance. Now, if the TES biasing is performed via a fixed current (constant I_{TES}) and the TES temperature increases due to incident radiation then the Joule heating, $P_J = I^2R$, will further heat the TES to its normal state. In other words, $\frac{\partial P_J}{\partial T} > 0$ and positive ETF causes thermal runaway, disabling the sensitivity of the detector. On the other hand, see Fig. 3, a voltage bias applied to the TES (V_{TES} constant) will cause a decrease in Joule power, $P_J = V^2/R$, and the TES stabilizes itself from an increase in temperature due to the incident radiation, i.e. $\frac{\partial P_J}{\partial T} < 0$. From Eq. 3 we can see that — for small powers, which is the operating condition of TES bolometers — the change in Joule power is equal and opposite to the change in absorbed optical power and so the TES response is linear in the case of negative ETF. Moreover, negative ETF effectively decreases the thermal time constant, τ_{th}, further by a factor $1/\alpha$ which increases the TES dynamic range, but, as mentioned before, may cause oscillations in the TES' response.

It has been described how TES bolometers have high sensitivity due to electrical biasing into the transition state and how these devices have large dynamic ranges due to negative ETF. However, the absolute response of TES bolometers in terms of their current response is small and, at the first stage of read-out, electronics are required that are sensitive, have low noise (i.e. lower than the TES noise), operate at mK temperatures, and can be relatively easily impedance-matched to the TES voltage bias circuit. As shown already in Fig. 3, SQUIDs prove to be advantageous here. Furthermore, SQUIDs allow the read-out of multiple TES pixels simultaneously in a frequency-division multiplexing (FDM) circuit architecture while retaining similar performance to single-pixel read-out but drastically reducing the wire count and the need for additional electronics [Wang et al. 2021], see also section 2.3. This is especially fruitful, necessary even, for kilopixel TES array space-based applications.

In practice, and in contrast with Fig. 3, the superconducting layer consists of a superconductor/normal-metal bilayer. This is because the critical temperature of a superconductor is often not at a favourable temperature to cool down to. Cryo-based cooling or adiabatic demagnetization refrigeration techniques are most efficient and stable at a fixed set of cooling temperatures. So, instead of investing in cooling techniques it is possible to alter the effective critical temperature of the superconductor by directly connecting a metal with a larger critical temperature. This will result in what is called the superconducting proximity effect and allows to tweak the effective TES critical temperature to a favourable value while leaving the transition width largely unaffected [Sadleir et al. 2011]. Moreover, as will be shown in the next section, a positive side-effect is that the dominant thermal fluctuation (phonon) noise of a TES scales with the critical temperature of the bilayer.

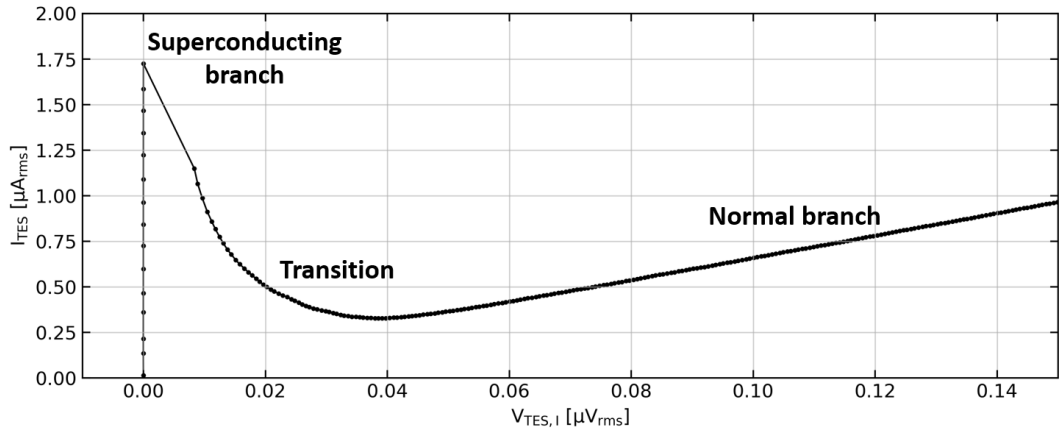

Figure 5: *Calibrated TES current-voltage response showing the current flowing through the TES and the associated potential difference across it. In this example, T_{bath} = 100 mK. The superconducting branch, normal branch, and the transition region are visible. Note that the transition from the superconducting stage to non-zero resistance in the transition region is discontinuous.*

2.2.2 TES characteristics

A celestial object's spectrum can hold a vast amount information from which to derive internal and external properties of and internal and external influences on said object. Likewise, the current response of a TES device to a range of voltages in the form of a current-voltage (I/V) curve allows one to derive various internal and external parameters relevant to the system. A TES device I/V curve is shown in Fig. 5 which is the result of a calibration procedure detailed in section 6.3.1.

It can be seen how for sufficiently small currents the TES remains in the superconducting state and produces no potential difference. At the onset of resistance in the TES bilayer the voltage across the TES becomes nonzero and the current drops as the resistance begins to increase (cf. Fig. 4). The I/V curve reaches a minimum as the TES approaches its critical temperature and the resistance settles towards the bilayer normal resistance, thereafter the response of the TES is Ohmic as characterized by this resistance. In practice, the TES is voltage biased somewhere at or before the I/V curve minimum, depending on the pixel's stability and sensitivity. Of course, I/V curves like in Fig. 5 cannot be measured directly, instead such I/V curves must be recovered from the read-out electronics using knowledge of, and perhaps assumptions on, the total read-out system. After such calibration it is, for example, possible to determine various noise or optical or spectral properties of TES devices.

The intrinsic noise performance of TES bolometers concerns two components: Johnson and phonon (thermal fluctuation) noise. The descriptions of each are as follows, respectively [Wang 2021 & Irwin and Hilton 2005]:

$$NEP_J^2 = \frac{4k_B T_{TES} I_{TES}^2 R_{TES}(1+2\beta)(1+(2\pi f \tau_{th})^2)}{\mathcal{L}^2} \; ; \tag{9}$$

$$NEP_{TFN}^2 = 4\gamma k_B T_C^2 G \; . \tag{10}$$

In Eq. 9, f is the noise frequency, and the dimensionless parameter $\mathcal{L}$ describes the low-frequency loop gain of the TES voltage bias ETF circuit:

$$\mathcal{L} = \frac{\alpha P_J}{G T_{TES}} \; . \tag{11}$$

The term γ in Eq. 10 describes the magnitude of the noise originating from the phonons that travel through the TES to the bath as a consequence of the thermal gradient between them. The value of γ is bounded between 0.5 and 1.

The noise-equivalent powers in Eqs. 9 and 10 may also be expressed in terms of the current noise in $[\mathrm{A}/\sqrt{\mathrm{Hz}}]$ by using the power-to-current responsivity, $s_I(\omega)$, where ω is the signal angular frequency ($\omega = 2\pi f$). For a TES device the responsivity can be written as [Irwin and Hilton 2005]

$$s_I(\omega) = -\frac{1}{I_{TES}R_{TES}}\left[\frac{L}{\tau_{el}R_{TES}\mathcal{L}} + \left(1 - \frac{R_{TH}}{R_{TES}}\right) + i\omega\frac{L\tau_{th}}{R_{TES}\mathcal{L}}\left(\frac{1}{\tau_I} + \frac{1}{\tau_{el}}\right) - \frac{\omega^2\tau_{th}}{\mathcal{L}}\frac{L}{R_{TES}}\right]^{-1} , \quad (12)$$

which contains the bias circuit electrical time constant for zero loop gain ($\mathcal{L} = 0$),

$$\tau_{el} = \frac{L}{R_{TH} + R_{TES}(1+\beta)} , \quad (13)$$

as well as the so-called current-biased thermal time constant,

$$\tau_I = \frac{\tau_{th}}{1-\mathcal{L}} . \quad (14)$$

In the formulations above, $\mathrm{R_{TH}}$ is the Thévenin equivalent of the shunt resistance together with parasitic resistances. Typically, $\mathrm{R_{TH}} \ll \mathrm{R_{TES}}$ and stable TES operation implies $\mathcal{L} \gg 1$. Then, Eq. 12 can be greatly simplified. The zero-frequency responsivity becomes:

$$|s_I(0)| \approx (V_{TES,I})^{-1} , \quad (15)$$

which has the units [A/W]. Note that, under these conditions, the Johnson noise from Eq. 9 in the TES is inferior to the phonon noise from Eq. 10. So, the former may be ignored. With the expression in Eq. 15 and the additional constraint that $\mathrm{T^n_{bath}} \ll \mathrm{T^n_c}$, the phonon current noise can be approximated as[3]

$$I_{TFN} \approx \sqrt{\frac{4k_BT_C}{R_{TES}}} \cdot \sqrt{\gamma n} . \quad (16)$$

Eq. 16 is a way of describing the phonon noise as an equivalent Johnson resistor with the addition of a description of thermal conduction. The final term is typically constrained within $1 \leq \sqrt{\gamma n} \leq 2$.

2.3 Multiplexing read-out architectures

2.3.1 Overview

The idea of multiplexing is the simultaneous read-out of multiple signals coming from multiple detectors via a single wire path, instead of one for each detector. When TES arrays become increasingly larger it also becomes increasingly attractive to implement multiplexing read-out to avoid having complex circuit architectures which become physically large, have increased power consumption, produce more heat (i.e. need more cooling), and may show degraded performance due to cross-talk. In fact, most of the ground-based missions deploying large TES bolometer arrays, mentioned in section 2.2, perform multiplexing read-out. Moreover, size and power consumption are considerably stronger limitations for space-based instrumentation so multiplexing read-out of competitive TES arrays in space is the norm.

[3] This is discussed in more detail in Appendix A.

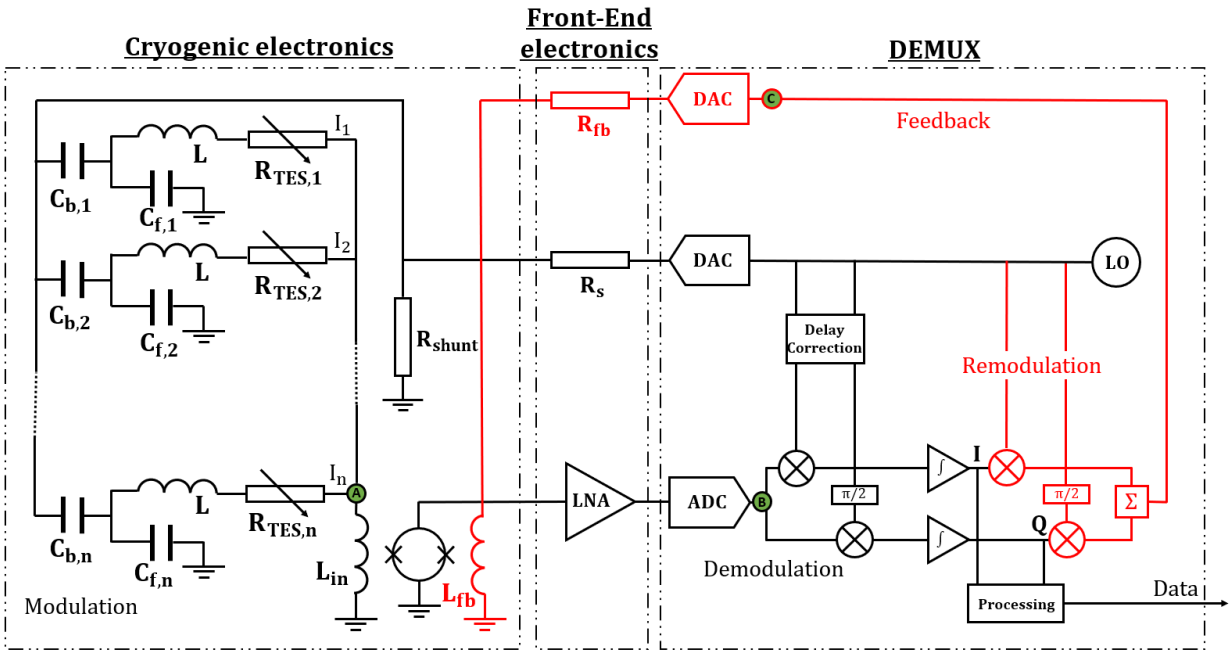

Figure 6: *SRON FDM TES read-out architecture with baseband feedback (BBFB), applicable to this work. In the DEMUX, a local oscillator (LO) in combination with a DAC sends an AC bias signal comb to the TES array. A series resistance R_S describes parasitic resistances of the wires. The shunt resistance $R_{shunt} \ll R_{TES,i}$ (for pixel i; i = 1,...,N) and the bias capacitors, $C_{b,i}$, facilitate the AC voltage bias. The TES pixels in the array are each coupled to an LC circuit characterized by the capacitance $C_{f,i}$ that resonate at a fixed, unique frequency of the AC bias comb. The induced TES currents from optical loading, I_i, modulate the AC bias voltage amplitude at the respective LC resonance frequency. The superimposed signal collects at the point **A** where it is coupled via the input coil to a SQUID amplifier. The signal is further amplified by a room temperature LNA and the amplified, superimposed signal at point **B** is demodulated in the DEMUX board. In-phase (I) and quadrature (Q), i.e. phase, information from the signal is extracted. At the same time, the demodulated signal is modulated again in the DEMUX and fed back to the array and the BBFB circuit (in red). The BBFB circuit sends the output signal at point **C** to the feedback coil. This signal is 180 degrees out of phase with the signal at point **B**. Thus, the SQUID output is nulled and its dynamic range is, effectively, substantially increased. All information, then, about the TES current response to absorbed radiation is captured in the feedback signal required to null the system output. Figure adapted from [Wang 2021].*

In section 2.1 it was introduced how a SQUID allows the implementation of TES detectors in a multiplexing scheme. These schemes may take the following forms: time division multiplexing (TDM); frequency-division multiplexing (FDM); and Walsh code division multiplexing (CDM) [Wang 2021]. TDM requires a SQUID for every TES pixel in the $N \times M$ array where pixels share the same DC bias within a row. Analogous to charge-coupled devices (CCDs) in optical/IR instrumentation, the TES pixels are individually read out where pixels in the same column are read out in parallel. The pixel signals are extracted by rapidly switching the SQUIDs coupled to the pixels on and off. The amount of electrical components and the wire count required are substantial in TDM making the heat load large. Additionally, the signal-to-noise at the read-out is affected by a factor $\sqrt{N}$ due to the number of pixels, N, in a row that are multiplexed. In the CDM scheme, the pixels are also DC biased but the signals from the detectors are encoded so that the signals from all the pixels in a column can be summed and read out simultaneously, thereby deleting the $\sqrt{N}$ penalty on the signal-to-noise. The drawback of this method is the challenging fabrication of SQUIDs compatible with CDM read-out. TDM has been used for ground-based TES array read-out and fairly recently has also been chosen as the read-out architecture for the space-based ATHENA/X-IFU mission[4]. CDM has so far not been deployed in scientific observations with TES arrays as detectors.

2.3.2 Frequency-division multiplexing (FDM) with baseband feedback (BBFB)

Read-out in this work is done in an FDM architecture, see Fig. 6 and its description. The wire count and required electrical components are considerably less compared to TDM and CDM as all pixels are (AC) biased via the same bias line and the read-out is done by a single SQUID amplifier. The dynamic range of this SQUID is vastly improved by employing a baseband feedback (BBFB) circuit that rotates the output signal phase at point **B** by 180° and reroutes this signal back to the SQUID via point **C** to null the system output (red circuit path in Fig. 6). Note that all information of the AC bias amplitude modulation (i.e. optical modulation or baseband modulation) due to the TES current excursions is also captured in the feedback signal required to null the output. The SQUID dynamic range in a circuit architecture like in Fig. 6 is between 1 – 5 MHz. This also dictates the FDM frequency operating range or, in other words, the possible frequency extend of the AC bias comb supplied by the local oscillator (LO). This, in turn, affects the maximum multiplexing factor of the FDM method.

The ability of the LC circuits to isolate their unique resonance frequency from the AC bias comb is quantified by the parameter which is aptly called the quality factor (Q-factor):

$$Q_i \equiv \frac{f_{0,i}}{\Delta f_{0,i}} = \frac{1}{R_{TES,i}} \sqrt{\frac{L}{C_{f,i}}} \,, \tag{17}$$

for pixel i in the array. $\mathrm{f_0}$ is the location of the resonance frequency, as measured, and $\Delta \mathrm{f_0}$ is the respective full-width-at-half-maximum (FWHM). $\mathrm{R_{TES}}$ is the TES resistance, so a TES biased lower in its transition has an LC circuit with a higher Q-factor (see Fig. 4). From Eq. 17 it can also be seen that at lower resonance frequencies in the FDM bandwidth, the Q-factor will drop.

Evidently, a high Q-factor is desired as each pixel would then largely filter out broad-band noise from the array as well as block out cross-talk from adjacent pixels, thus increasing signal-to-noise. Additionally, more high-Q-factor pixels can fit within an FDM bandwidth than TES pixels with lower Q-factors. So, the values of the Q-factor across the array have a large effect on the possible multiplexing factor of an FDM architecture. Consider an array biased at some point $\mathrm{R_{TES}} = \mathrm{xR_N}$ where $0 \leq \mathrm{x} \leq 1$. It is possible to extract the pixel normal resistances from Eq. 17 by scanning the frequency response of the array's LC circuits: $\mathrm{R_{N,i}} = \frac{1}{\mathrm{x_i Q_i}} \sqrt{\frac{\mathrm{L}}{\mathrm{C_{f,i}}}}$.

[4]Thereby changing the initial plan of read-out via FDM.

By design $R_{N,i} = R_N$ but deviations are present due to varying pixel geometries, parasitic effects in the FDM circuit and the tolerances on the capacitances in the LC circuits.

Compared to TDM and CDM, FDM comes with the lowest wire count which allows relatively easy circuit architectures and low thermal loading. Additionally, the LC circuits attached to each pixel are passive and theoretically dissipationless which further lowers the thermal loading. On the other hand, FDM does require sufficiently fast and stable BBFB circuitry to accurately follow and null the output signal of the pixels across the FDM bandwidth. Furthermore, signal-to-noise is optimized only when the lithographic techniques used for the LC circuits is such that the tolerances on the inductance and capacitance are minimal and Q-factors are sufficiently high. Larger FDM bandwidth will result in larger multiplexing factors and the read-out of arrays of increasing size. The FDM bandwidth is limited by the read-out system through the SQUID dynamic range, and the frequency behaviour of the LNA, ADCs and DACs at MHz frequencies [Gottardi and Nagayashi 2021]. Moreover, eddy currents in the normal-metal layer of the TES limit the bandwidth at the higher MHz frequencies. These currents cause thermal dissipation in the TES, affecting the transition curve (Fig. 4) and diminishing detector sensitivity. Careful pixel design has mitigated this effect [Sakai et al. 2018]. A second effect that limits FDM bandwidth is the non-linear Josephson effect [Gottardi et al. 2014b] which also occurs more strongly at the high-end of the FDM bandwidth. The effect by itself is non-dissipative and thus does not affect the signal-to-noise, however, as the name implies, non-linear artifacts will appear on the TES I/V response thus limiting the available options for a suitable operating point. Research on how to minimize the non-linear AC Josephson effect are still on-going by considering the TES bilayer normal resistance, the saturation power, TES dimensions and geometry, and TES-to-absorber coupling. The Josephson effect may be partially minimized by considering materials for TES bilayers with large normal resistances while keeping the low-end of the FDM bandwidth sufficiently high (electrical and engineering constraints) and the saturation power sufficiently high (scientific constraints) [Gottardi et al. 2018].

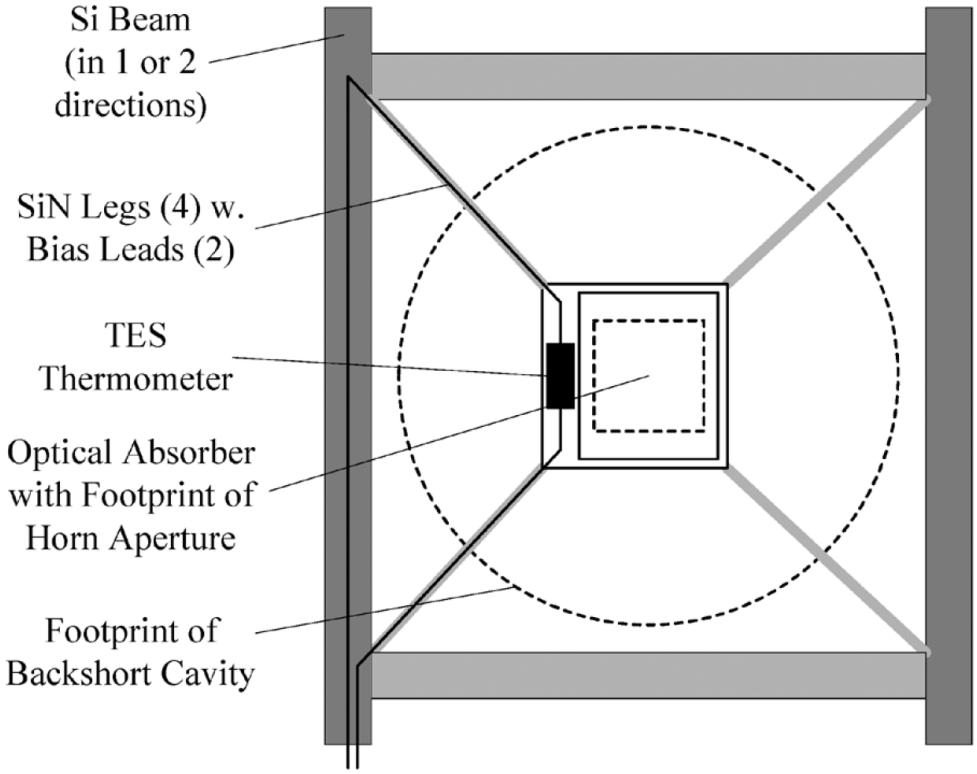

Figure 7: *Schematic design of a TES pixel used in the prototype TES array in this work. Each pixel has four Si_3N_4 (SiN for short) support legs suspending the SiN island in the center. Two of the four legs also carry the bias leads for the TES. Resting on the island is the Ti/Au TES thermometer and a Ta absorbing film. The footprint of the rectangular waveguide horn and that of the hemisphere cavity backshort are shown as well. The pixel design resembles that which was to be used for the SPICA mission. Adapted from [Jackson et al. 2012].*

3 TES pixel and array design

The generalities of TES bolometers and voltage bias ETF circuitry were treated in section 2.2.1. As one can imagine there are various suitable materials and designs that can be used to craft a functioning TES pixel which consists of: the TES thermometer as a superconductor/normal-metal bilayer film; an absorber; a weak thermal connection with the bath; and a cavity backshort. The TES pixels in this work are equipped with a 7 nm thick, 75 µm×75 µm tantalum (Ta) absorber which couples the radiation to the TES thermometer which is a Ti/Au bilayer with a design value of the critical temperature near 110 mK. The TES area is 50 µm×50 µm and the bilayer thickness is 16/65 nm. The normal resistance of the TES bilayer thermometer is 160 mΩ. The TES bolometers are suspended on Si_3N_4 islands via four legs of the same material — see Fig. 7. The islands have a thickness of 500 nm and an area of 224 µm×224 µm, the rectangular support legs have the same thickness, are 360 µm long, and 2 µm in width. The legs rest on a Si beam foundation. Bias leads can be found along two of the four support legs and allow the electrical biasing of the TES thermometer to the optimal operating point, as can be determined from the TES' I/V characteristics. The cavity backshort serves to improve the optical coupling of the TES absorber with the incident radiation, minimising light loss in the process. The cavity backshorts in this work are hemispheres for they are relatively easy to manufacture and provide a good improvement in optical coupling across the 4 – 10 THz range. Theoretical simulations show that pyramidal cavity backshorts and cavity backshorts with sinusoidal profiles provide, on average, even better coupling, yet this hasn't been conclusively demonstrated in practice due to manufacturing difficulties [Bracken et al. 2018].

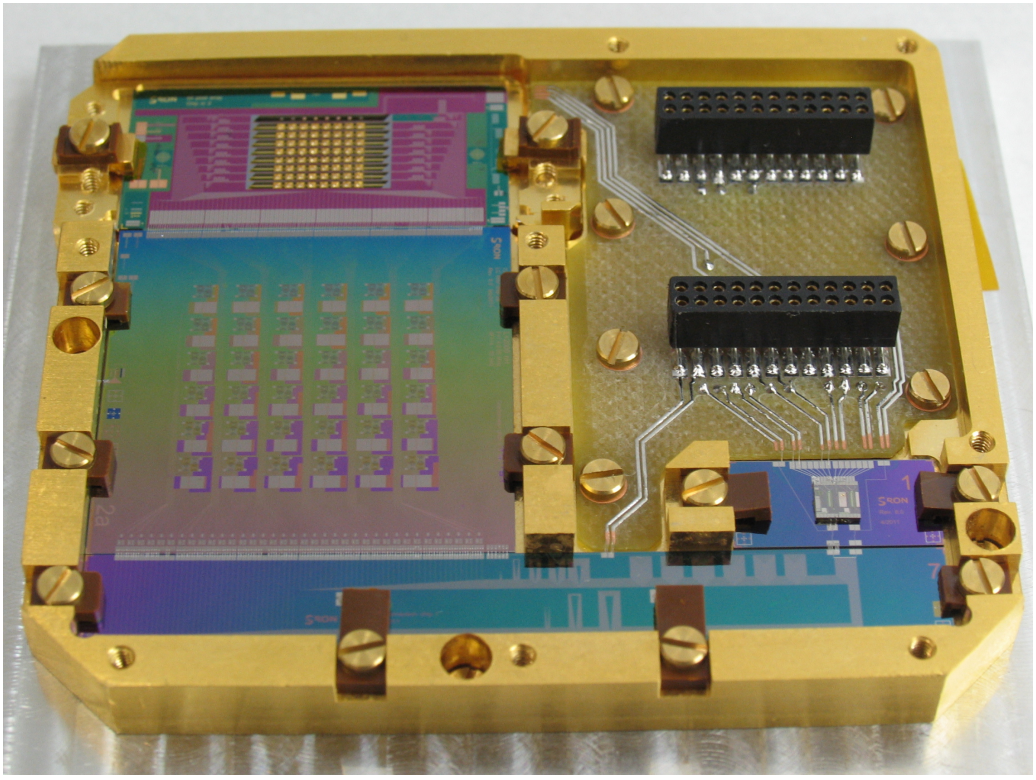

(a)

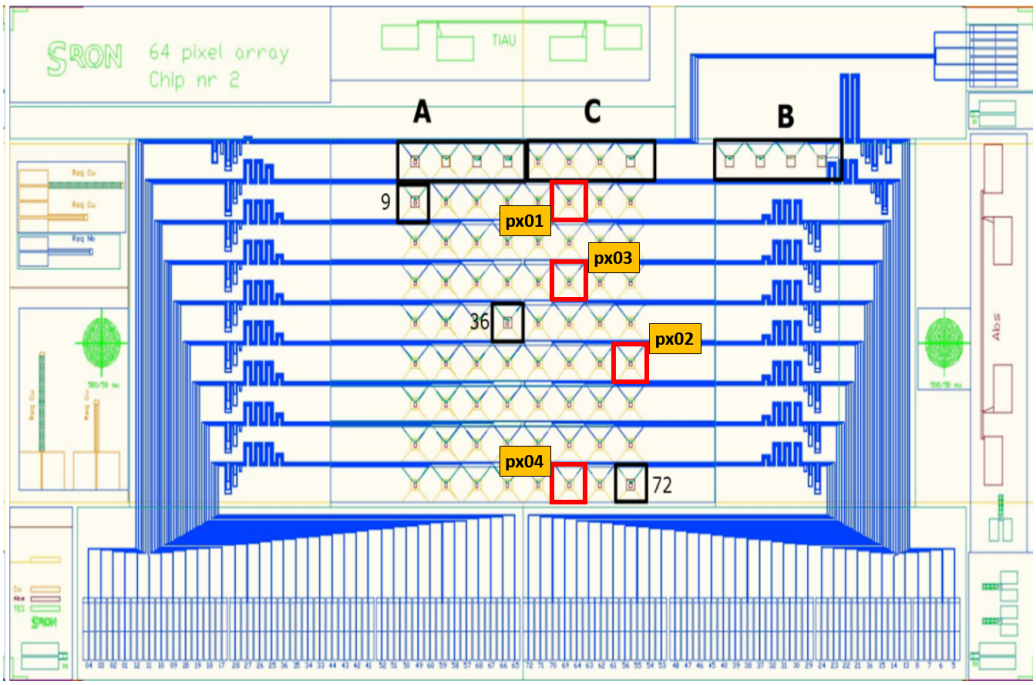

(b)

Figure 8: *(**a**) A photograph showing on the top left the prototype 64-pixel (8×8) TES array experimented on in this work. Behind the array is located the 8×8 hemispherical backshort array and below the TES array is located the associated LC circuitry, see section 2.3. On the top right a connector is present for thermal readings and control and below this is the connector to the read-out SQUID which allows electrical connections to and from the SQUID for biasing and read-out. The SQUID can be seen below the lower connector. The 8×8 square waveguide horn array — for optical coupling — is not shown.* ***Image credit**: M. D. Audley. (**b**) Schematic of the prototype array. Pixels in region A, B, C, and pixel 9, 36, and 72 are dummy resistors. The operational pixels studied in this thesis are labeled px01 to px04.* ***Image credit**: R. den Hartog.*

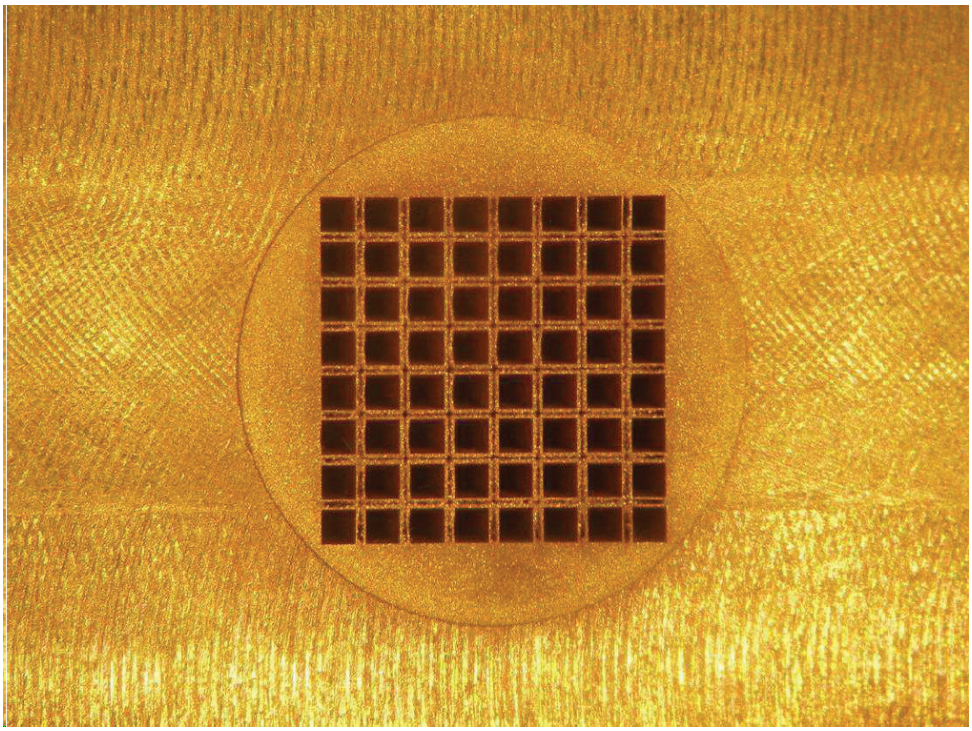

(a)

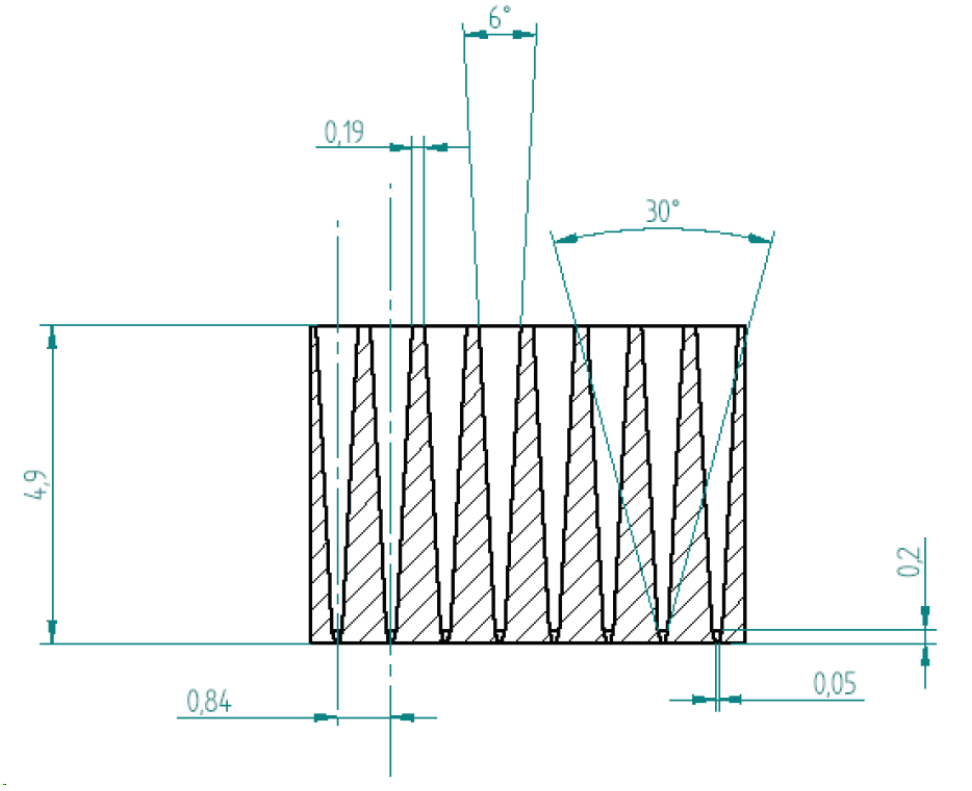

(b)

Figure 9: ***Image credits****: P. Mauskopf, D. Morozov, J. House, S. Withington, D. Goldie, D. Glowacka, P. Khosropanah, M. Ridder, R. Hijmering, J. R. Gao, A. Murphy, N. Trappe, C. O'Sullivan, D. Griffin, T. Lim, and M. Beardsley. (**a**) A photograph of the 8×8 square waveguide horn array that couples the light to the TES array beneath it. The diagonal of the square horn array is approximately 1 cm. (**b**) Schematic of a portion of the square waveguide horn array; showing the important dimensions (in millimeters).*

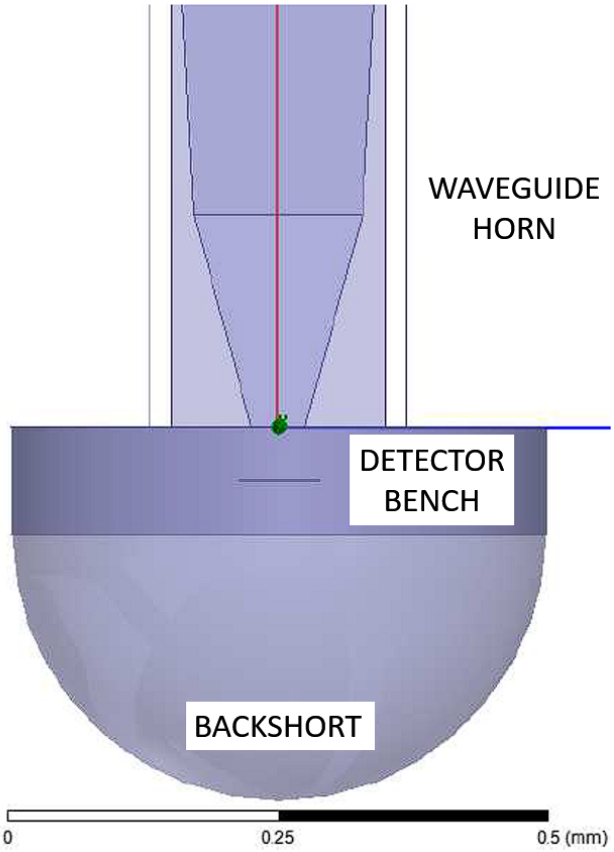

Figure 10: *A model showing a vertical cut of the optical coupling circumstances. The distances between the waveguide horn, detector bench, and backshort cavity are not known exactly in the setup of this thesis.* ***Image credit****: see Fig. 9 credits.*

The prototype TES array used in this work contains 8×8 pixels, see Fig. 8, and was manufactured in 2013 for the, now cancelled, SAFARI/SPICA mission. Each pixel has its own rectangular horn aperture enabled by the waveguide horn array mounted above the TES array, see Fig. 9a. The horns in the array have entrance apertures of 650×650 µm^2, exit apertures of 50×50 µm^2, a length of 4.9 mm, and an opening angle of 6°, as illustrated in Fig. 9b. The centres of the horns are separated by a distance of 840 µm. There is also an array of hemispherical backshorts, mounted behind the TES array; Fig. 10 illustrates the optical coupling circumstances for a single TES pixel with the waveguide horn, detector bench, and the hemispherical backshort.

Alternative designs of the thermal link to the bath have been considered in the past: the ring-type support structure thermal link and the parallel-leg thermal link [Khosropanah et al. 2010]. The latter design requires long SiN legs (around 1800 µm) to achieve low thermal conductance and sufficiently good noise performance (see Eq. 10). Consequently this would lead to arrays with low pixel densities which may violate the required Nyquist sampling, in the far-IR regime, which is of the same order of magnitude as the pixel sizes. Ring-type support geometries, on the other hand, allow compact pixels but then again it has been shown that these structures have large heat capacities and unfavourably low stiffness (prone to deformation).

4 Cryostat optical test-bed description

Measurements for the noise characterisation of the read-out system and optical characterisation of the prototype TES array, that was described in section 3, are performed in the Bluefors XLD-500 cryogen-free dilution refrigerator. Care is taken so that the system is completely RF, mechanically and magnetically isolated. The cryostat is divided in six temperature stages: room temperature, 50 K, 2.74 K, 700 mK, 150 mK, and 20 mK. The final stage contains a light-tight magnetic shield where the cryogenic electronics are housed. Via PID temperature control of a resistive heater (cf. Fig. 8), the temperature in the housing with the cryogenic electronics can in principle be set to any temperature between 40 and 150 mK with nominal 0.5 mK peak-to-peak modulation.

A window attached to the vacuum flange on top of the cryostat allows external optical input for spectral characterisation. In this experiment a Michelson interferometer is connected to this vacuum flange to which a globar optical source is connected which provides a 540 K stable blackbody input. The globar is integrated with an optical chopper to modulate the signal. The optical experimental set-up is elaborated upon in section 7. The external optical input travels down to the final stage via a light-attenuating light pipe. The light intensity attenuation is estimated to be a factor 10^6. The light eventually enters the light cavity in the 20 mK stage where part of the input beam is reflected into the light-tight magnetic shield. The remaining light can be measured by a reference detector, which is located behind the reflective mirror in the light cavity. This reference detector is a TES pixel — suspended in free space — with carefully selected parameters concerning the absorbing film and TES bilayer so that is has a flat spectral response [Audley et al. 2014]. Therefore, the reference detector can be used to measure the radiation entering the light cavity with no spectral biasing. Around half way down the light pipe (in the 2.74 K stage) is located the shutter with the following operation settings: closed, 2 mm, 4 mm, or open (5 mm). This may be used to tweak the optical power entering the light cavity. A cryogenic blackbody source is also present in the light cavity which may be used to internally illuminate the optical test-bed with powers between 3 K to 35 K. The blackbody power can be accurately controlled via PID software.

5 Experiments description

The cryostat and the laboratory that it houses within have been briefly described in section 4. Now, several experiments are performed in this thesis and these are briefly outlined here. The description goes more in-depth in sections 6 and 7.

Firstly, a closed shutter in the lightpipe allows dark measurements for noise characterisation. Recall that the main components of the frequency-domain multiplexing read-out architecture are the demultiplexer, low-noise amplifier, SQUID amplifier, and the TES array. The noise contribution of the demultiplexer and low-noise amplifier is treated first. The SQUID amplifier follows and concludes the read-out noise. Lastly, the thermal fluctuation (phonon) noise from the TES pixels in the array is studied. Recall that the Johnson noise of the pixels is not significant in this experiment. The experimental goal is to conclude whether or not it is possible to show that the dominant noise contribution of our system comes from the first element in the system chain, i.e. the TES array.

Secondly, shutter settings other than 'closed' allow spectral characterisation of the TES array and the reference detector using the chopped signal from the globar and the Michelson interferometer. In particular, interferograms can be measured and used to calculate spectra. From the TES array spectra the sensitivity range of the TES pixels in the far-infrared can be tested. Comparisons with the reference detector spectrum can also be made as well as with simple models of the incident spectrum. The signal-to-noise performance of the TES pixels can be compared.

Lastly, the cryogenic blackbody source in the light cavity allows optical experiments to measure the photon noise that the TES array experiences. The experimental goal is to determine the onset of background-limited performance and show that the system noise after that scales with the square root of the intensity - which is to be expected if photon noise dominates. Simple incident beam modelling will also allow estimations of the pixel optical efficiency to be computed.

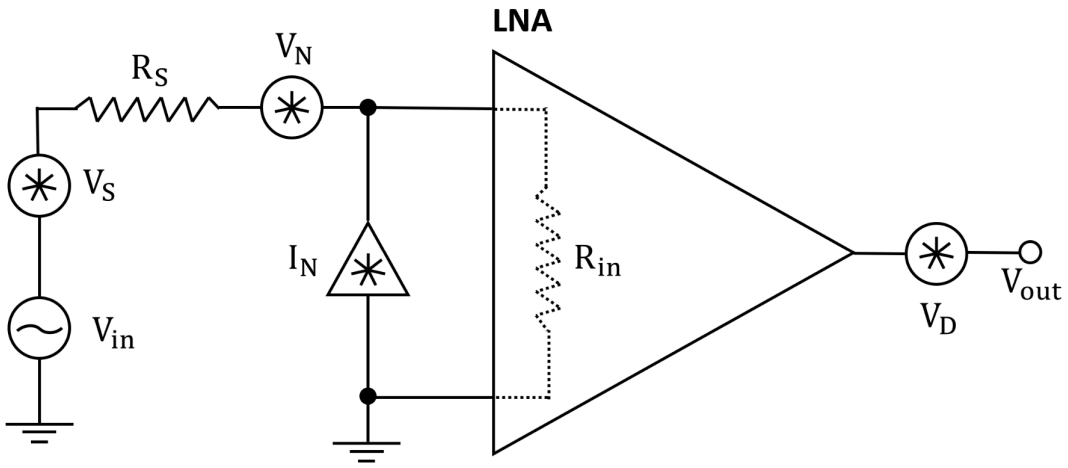

Figure 11: *Circuit model used to estimate the intrinsic noise contributions of the LNA. The model consists of the two zero-impedance noise voltage sources from the LNA, V_N, and the source resistance, V_S, which is due to the thermal noise from the source resistance, R_S. These two voltage sources are in series with the input voltage noise, V_{in}. The infinite-impedance noise current source, I_N, is connected in parallel to the input. The DEMUX adds additional offset voltage noise indicated by V_D. The LNA is modelled as noise free and has a built-in effective and adjustable input impedance R_{in}. The SQUID that is connected to the LNA has a resistance that varies with its operating bias point and input voltage signal. This behaviour can be mimicked with the SQUID disconnected and connecting arbitrary source resistances to the circuit.*

6 System read-out noise characterisation

It was treated how the optical test-bed allows dark measurements for read-out noise characterisation and optical measurements for spectral and photon noise characterisation. Here, the experiments and accompanying results to determine the noise properties of the system are presented.

6.1 The demultiplexer (DEMUX) and low-noise amplifier (LNA)

For the noise characterization of the DEMUX and the LNA, the model in Fig. 11 is used. The noise sources are assumed to be uncorrelated. In general, the output noise, V_{out}, of the system will vary depending on the operating point of the SQUID since its resistance (c.f. the source resistance) changes with bias voltage or current, bias flux, and input flux due to the TES array. However, what will not change are the internal noise contributions of the LNA and DEMUX. This is illustrated by the expression for the output voltage noise from Fig. 11:

$$V_{out}^2 = V_D^2 + G^2 \left[\left(I_N^2 R_s^2 + V_N^2 + 4k_B T_s R_s + 4k_B T_l R_l \right) \left(\frac{R_{in}}{R_{in} + R_s} \right)^2 \right] , \tag{18}$$

where T_S and T_l are the temperatures of the source resistance and the cables, respectively. Note that, with the SQUID replaced by a simple source resistance: $R_l = 0\ \Omega$, and the cable thermal noise contribution is zero. Various scenarios for different SQUID resistances can be simulated by changing the source resistance within the possible range of SQUID resistances. This can be done with simple commercial resistors. The design of the LNA allows various values for the input impedance R_{in}:
37.6 Ω, 48.7 Ω, 74.7 Ω, and 112.6 Ω. Noise spectra of the output noise voltage are calculated (with Hann windowing) from time series measurements of the output voltage. The spectra are averaged in the 1 – 2 MHz range, providing a good estimate of the flat, white noise.

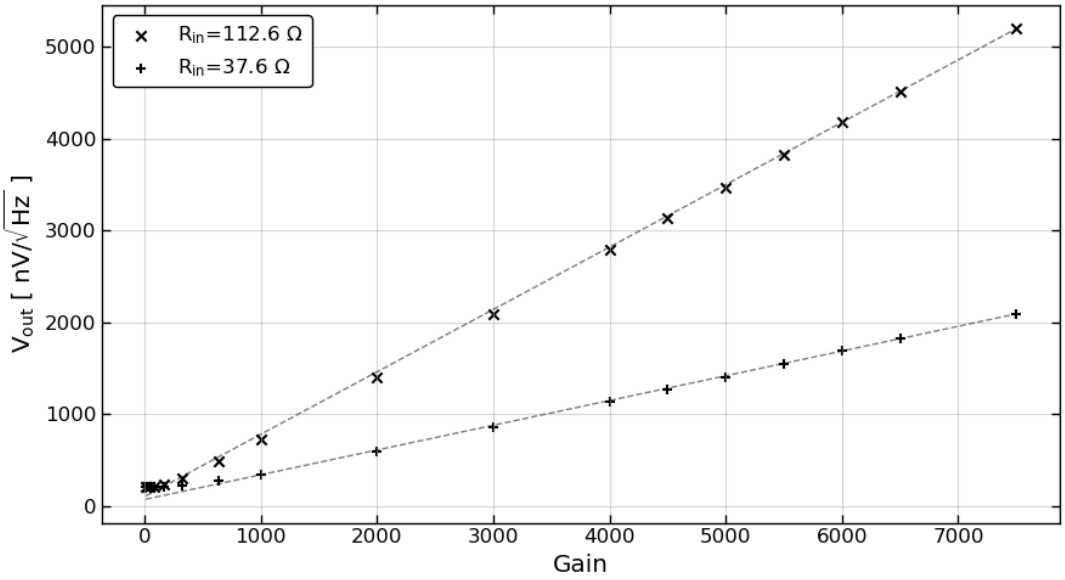

Figure 12: *Average output voltage noise in the 1 – 2 MHz range as a function of LNA gain for the lowest and highest possible input impedance. The dashed line shows, for reference, a straight line through the final three data points at the highest gain. The measurements were performed at room temperature.*

The response linearity of the LNA is readily tested by disconnecting the source resistance and measuring the output voltage noise for various values of the LNA gain, see Fig. 12. The chosen input impedance is either the minimum or maximum possible value. It can be concluded that the response of the LNA and DEMUX is linear for gains above 1000 for all input impedances.

At low gains, from Eq. 18, $V_{out} \approx V_D$ and the DEMUX dominates the read-out noise. Here it is found $V_D \approx 203.5$ nV/$\sqrt{\text{Hz}}$.

Knowing the noise contribution of the DEMUX, the output voltage noise can be measured again with the VNA but now at a fixed gain where the system response is linear and for various source resistances. Fig. 13 shows the room temperature noise measurements at an LNA gain of 5000 for the possible input impedances. Unfortunately, the model in Eq. 18 underestimates the voltage noise for a gain of 5000. This is most likely due to calibration errors of the gain and the input impedances in the software that was used to drive the LNA since the validity of the model has been demonstrated before in similar front-end electronics by SRON, albeit an older iteration [Wang et al. 2020]. It was found (by eye) that a gain of 5556 recovers the maxima in the output voltage noise. Before considering the input impedances, consider that when the system circuit is shorted ($R_S \approx 0\ \Omega$) the voltage noise is roughly

$$V_N \approx \sqrt{\frac{V_{out}^2 - V_D^2}{G^2}}\ . \tag{19}$$

And the LNA voltage noise is independent of the LNA input impedance. The average output voltage noise was measured for the shorted circuit for the possible input impedances, see Fig. 13b. An average output voltage noise of 2040 nV/$\sqrt{\text{Hz}}$ was found, subsequently the LNA voltage noise contribution was determined to be $V_N \approx 365$ pV/$\sqrt{\text{Hz}}$. Now, under open-circuit conditions ($R_S \gg 1$ kΩ) the LNA voltage noise is negligible and then the LNA current noise and input impedance are relatively dominant factors — this is easily seen in Fig. 11.

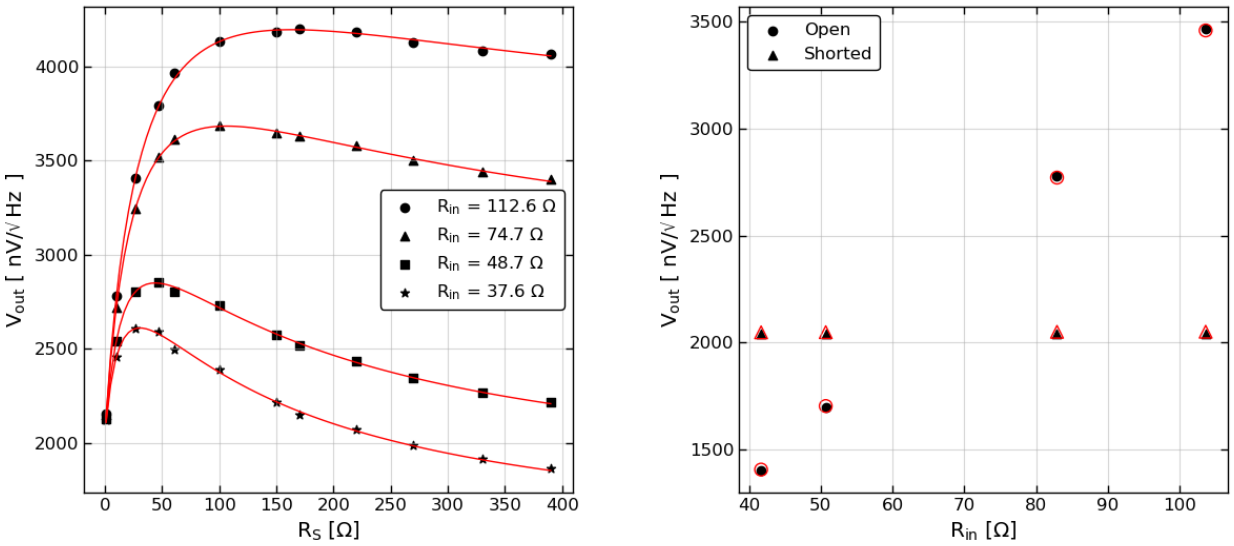

(a) **(b)**

Figure 13: *(**a**) Average output voltage noise measured in the 1 – 2 MHz frequency range for various values of the source resistance and LNA input impedance. Measurements were performed at room temperature with an LNA gain of 5000. The model from Eq. 18 is shown in red with alternative values of the gain and input impedances due to calibration errors in the software. (**b**) Output voltage noise in short-circuit and open-circuit circumstances which were used to find the LNA noise parameters. The red contours around the data points show the match with the model for the alternative gain, alternative input impedances, voltage noise* $V_N = 365\ pV/\sqrt{Hz}$*, and current noise* $I_N = 6.0\ pA/\sqrt{Hz}$*.*

The average output voltage noise was measured by simply disconnecting the source resistance (which in this case was a simple resistor) from the LNA PCB board, see Fig. 13b. These measurements can be matched with the model to find the LNA current noise and input impedance.

It was found that input impedances of approximately 104 Ω, 83 Ω, 50 Ω, and 41 Ω and a LNA current noise $I_N \approx 6.0$ pA/$\sqrt{\text{Hz}}$ produce a model that matches well with the measured data. Thus, the noise contribution of the LNA and DEMUX to the read-out noise has been approximated to acceptable levels when comparing to the previous iteration of the front-end electronics analyzed by Wang et al. 2020.

6.2 SQUID amplifier

As mentioned in section 2.1, the response of a SQUID is generally non-linear when subjected to input signals (in this case magnetic flux fields) of varying magnitude. Therefore it is required to apply a feedback signal to the SQUID which settles and keeps it in the so-called working point where the response is linear. There are possibly several of these working points, but the optimal working point with the best performance — concerning noise and stability — of the SQUID amplifier is found by scanning the 4-D space (I_b, I_{fb}, f, V_{out})[5] while blocking electrical connection to the TES array. Note that the LC filters of the array are still connected in the measurements. The bias current, I_b, through the SQUID covers its current-voltage (I/V) response. I_{fb}, the feedback current, controls the bias flux through the SQUID. The AC output voltage noise, V_{out} (cf. Fig. 11) is measured for signal frequencies f in the frequency range of 1 – 4 MHz. Note that, in this case, the output voltage noise of the SQUID is the input voltage noise, V_{in}, in Fig. 11.

[5]That is, the SQUID bias current, feedback current, signal frequency, and output voltage noise.

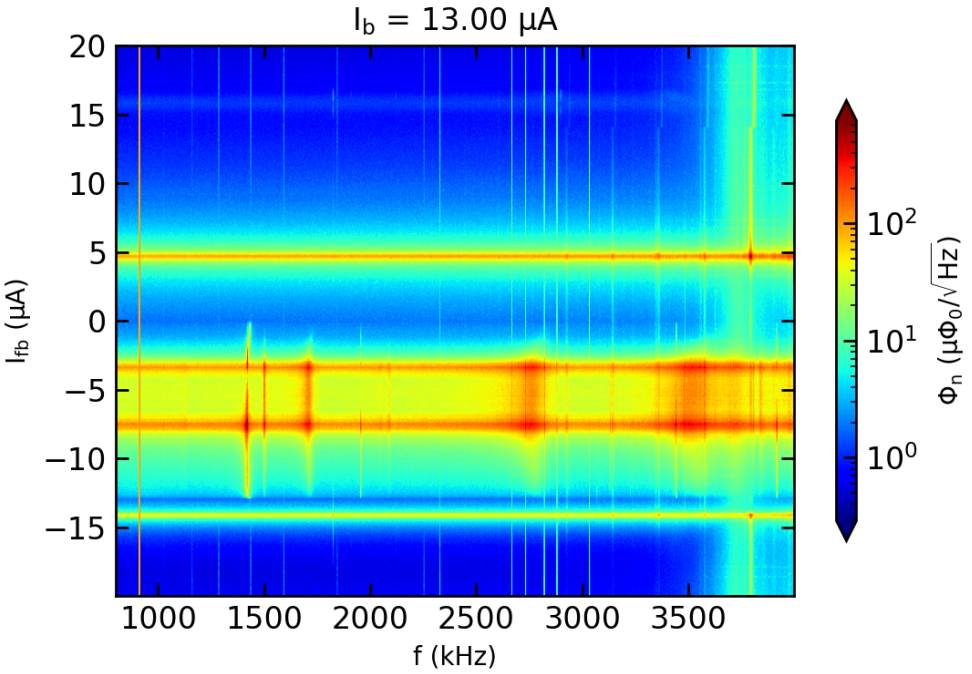

Figure 14: *Flux noise spectrum referred to the input coil with the SQUID amplifier at 53.5 mK for a bias current of 13.0 µA. Note the presence of the 0.01Φ_0 calibration tone at 912 kHz as well as the TES LC filter's resonances.*

The effective current noise referred to the input coil (with inductance L_{in}, see Fig. 6) can be calculated as follows:

$$I_N = M_{in}\Phi_N \ , \tag{20}$$

where M_{in} is the input mutual inductance of the SQUID ($26.4\,\mu A/\Phi_0$) and Φ_N is the intrinsic flux noise in units of $\Phi_0/\sqrt{\text{Hz}}$. The output voltage noise can be readily measured and related to the flux noise at the SQUID input by using a calibration tone sent through the feedback circuit by the DEMUX. The amplitude of this tone is chosen such that it causes a flux excursion in the SQUID corresponding to $0.01\Phi_0$. This amplitude was found by observing the output voltage as a function of tone amplitude. When the single-sided amplitude of the AC calibration tone corresponds to $1\Phi_0$ then the measured output voltage will vary periodically exactly like the SQUID's V/Φ response, see Fig. 2. The amplitude of the tone is then reduced by a factor of 100, giving the right single-sided amplitude where the SQUID response remains, locally, linear. Consequently, the calibration tone relates to the flux in the SQUID with good accuracy. Initial measurements showed clean SQUID noise spectra around 912 kHz, so this was chosen for the tone frequency. Now, the flux noise at the SQUID input is calculated as

$$\Phi_N = \frac{1}{V_{cal}\cdot C} V_{out} \ , \tag{21}$$

with V_{cal} being the voltage single-sided amplitude of the 912 kHz calibration tone. C is a calibration factor in units of $[\Phi_0/\sqrt{\text{Hz}}]$ and can be written as: $C = 100\cdot 2\cdot 2\cdot\sqrt{BW}$; the factor 100 converts the corresponding amplitude to $1\Phi_0$; one factor of two is needed to convert the single-sided amplitude to peak-to-peak and the other to compensate for the Hann window processing of the LNA gain in the fast Fourier transform algorithm; BW is the measurement bandwidth and equals 610.4 Hz[6].

[6]In the noise time series, 2^{16} samples are measured *twice* with a 40 MHz sampling rate, giving a Nyquist sampled spectrum up to 20 MHz.

In the scanning measurements of the (I_b, I_{fb}, f, V_{out})-space, the values of the bias current are varied between 6.00 and 25.00 µA with steps of 0.25 µA, the bias feedback current (i.e. flux) is varied between +20 µA and -20 µA with steps of 0.01 µA. The operating temperature of the SQUID is at 53.5 mK — higher operating temperatures are not expected to affect the noise performance of the SQUID as long as it remains in the superconducting state. As an illustrative example, a slice of the 4-D data cube at 13.00 µA bias current is shown in Fig. 14 with the calculated flux noise from Eq. 21.

The calibration tone is clearly visible at 912 kHz. Several frequency resonances are present in the spectrum which can be attributed to the array's LC circuits. Several broad noise bands at different ranges of the feedback current are also present - the amount and scale of these bands vary with the bias current. The sharp frequency resonances and broad noise bands limit the suitable operating points of a SQUID at a particular bias points.

The noise spectrum in Fig. 14 can be averaged in the 0.919 – 0.931 MHz line-free region to give a robust sample of the average flux noise versus the feedback current. Several other useful quantities can be produced from this line-free region, namely: system voltage noise, V_N; SQUID dynamic resistance, R_{dyn}; and SQUID AC transresistance, R^*_{AC}. The dynamic resistance is calculated from the SQUID I/V response, which may be used to find noise temperatures. The AC transresistance referred to the input coil is derived from the SQUID V/Φ curve and for this the calibration tone is used once more:

$$R^*_{AC} = \frac{V_{cal} \cdot C}{M_{fb}} \cdot \left(\frac{M_{fb}}{M_{in}}\right) \ . \tag{22}$$

In Eq. 22, there is the feedback mutual inductance: M_{fb} (38.3 µA/Φ_0). The feedback coil is indicated in Fig. 18 and the ratio M_{fb}/M_{in} is necessary to refer the AC transresistance *from* this coil *to* the input coil. The AC transresistance is, then, the effective resistance between the input coil and the SQUID, thereby relating current noise in the input coil to voltage noise in the SQUID and vice versa. Large AC transresistances are favoured as they suppress the effects of the voltage noise in the SQUID to magnitude of the current noise in the input coil near the TES array.

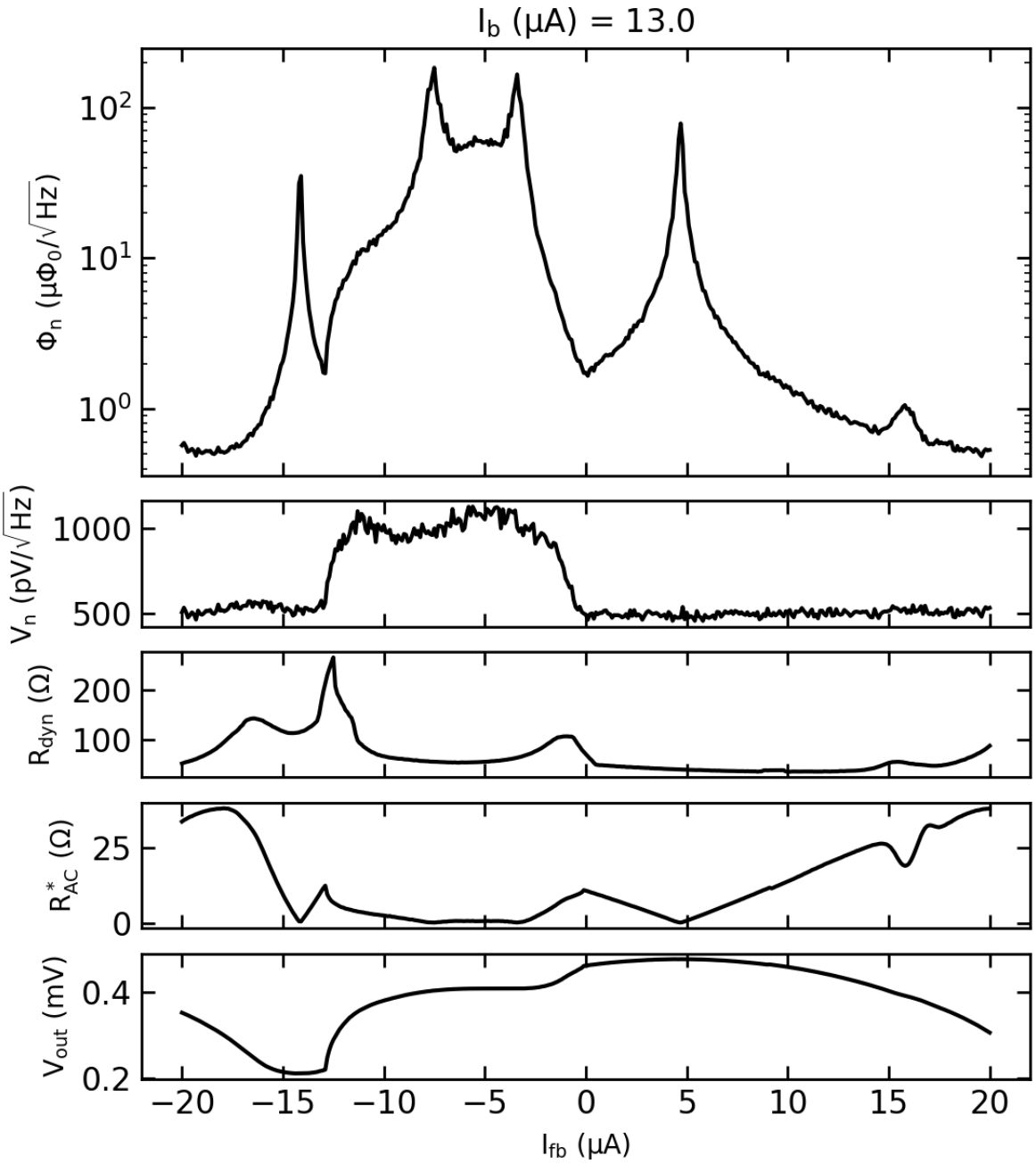

Figure 15: *From the top to the bottom panel: flux noise in the SQUID, voltage noise referred to the LNA input; SQUID dynamic resistance; SQUID AC transresistance referred to the input coil; and, for reference, the V/Φ curve of the SQUID. All the quantities on the vertical axes are averages from the 919 – 939 kHz window. Measurements are performed with the SQUID at 53.5 mK. The bias current applied is 13.0 μA. For the V/Φ curve the LNA settings are: gain = 5000 and R_{in} = 112.6 Ω.*

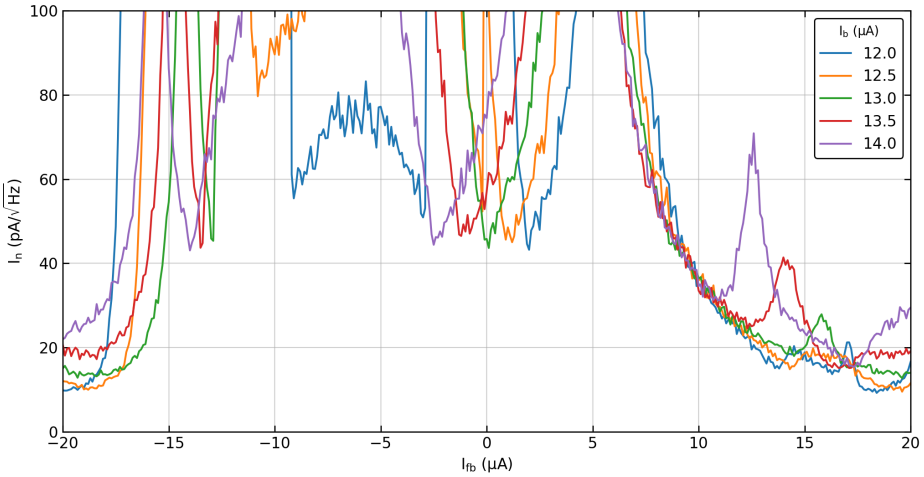

Figure 16: *Current noise referred to the input coil for a range of bias feedback currents and several bias currents near the working point with the lowest noise performance.*

Fig. 15 shows the relevant SQUID quantities, again for a bias current of 13.0 µA. It can be seen how distortion in the SQUIDs V/Φ curve is accompanied with an increase in the system voltage noise and flux noise. Note how the noise bands across the frequency range in the noise spectrum (Fig. 14) reappear in the flux noise of Fig. 15. Ideally the flux noise has a steady baseline — of the level seen at $|I_{fb}| > 18\,\mu A$ — with the noise resonances at fixed feedback currents which depends on the bias current (see [Wang 2021]).

The optimal working point of the SQUID may be found by looking at the current noise curves near the bias point where the current noise has been found to be minimal, see Fig. 16. Note that the DEMUX, LNA, and the SQUID contribute to this current noise. One should consider the minima of current noise and choose the appropriate operating bias current so that the current noise is minimal for a feedback bias current range of at least 1 µA. Less feedback current range around minima limits the dynamic range of the system and its stability. With this in mind the operating point (I_b, I_{fb}) = (13.0, 18.0) µA is chosen for which the total current noise (referred to the input coil) can be read out from Fig. 16 and equals approximately 15.9 pA/$\sqrt{\text{Hz}}$. To elaborate, it has been found that this working point provides a good trade-off between noise performance and SQUID stability under dark conditions and under optical loading conditions. In this case this choice took under the consideration that the optical loading on the TES array causes a slight shift of the working point(s) in the feedback current (horizontal) direction.

In section 6.1 it was found that $I_{N,LNA} \approx 6.0$ pA/$\sqrt{\text{Hz}}$ and $V_{N,LNA} \approx 365$ pV/$\sqrt{\text{Hz}}$. The choice for the SQUID operating point has been motivated before: (I_b, I_{fb}) = (13.0, 18.0) µA. Then, it can be read off from Figs. 15 and 16 that this corresponds to the parameters (I_N, V_N, R_{dyn}, R^*_{AC}) = (15.9 pA/$\sqrt{\text{Hz}}$, 526 pV/$\sqrt{\text{Hz}}$, 50.4 Ω, 33.1 Ω). Note that I_N is consistent with the ratio V_N/R^*_{AC}.

The latter current noise referred to the input coil may be compared by considering the LNA noise parameters and Eq. 18. Consider the *equivalent* noise voltage referred to the input of the amplifier caused by the connected SQUID, from the previously mentioned equation:

$$V_{eq}^2 = I_{N,LNA}^2 R_{dyn}^2 + V_{N,LNA}^2 + 4k_B(T_{SQUID}R_{dyn} + T_l R_l)\ . \tag{23}$$

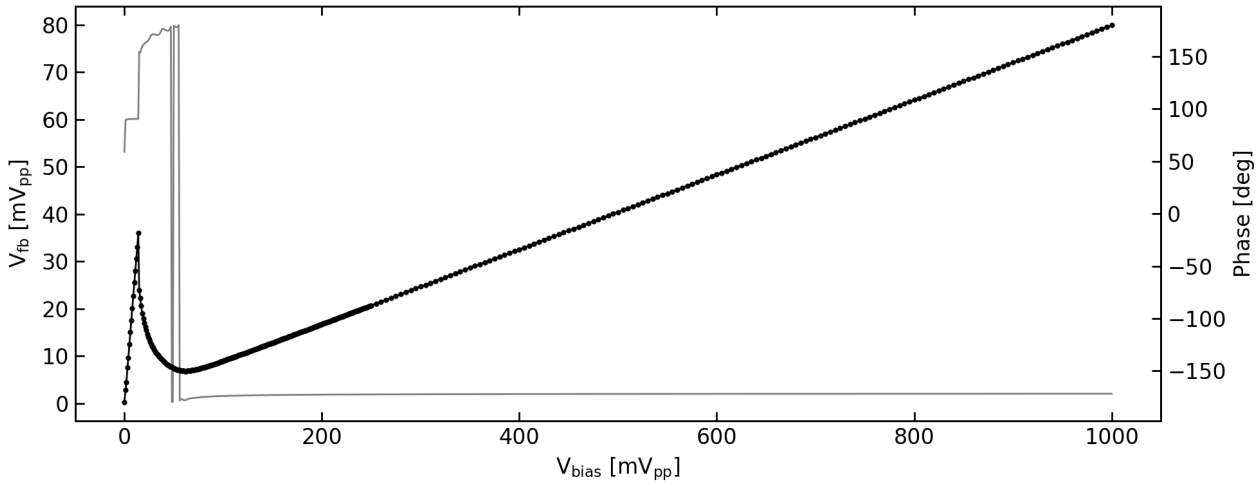

Figure 17: *Measured current-voltage response for pixel 1 with on the left vertical axis the feedback voltage required to null the SQUID output (black curve) and on the right vertical axis the phase (grey curve). The horizontal axis is the AC voltage amplitude applied by the DEMUX. The bath temperature during measurements was at 100 mK. SQUID operating point: (I_b,I_{fb}) = (13.0, 18.0) μA. LNA settings: gain = 5000 and R_{in} = 112.6 Ω.*

Considering the thermal noise from the cables, previous measurements estimate that $R_l \approx 7\ \Omega$ and the average cable temperature is estimated as $T_l \approx 100$ K[7]. Knowing that $T_{SQUID} = 53$ mK it can already be seen that the thermal noise of the SQUID contributes little to this total noise figure and it is the LNA which dominates the read-out noise. It is found that $V_{eq} = 5.1 \times 10^{-10}\ V/\sqrt{Hz}$. The equivalent current noise referred to the input coil is then calculated as V_{eq}/R^*_{AC} which gives $I_{eq} = 16\ pA/\sqrt{Hz}$ and, with the given amount of significant digits, this is consistent with the results from the SQUID analysis experiment.

6.3 TES array

The final component of the system to consider in this section is the TES array. The phonon (thermal fluctuation) NEP that is derived in this section - under the circumstances where no optical loading is present - is compared to the read-out noise found previously. In section 7.2, the system read-out noise and TES phonon noise are compared to the photon noise which enables one to conclude at what signal strengths the system is expected to be background limited.

It was found in previous measurements that the particular design of the TES prototype array gave rise to a high level of cross-talk between TES pixels within bundles of co-planar striplines on the detector chip. This cross-talk influences the calibration performed here but also affects the performance and stability of the pixels. So, it was decided to only use a limited amount of pixels per bundle. This reduces the number of TES devices can be measured from 64 to 12. In fact, 4 pixels are considered in this analysis due to stability issues of the higher-frequency pixels. These 4 pixels are highlighted in Fig. 8b.

The four pixels under consideration respond to the AC bias frequencies 1.161 MHz, 1.286 MHz, 1.437 MHz, and 1.592 MHz — hereafter referred to pixels 1 to 4 or px01 to px04, respectively.

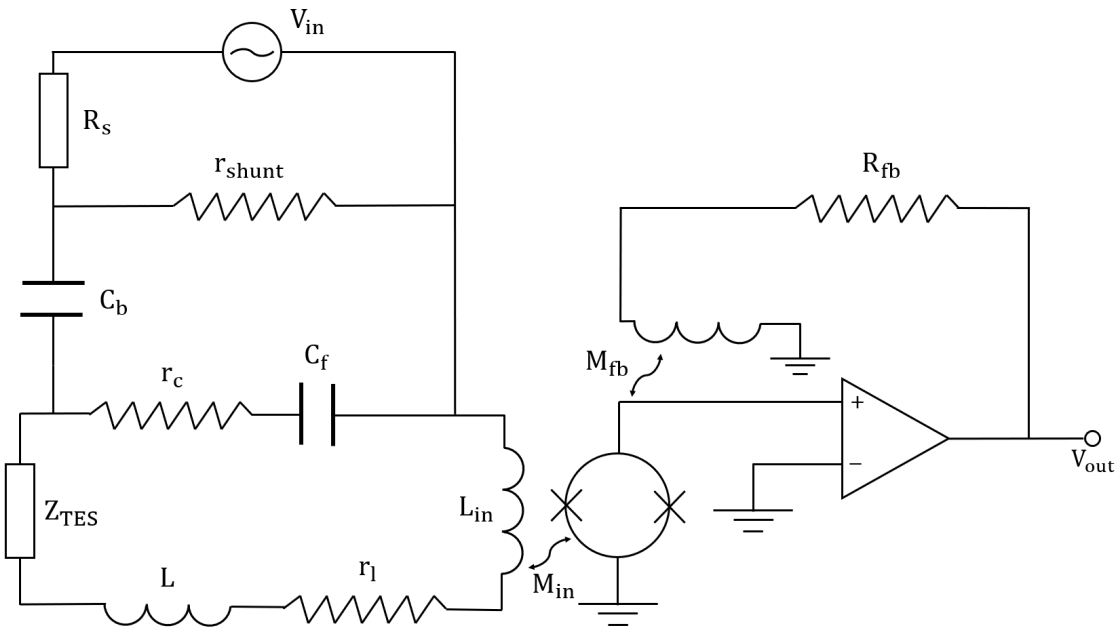

Figure 18: *The AC bias TES readout circuit used to model measured TES I/V response at the LNA output (cf. Fig. 6). V_{in} is the AC bias supplied by the DEMUX; R_S models the bias line resistance and parasitic contributions; $r_{shunt} \ll R_S$ so that the TES operates under negative electrothermal feedback; C_f and L form the pixel LC circuit; r_c and r_l model resistive losses; and M_{fb} and M_{in} are the mutual inductances of the feedback and input coil, respectively.*

6.3.1 Current-voltage calibration

The calibrated TES I/V response in Fig. 5 has been derived in line with the AC read-out circuit in Fig. 18 (cf. Fig. 6). For clarity, some of the circuit details have been left out since they are not relevant to the calibration procedure.

As was mentioned in section 2.3, the feedback voltage (V_{fb}) and its phase (ϕ) are readily measured for any AC bias peak-to-peak amplitude (V_{bias}). Fig. 17 illustrates the effect of parasitic capacitances and resistances on the measured current-voltage response. This effect reveals itself at the superconducting branch where non-zero resistance can be observed, causing a tilt in this branch. Consequently, the normal branch is steeper as the uncalibrated normal resistance is larger than R_N.

From Fig. 18 it can be shown that the in-phase TES current and voltage can be formulated in terms of the circuit parameters of the AC TES read-out circuit:

$$I_{TES,I} = \frac{M_{fb}}{M_{in}} \frac{V_{fb}}{R_{fb}} \ , \tag{24}$$

$$V_{TES,I} = \frac{b_S R_N}{b_r - 1} V_{bias} \cos\phi - \frac{I_{TES,I} R_N}{b_r - 1} \ . \tag{25}$$

Recall that M_{fb} ($38.3\,\mu A/\Phi_0$) is the mutual inductance of the feedback coil and M_{in} ($26.4\,\mu A/\Phi_0$) is the mutual inductance of the input coil. Furthermore, recall that for each pixel in the prototype array under study, the normal resistance: $R_N = 160$ mΩ. $b_r = b_s/b_N$ which is the ratio of the slope of the superconducting branch over the slope of the normal branch.

[7] By considering the six portions of the total cable length in the six cryostat temperature stages.

The normal branch and superconducting branch slopes are given by

$$b_N \equiv \left.\frac{I_{TES,I}}{V_{bias}\cos\phi}\right|_N = \frac{r_{shunt}}{R_S + r_{shunt}}\frac{C_b}{C + C_b}\frac{1}{r + R_N} \; ; \tag{26}$$

$$b_S \equiv \left.\frac{I_{TES,I}}{V_{bias}\cos\phi}\right|_S = \frac{r_{shunt}}{R_S + r_{shunt}}\frac{C_b}{C + C_b}\frac{1}{r} \; , \tag{27}$$

where the terms in the second equality are evaluated at either the normal or superconducting branch. Both expressions contain one resistive voltage divider term and one capacitive voltage divider term. Parasitic effects on the measured current-voltage response are captured in the expression of r:

$$r \equiv r_l + \frac{r_c + r_{shunt}(C_b/C)^2}{(1 + C_b/C)^2} \; . \tag{28}$$

It can be seen that is not required to know the details of the parasitic effects of C_b, r_L, and r_C on the measured voltages to properly calibrate the measurements since these can effectively be incorporated through the slopes of the superconducting and normal branch.

Essential for optical calibration is the power plateau that can be calculated from the TES I/V response. This curve describes the power dissipated in the TES as a function of its resistance. The plateau is rather straight-forward to produce knowing that $P_{TES} = V_{TES,I}I_{TES,I}$ and $R_{TES} = V_{TES,I}/I_{TES,I}$. Comparing the power plateaus of the TES, at the same bath temperature, for different magnitudes of optical loading to the power plateau for which no optical loading was present, allows an absolute calibration of the absorbed radiation power. This assumes that the TES response is linear, but this has already been established in section 2.2.

6.3.2 TES phonon noise

Changing the bath temperature in the TES array will affect the magnitude of the power flow — originating from the thermal noise — from the TES island to the bath. Consequently, its dynamic range is decreased. In other words, the effective saturation power decreases. By measuring this saturation power for various bath temperatures from the power plateaus one can determine from Eq. 5 the TES critical temperature (T_C), thermal conductance exponent (n), and the thermal conductance (G). Fig. 19 shows the calibrated current-voltage response of pixel 1 for different bath temperatures with the corresponding power plateaus. Strictly speaking the plateaus are not flat due to the finite transition width in Fig. 4. In Fig. 19 it can be seen how the TES is driven effectively to the normal state as bath temperatures start to approach 105 mK. Correspondingly the effective saturation power tends to zero. Each black star in Fig. 19 corresponds to the TES I/V minimum, which, depending on the circumstances, may be a suitable operating point. Evidently, more and more biasing is needed to drive the TES to the same point in the transition region for lower bath temperatures. The I/V minimum starts to corresponds to lower resistances as the bath temperature increases until the point where small voltage changes may already drive the TES normal.

The effective saturation powers are extracted from the power plateaus at a resistance of 0.5 R/R_N. The model in Eq. 5 is seen fitted to the saturation powers versus bath temperature in Fig. 20. Unfortunately, malfunctioning of the cryostat degraded its cooling capabilities and because of this it was no longer possible for pixels 2 to 4 to cool below 65 mK. Consequently, the least-squares minimization returns larger uncertainties for the most likely parameter values in these cases. See Tab. 1 for the least-squares fitting results. The derived thermal conductances and phonon NEPs are summarized in Tab. 2.

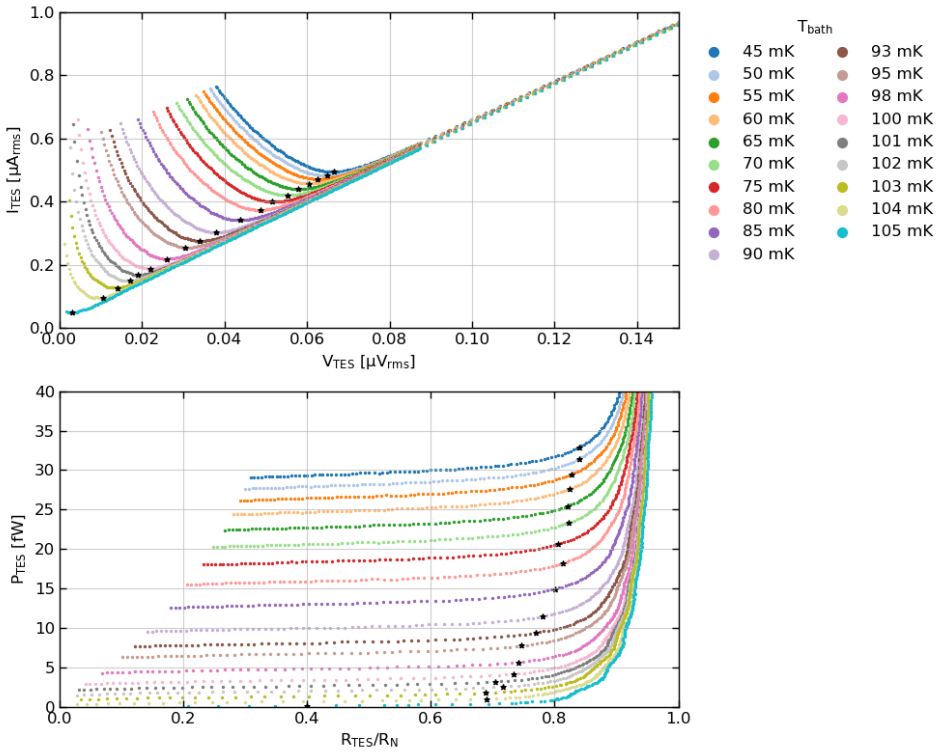

Figure 19: *Pixel 1 current-voltage responses and power plateaus for various bath temperatures. The black stars indicate the I/V minima and the corresponding location on the power plateaus. SQUID operating point:* $(I_b, I_{fb}) = (13.0, 18.0)\ \mu A$. *LNA settings: gain = 5000 and* $R_{in} = 112.6\ \Omega$. *Normal resistance:* $R_N = 160\ m\Omega$.

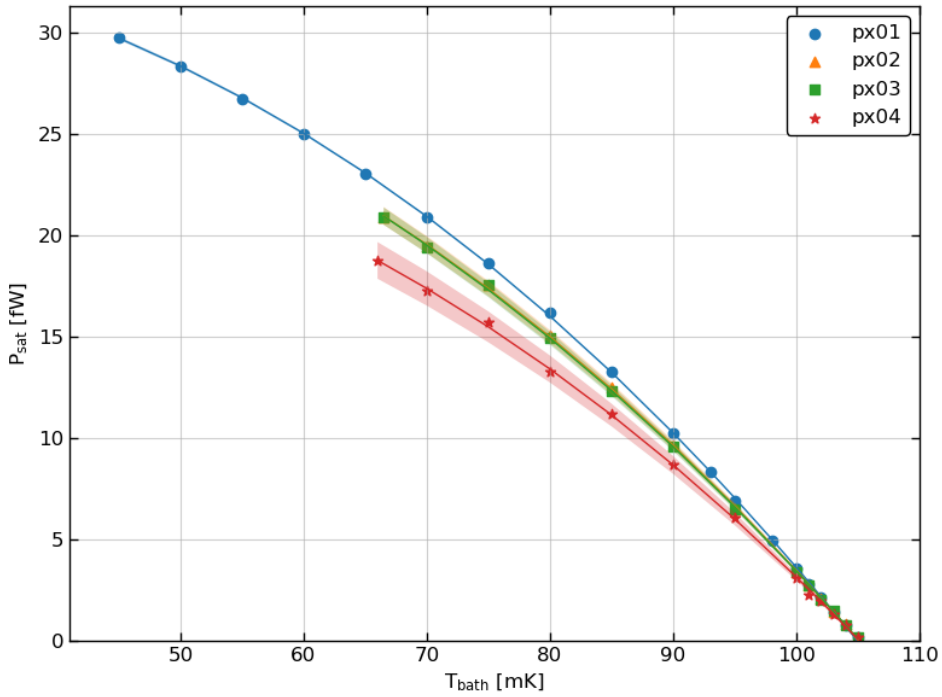

Figure 20: *Effective saturation powers at 50% R/R_N as a function of the bath temperature for pixels 1 to 4. The model in Eq. 5 is seen fitted to the data points. SQUID operating point:* $(I_b, I_{fb}) = (13.0, 18.0)\ \mu A$. *LNA settings: gain = 5000 and* $R_{in} = 112.6\ \Omega$. *Normal resistance:* $R_N = 160\ m\Omega$.

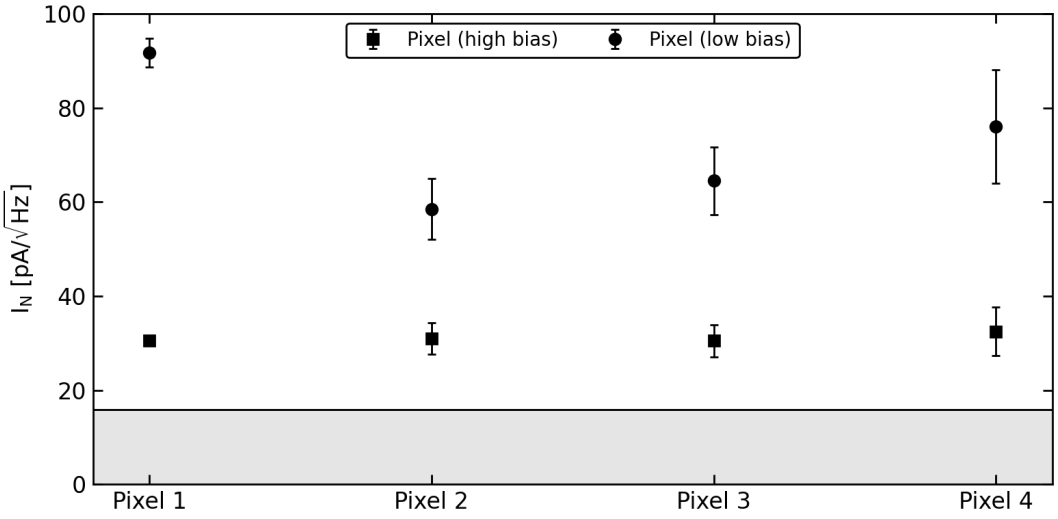

Figure 21: *Phonon noise of pixels 1 to 4 at high and low bias points, note that these noise values assume* $\sqrt{\gamma} = 1$. *The boundary of the system read-out noise (15.9 pA/*$\sqrt{Hz}$*) is indicated. For the TES pixels that are biased low in the transition the ratio* R/R_N *equals 11%, 25%, 20%, and 16% for pixels 1 to 4, respectively. These are the setpoints for the spectral measurements in section 7.1. For the TES pixels that are biased high in the transition the ratio* R/R_N *equals 73%, 71%, 71%, and 67% for pixels 1 to 4, respectively. The pixel bath temperature is 100 mK in all cases. SQUID operating point: (*I_b*,* I_{fb}*) = (13.0, 18.0)* μA*. LNA settings: gain = 5000 and* R_{in} *= 112.6* Ω*. Normal resistance:* $R_N = 160$ $m\Omega$*.*

Table 1: *Best fit parameters of Eq. 5 to the data in Fig. 20. The* 1σ *uncertainties are given in brackets.*

Pixel	K [pW/K^n]	n	T_C [mK]
1	5.78 (0.30)	2.27 (0.02)	105 (1)
2	5.73 (0.94)	2.30 (0.08)	105 (1)
3	4.88 (0.80)	2.22 (0.08)	105 (1)
4	6.18 (1.47)	2.40 (0.11)	105 (1)

It is convenient to express the phonon NEP in current noise referred to the input coil using the zero-frequency power-to-current responsivity, $s_I(0)$, from Eq. 15. In section 7.1, during spectral characterisation, pixels 1 to 4 are biased so that the in-phase voltages across the TES are[8]: 7.37 nV, 11.2 nV, 10.0 nV, and 8.19 nV, respectively. The approximate zero-frequency power-to-current responsivity is readily calculated from Eq. 15. In turn, the phonon current noises referred to the input coil can be computed and these are shown in Tab. 2.

[8]As derived from Fig. 19 and Figs. 31-33.

Table 2: *Values of the thermal conductances from the best-fit parameters of Tab. 1, the phonon noises, and the phonon current noises using the responsivities of the pixels at the bias points corresponding to the spectral measurements in section 7.1. These bias points correspond to the following voltages across the TES: 7.37 nV, 11.2 nV, 10.0 nV, and 8.19 nV for pixels 1 to 4 respectively. Note that $0 \leq \gamma \leq 1$.*

Pixel	G [fW/mK]	$NEP_{TFN}/\sqrt{\gamma}$ [aW/$\sqrt{Hz}$]	$I_{TFN}/\sqrt{\gamma}$ [pA/$\sqrt{Hz}$]
1	0.752 (0.051)	0.676 (0.023)	91.7 (3.1)
2	0.704 (0.157)	0.655 (0.073)	58.5 (6.5)
3	0.693 (0.153)	0.650 (0.072)	64.5 (7.2)
4	0.636 (0.205)	0.623 (0.100)	76.0 (12.1)

In comparison with the current noises from Tab. 2, consider the approximate phonon current noise at the boundary of suitable TES operation, i.e. at the I/V minima — this is the point where higher biasing will lead to significant decreases in sensitivity. From the I/V measurements at 100 mK it can be derived that the minima correspond to (V_{TES}, R/R_N) = (22 nV, 73%), (21 nV, 71%), (21 nV, 71%), and (19 nV, 67%), respectively for pixels 1 to 4. What follows is that the phonon current noises of the pixels are similar, i.e. the current noises fall in the range $(30.6 - 32.5)/\sqrt{\gamma}$ pA/$\sqrt{Hz}$ with a maximum uncertainty from pixel 4 of $5.2/\sqrt{\gamma}$ pA/$\sqrt{Hz}$.

6.4 Total read-out noise

It can be concluded that, for all suitable operating points, the TES thermal fluctuation (phonon) noise is higher than the 15.9 pA/$\sqrt{Hz}$ read-out current noise determined in the previous sections — keeping into account that $0.7 \leq \sqrt{\gamma} \leq 1$. It is expected, then, that the TES noise favourably dominates the system read-out noise. This is also illustrated in Fig. 21.

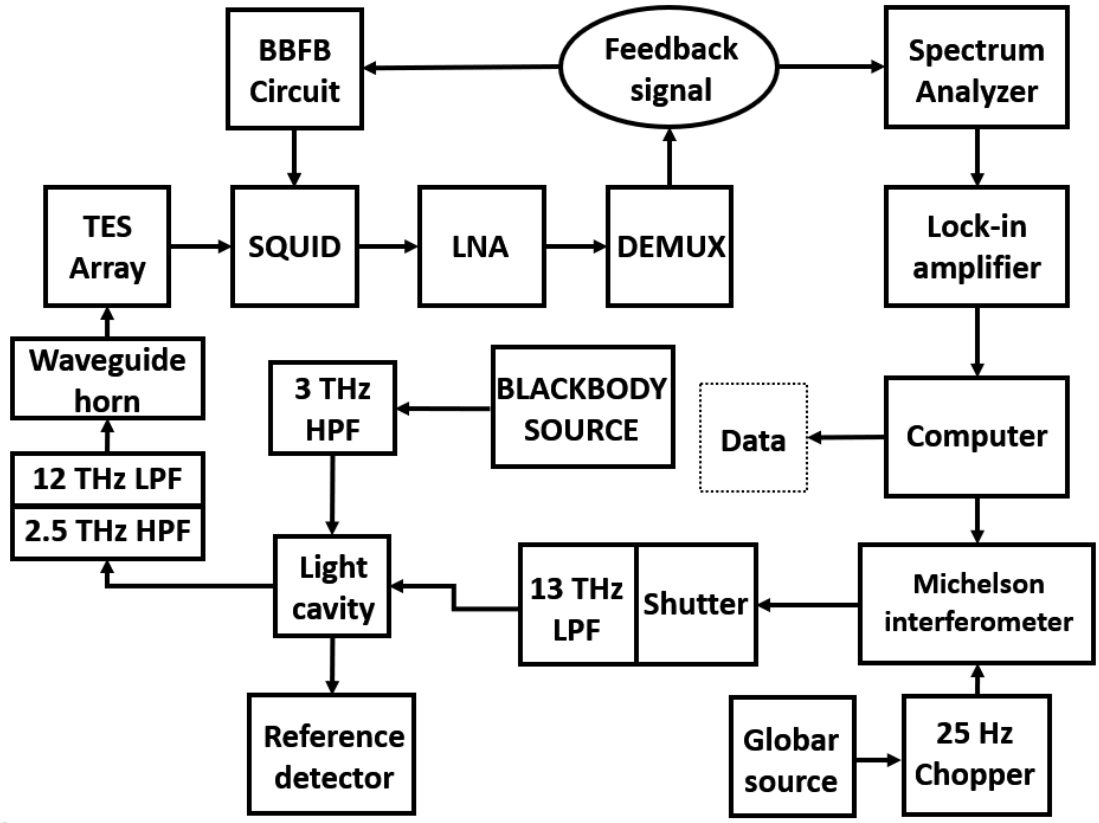

Figure 22: *Block diagram showing the various components involved in the optical characterisation of the TES array. LPF and HPF refer to low-pass and high-pass optical filters, respectively. The globar source emits as a 540 K blackbody. The Michelson interferometer outside the cryostat is operating under 1 millibar pressure conditions.*

7 TES array optical characterisation

The optical characterization of the TES array is performed with the setup illustrated schematically in Fig. 22. A 540 K globar light source is chopped at a frequency of 25 Hz. So, the power is modulated between 540 K and 295 K (room temperature). Central to the spectral characterization in this set-up is the Michelson interferometer which contains a 6 µm-thick mylar beamsplitter and is operated around 1 millibar pressure to minimise atmospheric effects. The interferometer is used in step-scan mode for measuring interferograms. The optical signal travels through the attenuating light pipe and passes the shutter in the 2.74 K stage which is set to *open* implying an exit aperture of 5 mm. The reference detector in the situated in the light cavity and has its own LC filter and read-out SQUID amplifier. In the experiment, the output AC feedback signal from the TES array is coupled to a spectrum analyser. As described by Eq. 17, the feedback voltage of a pixel will have a non-zero width around the design resonance frequency value so the spectrum analyzer is used to lock-in on the peak value of the AC feedback voltage spectrum. The lock-in amplifier, then, measures the 25 Hz peak-to-peak modulation due to the optical loading from the globar at the resonance frequency.

This experiment also includes step-scan measurements with the reference TES detector in the light cavity. It is not indicated in Fig. 22, but the read-out chain of the reference detector is such that the amplitude modulation can be directly measured in DC via the Magnicon electronics to the lock-in amplifier. So, the spectrum analyser is redundant in this case.

A part of the analysis involves the signal-to-noise performance of the system during the experiment. Here the approach by Davis, Abrams, and Brault 2008 is followed. The signal-to-noise (SNR) for the interferogram is

$$(SNR)_\delta = \frac{I(\delta = 0)}{\sigma_I} \ , \tag{29}$$

which means taking the interferogram strength at the centerburst — where the optical path difference is zero — and dividing it by the noise levels sufficiently far from the centerburst. This singular value for the interferogram SNR reappears in the spectral domain in the spectrum SNR:

$$(SNR)_\nu = \sqrt{\frac{2}{N}} \frac{S_\nu(\nu)}{\langle S_\nu \rangle} (SNR)_\delta \ , \tag{30}$$

where N is the number of points in the interferogram and $\langle S_\nu \rangle$ the mean of the spectrum intensity across the frequency range. It can be seen how the resolving power of the interferogram ($N/2$) and the local and mean signal strength in the spectral domain affect the SNR of the spectrum.

7.1 Pixel spectral response

The spectral response of each pixel in the prototype array can be inferred from step-scan measurements with the Michelson interferometer. For each pixel the bias point is determined from the TES current-voltage response to the optical loading which is measured prior to the step-scan. In particular, the bias point is chosen approximately in between the superconducting branch onset and the I/V minimum so that sensitivity (cf. Eq. 15) is high enough for a good signal-to-noise in the interferogram while stability performance is still adequate.

Fig. 23 shows the measured interferograms with pixels 1 to 4. These are averages of respectively four, five, two, and four measurements. The AC bias frequency and amplitude has been indicated for each measurement and details of the step-scan measurements are given in the figure description. The voltage (vertical) axis has been calibrated using the lock-in amplifier response to the peak-to-peak voltage modulation of the feedback signal. This can be done by simultaneously measuring the 25 Hz modulation of the feedback voltage given by the DEMUX.

This calibration is demonstrated in more detail in appendix B.2. The signal-to-noise ratios of the interferograms follows from Eq. 29 and equal 173, 154, 118, and 161 respectively for pixels 1 to 4.

Before a spectrum is calculated from the interferogram, it is calibrated by applying the following methods: regridding; normalization; apodization; and zero-filling. Firstly, by regridding the interferogram it is mapped to an ideal equidistant position grid in the 4 mm scan range. Secondly, the mean of the interferogram is subtracted which will be necessary for the zero-filling. Before zero-filling the interferogram is, thirdly, apodised with a Hanning window. Since the interferometer operates around 1 millibar, the features in the spectrum originating from the atmosphere are expected to be weak and the globar source can be considered as supplying continuous radiation so that a Hanning windowing would increase the spectral quality without losses [Griffiths and de Haseth 2007]. Lastly, the interferogram is artificially extended with zeros. This procedure effectively increases the spectral resolution further — the signal-to-noise is unaltered. Baseline correction and phase corrections are not considered. After the calibration calibration steps, a fast Fourier transform algorithm computes the spectrum from the interferogram. This procedure is repeated for pixels 2 to 4, the four spectra are presented in Fig. 24.

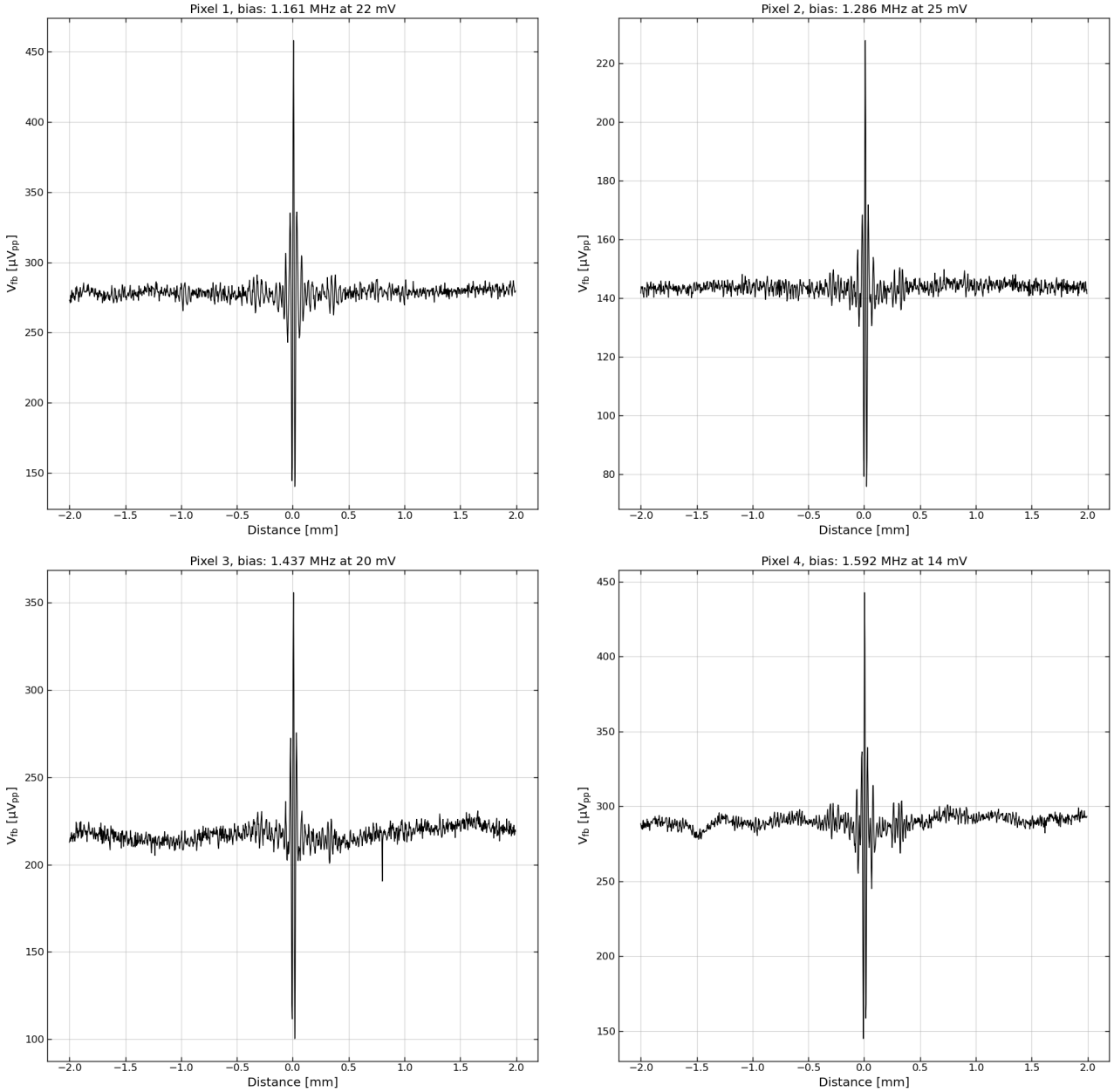

Figure 23: *Interferograms measured with pixels 1 to 4 modulating near [R/R_N] 11%, 25%, 20%, and 16%, respectively. The signal-to-noise ratios equal respectively 173, 154, 118, and 161. The lock-in amplifier output voltage has already been calibrated to the peak-to-peak modulation in the feedback voltage. A 540 K globar source was chopped at 25 Hz. The Michelson interferometer has a 6μm-mylar beamsplitter. In the step-scan the step-size was 3.75 μm over a range of 4.0 mm, giving a resolution of 75 GHz and a frequency range up to 20 THz. SQUID operating point: (I_b, I_{fb}) = (13.0, 18.0) μA. LNA settings: gain = 5000 and R_{in} = 112.6 Ω. Normal resistance: R_N = 160 mΩ.*

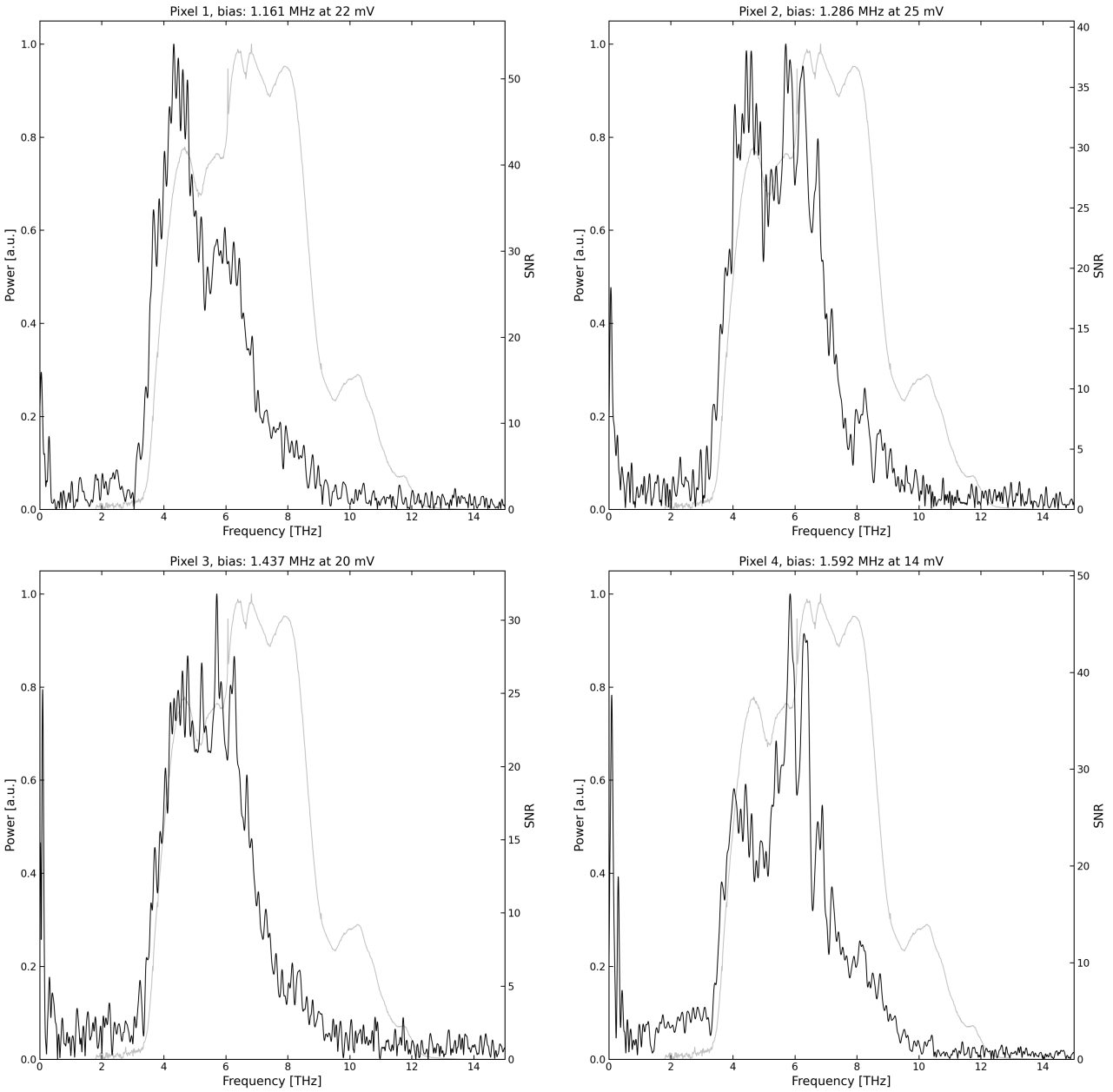

Figure 24: *Spectra of pixels 1 to 4 subjected to a 25 Hz power modulation between 540 K and 240 K. The graph titles indicate the AC bias frequency and peak-to-peak voltage amplitude. The spectral model from Eq. 31 has been overplotted for comparisons. The local signal-to-noise (SNR) in the spectra is shown. The positions in the transition, R/R_N, of pixels 1 to 4 are 11%, 25%, 20%, and 16%, respectively. The R/R_N modulations of pixel 1 and pixel 2 are below one percent, for pixel 3 it is roughly 1%, and for pixel 4 it is roughly 2%. SQUID operating point: (I_b, I_{fb}) = (13.0, 18.0) μA. LNA settings: gain = 5000 and R_{in} = 112.6 Ω. Normal resistance: $R_N = 160\ m\Omega$.*

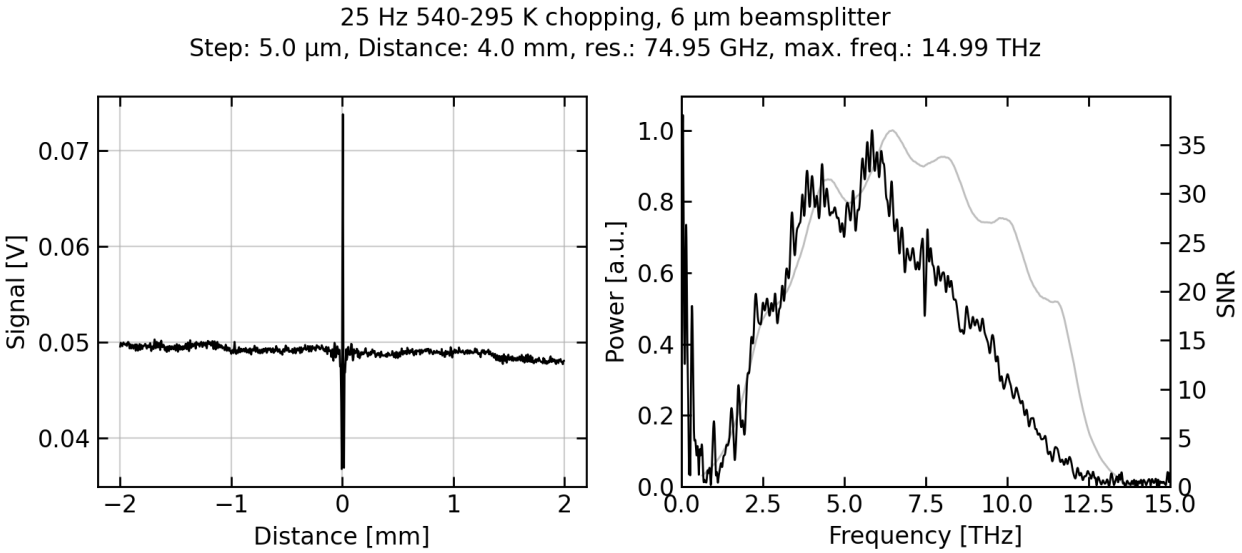

Figure 25: *The measured interferogram and calculated spectrum from the reference detector in the light cavity. The same measurements were performed for pixels 1 to 4. The spectral model from Eq. 31 has also been plotted over the spectrum and the local signal-to-noise (SNR) has been indicated.*

A simple model of the spectrum is projected as well in the pixel spectra of Fig. 24. The spectral power modulation $\Delta \mathrm{P}_\nu$ in [W Hz^{-1}] absorbed by the detector is modelled according to

$$\Delta P_\nu \propto \Delta B_\nu \cdot \mathrm{A}\Omega \cdot f(\nu) \cdot b(\nu) \ , \tag{31}$$

where the throughput, or etendue, can be written as $\mathrm{A}\Omega = \mathrm{G}(\lambda)\lambda^2$. The factor $\mathrm{G}(\lambda)$ specifies how many modes of a certain wavelength are present in the beam footprint, so $\mathrm{G}(\lambda) \geq 1$ for all λ. For example, a single-mode description has $G(\lambda) = 1$. In Eq. 31 there is also the filter transmission $f(\nu)$, the blackbody power modulation $\Delta B_\nu(\nu, \Delta T) = B(\nu, 540\ \mathrm{K}) - B(\nu, 295\ \mathrm{K})$, and the beamsplitter efficiency, $b(\nu)$, which is modelled following the work from Homes et al. 2007. Note that the following frequency-dependent factors have been ignored: atmospheric transmission, globar emissivity, optics efficiency, and the waveguide horn (array) response.

The step-scan measurements with the Michelson interferometer, the calibration steps, and computations have been repeated for the reference detector. The results can be found in Fig. 25.

7.2 Dark noise and photon noise

This section treats the noise performance of the system under increasing amounts of optical loading. Only pixel 1 is considered in this section. In the previous experiment in section 7.1 the optical loading was provided externally with a globar source. Here the source is internally provided by the cryogenic blackbody source in the light cavity, see Fig. 22. The shutter is closed in this experiment as in the experiments performed in section 6.

The bath temperature is set to 70 mK and I/V measurements are performed with the cryogenic blackbody source (CBB) at various powers. The lowest possible power corresponds to the environmental temperature at the CBB, which is 2.69 K. The highest possible power is determined at the onset of saturation of the TES' I/V response.

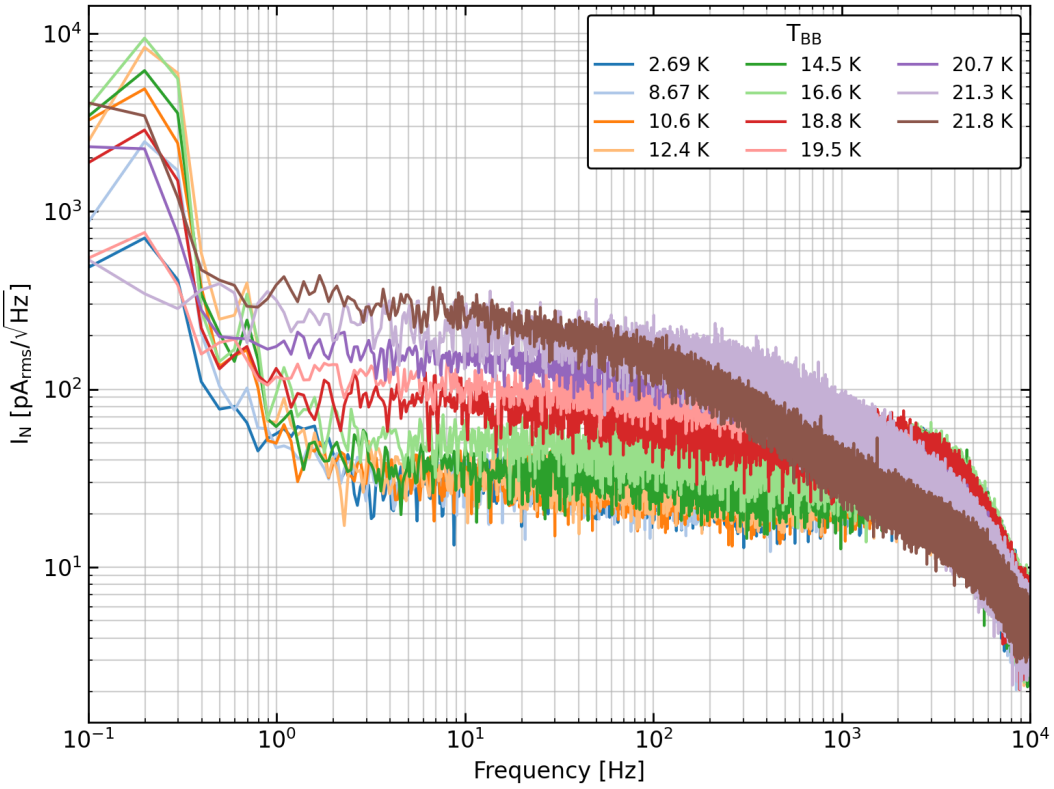

Figure 26: *Current noise spectral densities referred to the input coil as derived from the pixel feedback voltage measured by the DEMUX. The pixel 1 is biased at 50% R/R_N for different levels of optical loading from the cryogenic blackbody source. The bath temperature is 70 mK. SQUID operating point: $(I_b,\ I_{fb}) = (12.5,\ 20.0)\ \mu A$. LNA settings: gain = 5000 and $R_{in} = 112.6\ \Omega$. Normal resistance: $R_N = 160\ m\Omega$.*

The measured I/Vs are calibrated and analysed so that the voltage bias points can be found that correspond to the pixel being at 50% R/R_N for each level of optical loading[9]. Fig. 26 shows the measured current noise spectra due to the feedback signal of pixel 1 at 50% R/R_N for various power settings of the cryogenic blackbody source. The current noise at the input coil has been derived from the feedback voltage noise spectrum — measured by the DEMUX — using Eq. 24. It can be seen that the noise from the read-out chain and the TES detector dominates for $T_{BB} < 14.5$ K where the current noise is 30.4 pA/$\sqrt{\text{Hz}}$. At $T_{BB} \geq 14.5$ K the photon noise starts to dominate and it is clear that the response time of the pixel decreases with increased optical loading. This can be understood from the fact that the pixel's relaxation time constant is proportional to the low-frequency loop gain [Irwin and Hilton 2005], i.e. $\tau_{relax} \propto \mathcal{L}$. From Eq. 11 it can be understood that the Joule power, P_J, is forced to decrease due to the increased absorbed optical power. Thus, a decrease in electrothermal feedback occurs and τ_{relax} increases.

The current noise is averaged in a frequency window where all the spectra are sufficiently flat. The window 2 – 15 Hz is chosen and the left graph in Fig. 27 shows more clearly at what blackbody source power the photon noise starts to dominate. The standard deviation around the mean values are indicated as well. The standard deviations are relatively smaller for the noise averages for $T_{BB} \geq 19.5$ K since the spectra at these temperatures were taken twice as many times than the noise spectra for the other levels of optical loading.

[9]This is illustrated in appendix B.1

The zero-frequency power-to-current responsivity, $s_I(0)$ (Eq. 15), at the known bias points is used with the current noise to give the noise-equivalent power (NEP = $\frac{I_N}{s_I(0)}$). The absorbed optical power is known from the power plateaus which are calculated from the previously measured I/Vs. The right graph in Fig. 27 illustrates the photon noise behaviour with absorbed power, $NEP_\gamma \propto \sqrt{P}$, as is highlighted by the fitted function in this graph[10]:

$$NEP^2 = NEP^2_{read-out} + NEP^2_{TFN} + NEP^2_\gamma \ , \tag{32}$$

where the photon NEP is simply modelled as $NEP^2_\gamma = a \cdot P_{abs}$. The best-fit slope, a, is given in the legend of Fig. 27. The best-fit offset due to the read-out and phonon detector noise is given there as well. Previous work by the author and collaborators has also been presented in Fig. 27, see Audley et al. 2022[11]. Here the current noise floor is 57.2 pA/$\sqrt{\text{Hz}}$.

The photon noise may be computed with [Richards 1994]:

$$NEP^2_\gamma = \frac{P^2_N}{B} = 2\int P_\nu h\nu d\nu \ , \tag{33}$$

which is referred to power absorbed. So, P_N is the mean square absorbed noise power in an effective noise bandwidth B and P_ν is the absorbed spectral power. The absorbed spectral power may be written as $P_\nu = \eta P^*_\nu$. The TES pixel absorptivity, η, is known from the calculated incident power on the TES horn array for the various levels of power loading, see Fig. 28 (right), and the actual absorbed power from the measured I/V responses, Fig. 34. It was found that $\eta = 5.3 \pm 0.4\%$ in the 0 – 20 THz range. The incident beam spectral power, P^*_ν, assumes a blackbody intensity with a single-mode throughput and uses the known filter transmissions. The spectral response of the pixel, $s(\nu)$, is illustrated in Fig. 28 (left) and weighs the photon NEP appropriately — as made possible by the spectral measurements in section 7.1. Eq. 33 can then be rewritten to

$$NEP^2_\gamma = 2\eta \int_0^{20\ \text{THz}} B(\nu, T_{BB}) \cdot (c/\nu)^2 \cdot f(\nu) \cdot (s(\nu) h\nu) d\nu \ , \tag{34}$$

and the photon NEP computations from this expression together with the known NEP noise floor are present in Fig. 27 as a comparison.

[10] Excess noise sources are ignored.

[11] And the keen observer notices that the results from Audley et al. 2022 in Fig. 27 do not match the results found in the conference proceeding. This is because in this thesis it was found that feedback resistance corrections are necessary to correct for systematic errors in the voltages in the FDM set-up due to cable and electronics issues. The SQUID was used here as an absolute calibrator of the voltages.

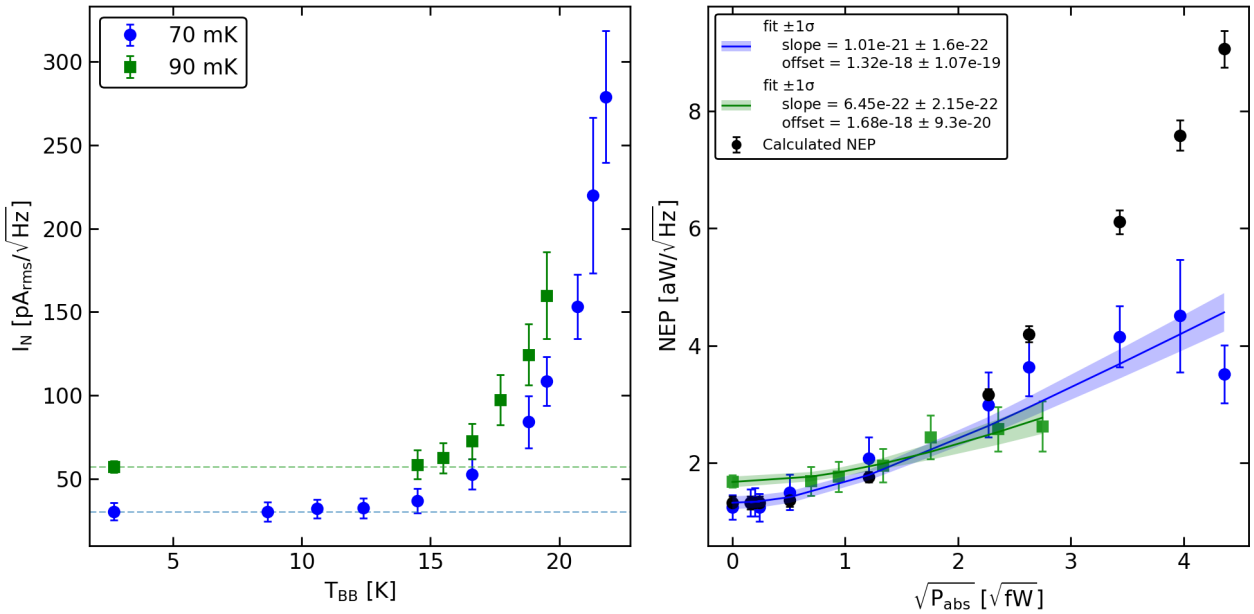

Figure 27: *In this figure the data with T_{bath} = 90 mK (green squares) are from Audley et al. 2022 with SQUID operating point: (I_b, I_{fb}) = (13.0, 8.0) μA. The data with T_{bath} = 70 mK (blue circles) has SQUID operating point: (I_b, I_{fb}) = (12.5, 20.0) μA. In both cases the LNA settings are: gain = 5000 and R_{in} = 112.6 Ω. Also, the pixel (px01) is biased to 50% R/R_N in all cases. Normal resistance: R_N = 160 mΩ.* ***(left)*** *Average current noise (referred to the input coil) in the 2 – 15 Hz (T_{bath} = 70 mK) and 2 – 20 Hz (T_{bath} = 90 mK) frequency window versus the cryogenic blackbody power that indicates the degree of incident optical power.* ***(right)*** *Noise equivalent power for different levels of optical power absorbed. Eq. 32 is fitted to the measurements. Separate calculations of the photon noise, from Eq. 34, together with the known noise floor are shown as well.*

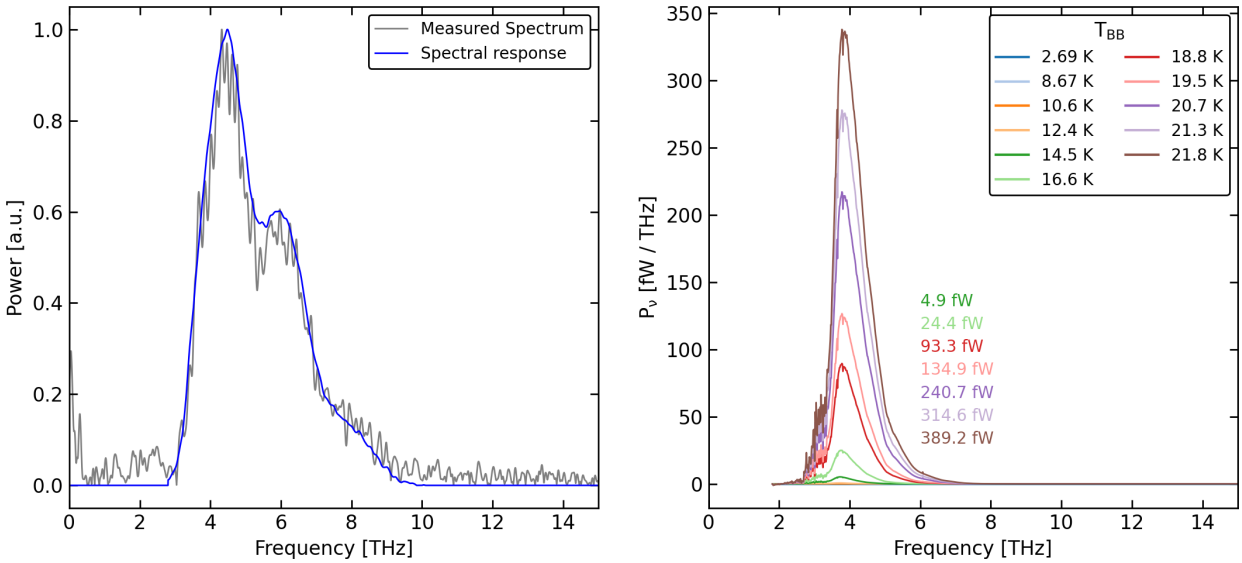

Figure 28: ***(left)*** *Pixel 1 spectrum measured earlier (Fig. 24) and the derived spectral response, $s(\nu)$.* ***(right)*** *Incident spectral power from the cryogenic blackbody source — assuming single-mode throughput — used to calculate the photon NEP from Eq. 33. The theoretical incident powers that are practically measurable are indicated.*

8 Discussion

From Figs. 2 and 15 it can be seen that the SQUID characteristics are not ideal. The origin of the distortions with excesses in noise are a well known phenomenon in SQUIDs and are attributed to internal feedback oscillations in the SQUID. These distortions limit the possible number of working points from which the SQUID may be operated. On a suitable working point it is nevertheless expected that the distortions have no impact on the SQUID's read-out stability performance. Indeed, the dynamic range was found to be sufficient during the project as the SQUID's flux-locked loop remained stable throughout all the measurements.

The interferogram of pixel 1 in Fig. 23 has artifacts near the mirror distances of -1.8 mm and -1.0 mm from ZPD which accompany a slightly distorted baseline on the left half. Furthermore, the interferogram is not fully symmetric near the centerburst and first side lobes. This effect is, in part, due to chirping (phase delay). The asymmetry is also found in the interferograms of pixels 2 to 4. Moreover, the interferograms of pixels 3 and 4 have strongly distorted baselines. The different baseline distortions in the interferograms could have been caused by temperature fluctuations in the cryogenic housing which affects the pixel sensitivity while measuring the interferograms. The origins of the former two artifacts in the interferograms is not fully understood but one could speculate about the consistency of the globar output power, optical chopper rate, and the Michelson interferometer mirror displacement accuracy (across the whole area of the mirror). The interferogram quality would benefit from changing the modus operandi to rapid-scan measurements with a suitable Michelson interferometer to avoid the effects from the possible time-dependence of the light intensity and the TES sensitivity.

The signal-to-noise ratios (SNRs) of the interferograms were found to be 173, 154, 118, and 161 for pixels 1 to 4. Recall that the pixel 1 interferogram is an average of four measured interferograms. For pixels 2 to 4, the average consists of five, two, and four averages, respectively. This number varies due to time constraints and difficulties in measuring stable interferograms at the particular development stage of the optical test-bed. Firstly, the number of averages explains in part the SNR differences. Secondly, the intensity of the beam incident on the TES array feed-horn array plays a role, i.e. the beam pattern. If the beam incident on the feed-horn array is Gaussian, then it is expected that the signal level drops as such, increasingly further from the center of the TES array[12]. Lastly, the sensitivity of the pixel at its respective point in the transition affects the magnitude of modulation in the feedback signal due to the optical loading. Now, it should be noted that theoretically the signal strength at the centerburst is twice the background continuum level. For the interferograms of pixel 1 to 4 the centerburst strength is between 1.6 – 1.7 times the background continuum which, in practice, is a good result. Mirror misalignment in the Michelson interferometer during the scan can cause a decrease in interference strength at the centerburst, subsequently negatively impacting the signal-to-noise ratio.

The calculated spectra were shown in Fig. 24 and it can be seen that oscillations are present in the spectra near 4.5 THz. The distances between the nodes of these oscillations fall within the frequency range of 80 to 210 GHz (just above the interferogram resolution). It is speculated that these oscillations arise from standing waves that are created at some point in the optical path of the light like in a Fabry-Pérot cavity. If so, the frequency range 80 – 210 GHz would correspond to half-wavelengths of 1 – 4 mm or cavity sizes of 2 – 8 mm. Since the lightpipe exit aperture was set to 5 mm[13] during the experiment it can be suggested that standing waves are created in the lightpipe as the light travels from the globar to the TES array. However, the standing waves are not apparent in the reference detector spectrum of Fig. 25, see also Fig. 29, which contradicts the previous statement and suggests the absence of standing waves altogether or suggests that the standing waves are created at some point between the light cavity and the TES array.

[12] Assuming the incident beam on the feed-horn array is centered on it in the first place.
[13] Which is also the lightpipe diameter.

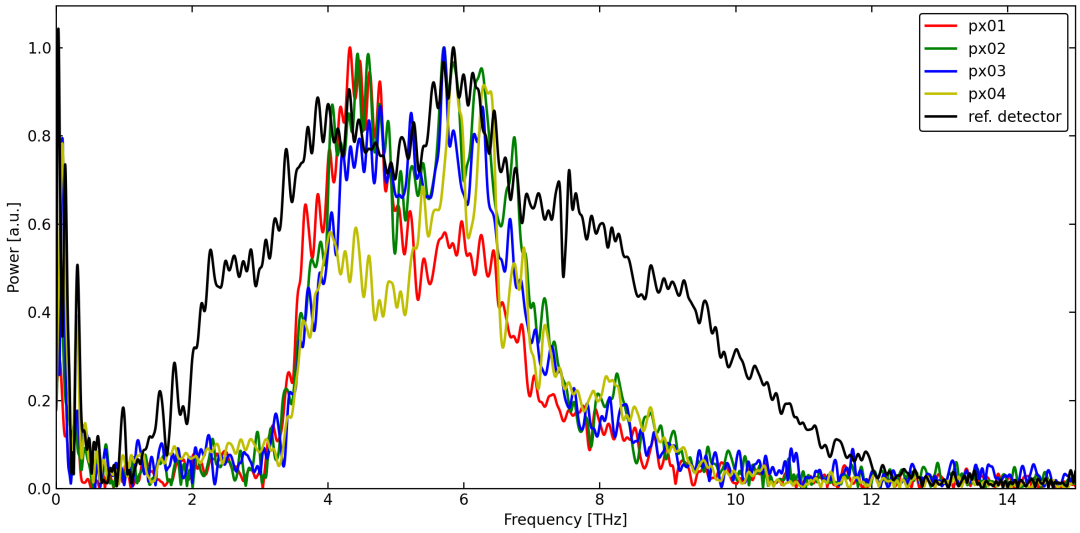

Figure 29: *Overlay of the measured spectra from section 7.1.*

Low-frequency artifacts are present in each spectrum which is due to the slow baseline modulations in the measured interferograms.

It is challenging to find similar features in all the four pixel spectra and the reference detector spectrum, apart from the weakly common features at 4.3 THz, 4.6 THz, 5.7 THz, and 5.9 THz, the low-frequency cut-off due to the transmission filters, and the consistent high-frequency cut-off at around 6.5 THz. Centrally, the pixel spectral responses in Fig. 24 are notably different which is not to be expected as the pixels observe the same source as indicated by the gray overlays in the spectra of the model from Eq. 31. Here, it would be beneficial to have been able to spectrally characterise more pixels in the array so that possible correlations are more easily found in the larger statistics. It is expected that the high-frequency cut-off of the model in Eq. 31 is incorrect due to the fact that it does not incorporate the waveguide horn response. This is because the roughness of the individual horn walls in the horn array could determine the high-frequency cut-off and it is not expected that the pixels systematically lose sensitivity at higher frequencies — the copper walls from the waveguide horns are a product of electroplating and it may be that the surface roughness is considerable. However, the model from Eq. 31 shows a similar discrepancy when compared to the reference detector spectrum and suggests instead that high-frequency attenuation occurs in the light cavity or somewhere in the optical path before this location. In any case, uniformity in the pixel spectral responses is not guaranteed due to the unavoidable fabrication tolerances involved in the production of the horn array. It is known that the light-pipe attenuates the external optical power with a factor $\sim 10^6$, but it is suspected that there is a bias towards frequencies above 6.5 THz. Alternatively, one could argue that the electromagnetic (EM) wave propagation is made rather complex near the detector bench with the inclusion of the waveguide horn, the hemispherical backshort, and the distances between them (Fig. 10). Possible high-frequency attenuation due to this complex interplay and the 3-D EM wave simulations required to model it are beyond the scope of this thesis. In any case, generally speaking, the TES pixel spectra in this prototype array demonstrate sensitivity in the 4 – 9 THz frequency range while biased significantly low in their transition. This performance may be comparred with competitive far-infrared detector technology like the the kinetic inductance detector (KID) which has taken recent interest. The working principles, pros, and cons are beyond the scope of this thesis but sensitivity of state-of-the-art KIDs above 6 THz frequencies ($\lambda < 50$ µm) for ∼fW power loadings is still to be demonstrated.

Throughout this work, the SQUID and LNA settings were consistent up until the optical characterisation of pixel 1 in section 7.2, as can be found in the figure captions. After the spectral characterisation of pixels 1 to 4 in section 7.1 it was necessary to perform maintenance, repairs, and improvements on the cryostat, pumps, and the optical test-bed to tackle the continuously decreasing and unstable cooling capabilities. After this process, suitable SQUID operation was chosen to be at (I_b, I_{fb}) = (12.5, 20.0) µA. This, then, is not consistent with the read-out noise analysis from section 6. The thermal noise from the SQUID is negligible regardless, but the SQUID's dynamic resistance that couples to the LNA is different. Subsequently, the read-out noise differs from the 15.9 pA/$\sqrt{\text{Hz}}$ found in section 6.2. Having said that, it was found in section 7.2, Fig. 27 (right), that the current noise referred to the input coil under dark circumstances was 30.4 pA/$\sqrt{\text{Hz}}$ for pixel 1 at 70 mK and at 50% R/R_N. The phonon NEP from Tab. 2 may be used with the zero-frequency power-to-current responsivity from the T_{BB} = 2.74 K (dark) I/V response of Fig. 34 to find that the phonon noise contributes 18.4 pA/$\sqrt{\text{Hz}}$. Given the scatter around the mean value of the noise floor, the read-out noise is then calculated to be 24.2 ± 6.5 pA/$\sqrt{\text{Hz}}$. Similarly, the phonon current noise in the case of the 90 mK data contributes 25.7 pA/$\sqrt{\text{Hz}}$ to its noise floor, implying a read-out noise of 51.1 ± 3.9 pA/$\sqrt{\text{Hz}}$. This is not an odd result given the current noise curves of Fig. 16 and knowing the SQUID operating point of the 90 mK measurements is (I_b, I_{fb}) = (13.0, 8.0) µA. Although there is no guarantee that the same current noise curves can now be recovered after the optical test-bed improvements. Thus, if we ignore excess noise sources, Fig. 27 gives the impression that the read-out noise dominates over the detector noise before the photon noise does. A reason, then, for this observation is the significant change of SQUID performance at the new bias settings. An extensive analysis as in section 6.2 of the SQUID performance to test this finding has not been performed due to time constraints. In any case, the photon current noise behaviour is consistent between the two data sets as can be seen when the two are put on top of each other.

The noise-equivalent powers of the two data sets in Fig. 27 (right) are expected to follow the trend given by Eq. 32, however it is clear that the 90 mK data set strays from this trend for $T_{BB} > 17.7$ K and the 70 mK data set at $T_{BB} > 21.3$ K. In other words, for absorbed powers greater than 3.1 fW and 15.7 fW, respectively. One could argue that the apparent lack of increase in photon NEP at higher optical powers may be an artifact of the responsivity approximation. The relevant signal frequencies in Fig. 27 are f ≤ 20 Hz, so it may be taken that $\omega \approx 0$. Eq. 12 then becomes

$$s_I(0) \approx -\frac{1}{I_{TES}R_{TES}}\left[\frac{L}{\tau_{el}R_{TES}\mathcal{L}} + \left(1 - \frac{R_{TH}}{R_{TES}}\right)\right]^{-1} . \tag{35}$$

As the optical loading increases the Joule power, P_J, in the TES decreases and since $\mathcal{L} \propto P_J$ so does the low-frequency loop gain of the electrothermal feedback (ETF) circuit, $\mathcal{L}$. Therefore, it may be that the first term in the brackets becomes appreciable for the respective optical powers where the two data sets start to deviate from the expected trend. Consequently, the magnitude of the responsivity from Eq. 35 would be lower than simply V_{TES}^{-1}. But then the NEP computes to higher values with Eq. 35 than with the simplified expression. So, the expected inaccuracy of the responsivity approximation due to small loop gains cannot explain the curiously low NEP values for the larger optical powers.

Now, consider the measured NEPs at bath temperatures of 70 mK and 90 mK in Fig. 27 (right) with respect to each other. Firstly, the noise floors are different as with the current noises. Here however, this is not to be expected as there is no explicit dependence of the NEP on the bath temperature and the difference in responsivities at the different bath temperatures should equalise the NEPs between 70 mK and 90 mK. So far, the measured current noises provided a consistent picture given fair arguments but this is not the case for the NEPs. In fact, it is more likely that systematic errors are present in the I/V response calibration in the sense that the underlying effective AC bias TES read-out circuit of Fig. 18 is not representative of how the circuit actually behaves due to unknown noise sources with unknown dependencies on the experimental parameters. As mentioned in section 6.3,

array modifications were performed to mitigate cross-talk. It cannot be excluded that cross-talk completely disappeared and does not affect the calibration anymore. Furthermore, a brief note in section 6.2 already mentioned the observation of an effective small shift in the SQUID working point due to the optical loading from the globar modulation in the spectral measurements. Systematic errors may thus arise in the calibration due to undesired SQUID behaviour at levels of optical loading larger than during the spectral measurements[14]. The systematic errors may then be the cause of the different photon noise slope between the two bath temperatures which should only depend on quantities that are consistent between the two data sets, as Eq. 34 illustrates. Systematic issues that affect the validity of the AC bias TES calibration circuit may also have affected the measurements of the curiously low NEPs for the largest optical loadings.

The photon NEP calculations from Eq. 34 are based on a single-mode throughput. If more modes are able to propagate through the aperture stop of the system — in this case the horn exit aperture — than the incident power would be underestimated and the optical efficiency would be overestimated. Extensive multimodal EM simulations to estimate the amount of modes in the horn as a function of frequency is beyond the scope of this thesis. Eq. 34 also assumes that the pixel sees the entire cryogenic blackbody source exit aperture in its beam. The horn exit opening angle is known quite well from Fig. 9b and equals 6.0°. The distance between the horn array and the CBB aperture is estimated at 2.0 cm (though this needs to be confirmed through measurement), giving a square horn beam area at the CBB of $(6^\circ \cdot \pi/180^\circ \cdot 2.0 \times 10^{-2})^2 = 4.4 \times 10^{-6}$ m^2. This corresponds to a square patch with sides of length 2.1 mm. The diameter of the CBB aperture is 12 mm. Obviously, pixels closely under the CBB aperture center would see a filled beam of a blackbody source with power T_{BB}. Imagine a horn center at the top-right edge of the horn array, i.e., from Fig. 9a, with a displacement of 5 mm from the center along the diagonal. This point can be labeled as $(x, y) = (3.5, 3.5)$. The top-right edge of the square horn beam at the CBB would then be located at $(x, y) = (4.5, 4.5)$ or at a radius of 6.4 mm. This is just outside the CBB aperture radius and this horn at the maximum distance from the center will see a portion of a 2.7 K blackbody, although the effects can be estimated to be small. Given the guess of the 2.0 cm distance between the horn array and the CBB aperture, it is unlikely that the beam filling factor plays a significant role in determining the photon noise.

8.1 Dark NEP comparisons with 2013 findings

The pixel 1 dark NEPs found here in Fig. 27 (right) of 1.32 ± 0.11 aW/$\sqrt{\text{Hz}}$ (T_{bath} = 70 mK, 50% R/R_N) agree with earlier dark characterisation measurements of the prototype array by den Hartog et al. 2014 (T_{bath} = 65 mK, 40% R/R_N) in 2013. However, this is not in line with the pixel phonon NEP found in section 6.3, 0.676 ± 0.023 aW/$\sqrt{\text{Hz}}$, if the TES phonon noise is expected to dominate the dark noise. The phenomenon that may be involved here is the apparent decrease of the measured power plateaus by a factor larger than 2.0 as was observed in den Hartog et al. 2014, see Fig. 30 from their work. To elaborate, this was observed after a wirebonding procedure on the prototype array that increased the pixel count from 3 to 38 — the initial goal was to be able to use all 64 pixels of the array but various technical issues and complications eventually led to the latter number. Earlier DC power plateau measurements were found to agree with the 3-pixel AC measurements in den Hartog et al. 2014, but, as mentioned, this was found not to be the case when the pixel count was increased. They speculated that unexpected LC filter alterations could have caused this result — next to unwanted SQUID behaviour or possible cross-talk contamination already mentioned in this work. As in the 2013 measurements, but with additional alterations of the detector chip, the DC and 3-pixel AC measurements of the power plateaus could also not be reproduced indicating the same problem in the calibration in this particular experiment.

[14] An estimate of the optical loading from the 295/540 K power modulation could not be estimated since the I/V responses at 100 mK were too insensitive to such small power loadings.

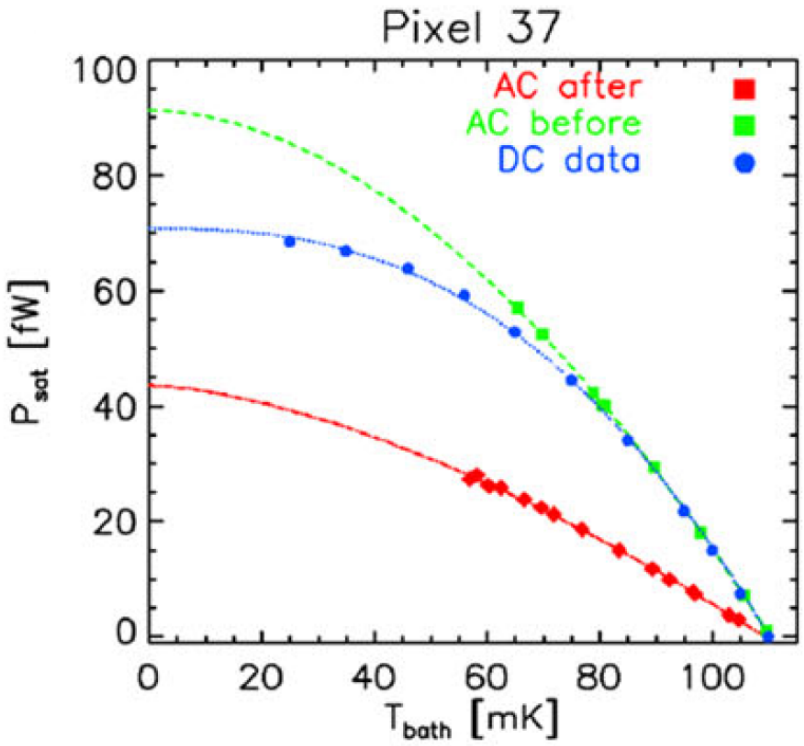

Figure 30: *Effective saturation powers at 40% R/R_N as a function of bath temperature for pixel 37 (AC bias: 3.034 MHz). The same model as Eq. 5 is seen fitted to the data. The difference between the three data sets is discussed in the text. These measurements and the analysis have been performed by den Hartog et al. 2014.*

In fact, the saturation power difference — which can be read off from Fig. 20 and Fig. 30 — between pixel 4 (AC bias: 1.528 MHz)[15] and pixel 37 (DC bias) is a factor 2.9 at $T_{bath} = 75$ mK.

Although the numerical values of the voltages, currents, and powers that follow from I/V calibration are erroneous, this does not act as a practical showstopper. The qualitative spectral characterisation of section 7.1 is one reason. The other is that space-based FIR observational techniques, like SPICA, typically involve on-sky calibrator sources from which the flux is known with confidence. The absorbed powers by the TES may then be appropriately calibrated and knowing that the TES array is a linear power detector would then allow accurate flux measurements anyhow.

[15]Pixel 4 is chosen here because this pixel is the closest available in AC bias frequency to pixel 37.

9 Conclusion

The novel cryostat-housed optical test-bed configuration used and further developed during this thesis allowed the signal read-out of individual transition-edge sensors (TESs) in a single-stage-SQUID frequency-division multiplexing architecture with baseband feedback. At the start of the thesis the setup was still in its development stage; the performance of the cryostat and test-bed was gradually improved over the course of time. The set-up offered the flexibility to perform three separate experiments on the TES array under study. This 8×8 prototype array, originally designed for the SPICA mission, is flawed and underwent several on-chip wirebonding alterations to ensure pixel stability and performance. The pixel count was limited to 4 and simultaneously reading out several pixels unfortunately did not result in good performance, so this method was avoided.

The first experiment in section 6 presented, firstly, the room-temperature noise characterisation of the demultiplexer and low-noise amplifier in the front-end electronics (FEE) — developed in-house by SRON — based on the equivalent circuit model in Fig. 11. The DEMUX voltage noise was found to be 203.5 nV/$\sqrt{\text{Hz}}$, the LNA voltage and current noise were approximated to 365 pV/$\sqrt{\text{Hz}}$ and 6.0 pA/$\sqrt{\text{Hz}}$ which are consistent results given the analysis of previous FEE SRON electronics. Secondly, calibration tone measurements with the SQUID amplifier allowed the possible bias operating point space to be extensively explored. A suitable operating point was chosen with a system read-out current noise (referred to the SQUID input coil) of 15.9 pA/$\sqrt{\text{Hz}}$ and proved to be consistent with model calculations. Lastly, the TES phonon noise was derived for the four available pixels which lead to phonon NEPs ∼50% lower than expected from earlier DC characterisation work of pixels in the array [den Hartog et al. 2014]. Possible LC filter alterations, unwanted SQUID behaviour, or excessive cross-talk could be explanations to this discrepancy. The phonon current noises regarding the spectral measurements were computed and found to be consistent with den Hartog et al. 2014 for TES pixels biased low in the transition. For practically all possible TES bias points of the four measured pixels it was found that the phonon noise dominates over the read-out noise.

A globar source, optical chopper, and Michelson interferometer — situated outside the cryostat — successfully allowed step-scan spectral characterisation of the four operational TES pixels in the array in the 4 – 9 THz frequency range. This was demonstrated in section 7.1. Poor cryostat performance at the time of the experiment limited the bath temperature to 100 mK which is close to the critical temperatures of the pixels. Pixels 1 to 4 were biased low in the transition to achieve maximum sensitivity. There are indications that standing waves contaminate the pixel spectra, but not the reference detector spectrum. The standing waves could have been created between the light cavity and the TES array. The pixel spectra and reference detector spectrum show high-frequency attenuation for frequencies above ∼6.5 THz when compared to the expected spectral response from Eq. 31. This attenuation is induced somewhere before the light cavity. The spectral responses of the four pixels are unexpectedly different, except for the low-frequency cut-on (filter transmission) and high-frequency cut-off (induced somewhere before the light cavity), and show poor correlations. There is also little correlation with the reference detector spectrum. The details on the fabrication and state of the horns in the horn array and the backshort array are lacking but could cause the discrepancies in the non-uniformity of the pixel spectral responses.

Section 7.2 presented photon noise measurements of pixel 1 at 70 mK bath temperatures by use of the cryogenic blackbody source located in the light cavity. 90 mK bath temperature measurements were also shown, from Audley et al. 2022. The current noise behaviour at the onset of background-limited performance was determined to be consistent between the two data sets. The current noise floors (or, dark current noises) are difficult to confirm as consistent, given the power-to-current sensitivity's dependence on bath temperature and possible influence by unwanted SQUID behaviour, cross-talk, and unknown excess noise sources.

The dark noise from section 7.2 and from the earlier end-to-end noise analysis cannot be compared due to test-bed tweaks and alternative SQUID settings at the time of the photon noise experiment. The NEPs between the 70 mK and 90 mK data sets are found not to be consistent, possibly due to the aforementioned effects that make the effective TES AC bias calibration circuit from Fig. 18 not realistic and the calibration thus erroneous due to the systematic errors. Theoretical photon NEP calculations from Eq. 34 can be improved by implementing factors that detail the optical coupling circumstances of the TES array in the optical test-bed and by considering the multi-mode EM wave propagation in the horns as a function of frequency. This is expected to lower the calculated photon NEPs, more in line with the measured values.

References

Audley, M. D. et al. (Sept. 2014). "Measurements of the Optical Performance of Prototype TES Bolometers for SAFARI". In: *Journal of Low Temperature Physics* 176.5, pp. 755–760. ISSN: 1573-7357. DOI: 10.1007/s10909-013-0984-5 (cit. on p. 20).

Audley, M. D., Huijser, G. F., de Lange, G., and Orlando, A. (2022). "Optical measurements of ultrasensitive far-infrared TES bolometers with FDM readout". In: *Millimeter, Submillimeter, and Far-Infrared Detectors and Instrumentation for Astronomy XI*. Ed. by J. Zmuidzinas and J.-R. Gao. Vol. 12190. International Society for Optics and Photonics. SPIE, p. 121901L. DOI: 10.1117/12.2629201 (cit. on pp. 41, 42, 48, 52, 56).

Barret, D. et al. (June 2018). "The Athena X-ray Integral Field Unit". In: *SPIE Astronomical Telescopes + Instrumentation 2018*. Vol. 10699. Austin, United States, 106991G. DOI: 10.1117/12.2312409 (cit. on p. 7).

Bracken, C., de Lange, G., Audley, M. D., Trappe, N., Murphy, J. A., Gradziel, M., Vreeling, W.-J., and Watson, D. (2018). "A novel, highly efficient cavity backshort design for far-infrared TES detectors". In: *Infrared Physics & Technology* 89, pp. 194–202. ISSN: 1350-4495. DOI: https://doi.org/10.1016/j.infrared.2018.01.004 (cit. on p. 16).

Clarke, J. and Braginski, A. I. (2004). *The SQUID Handbook. Vol 1: Fundamentals and Technology of SQUIDs and SQUID systems*. Weinheim, Germany: WILEY-VCH Verlag GmbH & Co. KGaA, pp. 2, 357–365. ISBN: 3-527-40229-2 (cit. on pp. 4, 5).

Cui, W. et al. (2020). "HUBS: a dedicated hot circumgalactic medium explorer". In: *Space Telescopes and Instrumentation 2020: Ultraviolet to Gamma Ray*. Ed. by J.-W. A. den Herder, S. Nikzad, and K. Nakazawa. Vol. 11444. International Society for Optics and Photonics. SPIE, pp. 470–481. DOI: 10.1117/12.2560871 (cit. on p. 7).

Davis, S., Abrams, M., and Brault, J. (2008). *Fourier Transform Spectrometry*. Academic Press. Chap. Effects of noise in its various forms, pp. 119–141. ISBN: 9780120425105 (cit. on p. 36).

den Hartog, R. H. et al. (Aug. 2014). "Progress on the FDM Development at SRON: Toward 160 Pixels". In: *Journal of Low Temperature Physics* 176.3, pp. 439–445. ISSN: 1573-7357. DOI: 10.1007/s10909-014-1117-5 (cit. on pp. 46–48).

Drung, D., Beyer, J., Peters, M., Storm, J.-H., and Schurig, T. (2009). "Novel SQUID current sensors with high linearity at high frequencies". In: *IEEE transactions on applied superconductivity* 19.3, pp. 772–777 (cit. on p. 6).

Gottardi, L., Kiviranta, M., van der Kuur, J., Akamatsu, H., Bruijn, M. P., and den Hartog, R. (2014a). "Nearly quantum limited two-stage SQUID amplifiers for the frequency domain multiplexing of TES based X-ray and infrared detectors". In: *IEEE Transactions on Applied Superconductivity* 25.3, pp. 1–4 (cit. on p. 6).

Gottardi, L. et al. (2014b). "Josephson effects in an alternating current biased transition edge sensor". In: *Applied Physics Letters* 105.16, p. 162605. DOI: 10.1063/1.4899065 (cit. on p. 15).

Gottardi, L. et al. (Nov. 2018). "Josephson Effects in Frequency-Domain Multiplexed TES Microcalorimeters and Bolometers". In: *Journal of Low Temperature Physics* 193.3, pp. 209–216. ISSN: 1573-7357. DOI: 10.1007/s10909-018-2006-0 (cit. on p. 15).

Gottardi, L. and Nagayashi, K. (2021). "A Review of X-ray Microcalorimeters Based on Superconducting Transition Edge Sensors for Astrophysics and Particle Physics". In: *Applied Sciences* 11.9. ISSN: 2076-3417. DOI: 10.3390/app11093793 (cit. on p. 15).

Griffiths, P. R. and de Haseth, J. A. (2007). "THEORETICAL BACKGROUND: Apodization". In: *Fourier transform infrared spectrometry*. 2nd ed. Wiley (cit. on p. 36).

Harper, D. A. et al. (2018). "HAWC+, the Far-Infrared Camera and Polarimeter for SOFIA". In: *Journal of Astronomical Instrumentation* 07.04, p. 1840008. DOI: 10.1142/S2251171718400081 (cit. on p. 7).

Holland, W. S. et al. (Mar. 2013). "SCUBA-2: the 10 000 pixel bolometer camera on the James Clerk Maxwell Telescope". In: *Monthly Notices of the Royal Astronomical Society* 430.4, pp. 2513–2533. ISSN: 0035-8711. DOI: 10.1093/mnras/sts612 (cit. on p. 6).

Homes, C. C., Carr, G. L., Lobo, R. P. S. M., LaVeigne, J. D., and Tanner, D. B. (Nov. 2007). "Silicon beam splitter for far-infrared and terahertz spectroscopy". In: *Appl. Opt.* 46.32, pp. 7884–7888. DOI: 10.1364/AO.46.007884 (cit. on p. 39).

Irwin, K. and Hilton, G. (2005). *Cryogenic Particle Detection: Transition-Edge Sensors*. Ed. by C. E. Ascheron. Topics Appl. Phys. 99. Heidelberg, Germany: Springer-Verlag Berlin, pp. 63–152. ISBN: 978-3-540-20113-7 (cit. on pp. 8, 9, 11, 12, 40).

Jackson, B. D. et al. (2012). "The SPICA-SAFARI Detector System: TES Detector Arrays With Frequency-Division Multiplexed SQUID Readout". In: *IEEE Transactions on Terahertz Science and Technology* 2.1, pp. 12–21. DOI: 10.1109/TTHZ.2011.2177705 (cit. on p. 16).

Jaehnig, G. C. et al. (May 2020). "Development of Space-Optimized TES Bolometer Arrays for LiteBIRD". In: *Journal of Low Temperature Physics* 199.3, pp. 646–653. ISSN: 1573-7357. DOI: 10.1007/s10909-020-02425-2 (cit. on p. 6).

Khosropanah, P. et al. (2010). "Low-noise transition edge sensor (TES) for SAFARI instrument on SPICA". In: *Millimeter, Submillimeter, and Far-Infrared Detectors and Instrumentation for Astronomy V*. Ed. by W. S. Holland and J. Zmuidzinas. Vol. 7741. International Society for Optics and Photonics. SPIE, pp. 163–171. DOI: 10.1117/12.857725 (cit. on p. 19).

Montgomery, J. et al. (2020). "Performance and characterization of the SPT-3G digital frequency multiplexed readout system using an improved noise and crosstalk model". In: *Millimeter, Submillimeter, and Far-Infrared Detectors and Instrumentation for Astronomy X*. Ed. by J. Zmuidzinas and J.-R. Gao. Vol. 11453. International Society for Optics and Photonics. SPIE, pp. 167–188. DOI: 10.1117/12.2561537 (cit. on p. 6).

Nucciotti, A. et al. (Dec. 2018). "Status of the HOLMES Experiment to Directly Measure the Neutrino Mass". In: *Journal of Low Temperature Physics* 193.5, pp. 1137–1145. ISSN: 1573-7357. DOI: 10.1007/s10909-018-2025-x (cit. on p. 7).

Ravera, L. et al. (2014). "The X-ray Integral Field Unit (X-IFU) for Athena". In: *Space Telescopes and Instrumentation 2014: Ultraviolet to Gamma Ray*. Ed. by T. Takahashi, J.-W. A. den Herder, and M. Bautz. Vol. 9144. International Society for Optics and Photonics. SPIE, pp. 779–791. DOI: 10.1117/12.2055884 (cit. on p. 6).

Richards, P. L. (1994). "Bolometers for infrared and millimeter waves". In: *Journal of Applied Physics* 76.1, pp. 1–24. DOI: 10.1063/1.357128 (cit. on p. 41).

Roelfsema, P. et al. (2014). "SAFARI new and improved: extending the capabilities of SPICA's imaging spectrometer". In: *Space Telescopes and Instrumentation 2014: Optical, Infrared, and Millimeter Wave*. Ed. by J. M. Oschmann, M. Clampin, G. G. Fazio, and H. A. MacEwen. Vol. 9143. International Society for Optics and Photonics. SPIE, pp. 419–429. DOI: 10.1117/12.2056449 (cit. on p. 6).

Rohlf, J. W. (1994). "Superconductivity". In: *Modern Physics from α to Z^0*. 2nd ed. Wiley, pp. 403–433 (cit. on p. 4).

Sadleir, J. E., Smith, S. J., Robinson, I. K., Finkbeiner, F. M., Chervenak, J. A., Bandler, S. R., Eckart, M. E., and Kilbourne, C. A. (Nov. 2011). "Proximity effects and nonequilibrium superconductivity

in transition-edge sensors". In: *Phys. Rev. B* 84 (18), p. 184502. DOI: 10.1103/PhysRevB.84.184502 (cit. on p. 10).
Sakai, K. et al. (Nov. 2018). "Study of Dissipative Losses in AC-Biased Mo/Au Bilayer Transition-Edge Sensors". In: *Journal of Low Temperature Physics* 193.3, pp. 356–364. ISSN: 1573-7357. DOI: 10.1007/s10909-018-2002-4 (cit. on p. 15).
Shirazi, F. et al. (2022). *The 511-CAM Mission: A Pointed 511 keV Gamma-Ray Telescope with a Focal Plane Detector Made of Stacked Transition Edge Sensor Microcalorimeter Arrays*. arXiv: 2206.14652 [astro-ph.IM] (cit. on p. 7).
Wang, Q. et al. (2021). "Frequency division multiplexing readout of 60 low-noise transition-edge sensor bolometers". In: *Applied Physics Letters* 119.18, p. 182602. DOI: 10.1063/5.0065570 (cit. on p. 10).
Wang, Q. et al. (2022). "Frequency division multiplexing readout of a microstrip wired, slow TES bolometer array". In: *Rev. Sci. Instrum.* under submission, to appear (cit. on p. 8).
Wang, Q. (Dec. 2021). "Development of frequency division multiplexing readout for a large transition edge sensor array for space". PhD thesis. Rijksuniversiteit Groningen (cit. on pp. 11, 13, 14, 28).
Wang, Q., Audley, M. D., Khosropanah, P., van der Kuur, J., de Lange, G., Aminaei, A., Boersma, D., van der Tak, F., and Gao, J.-R. (May 2020). "Noise Measurements of a Low-Noise Amplifier in the FDM Readout System for SAFARI". In: *Journal of Low Temperature Physics* 199.3, pp. 817–823. ISSN: 1573-7357. DOI: 10.1007/s10909-019-02328-x (cit. on pp. 23, 24).

A Derivation approximate TES phonon current noise

Here the derivation of Eq. 16 is outlined. Consider the effective saturation power from Eq. 5 which may be simplified if the bath temperature is considerably lower than the critical temperature of the TES bilayers in the prototype array ($T_c = 105$ mK):

$$P_{sat} = K(T_c^n - T_{bath}^n) \approx KT_c^n$$

If a typical value for the strength of the thermal conductance is assumed, say n = 2.35, then $T_{bath}^n/T_c^n < 10\%$ for bath temperatures below ∼40 mK. Thus, the approximation is somewhat accurate for bath temperatures below 40 mK. The thermal conductance G can be rewritten with the expression above:

$$G = nKT_c^{n-1} \approx \frac{nP_{sat}}{T_c} = \frac{n(V_{TES}I_{TES} + P_{FIR})}{T_c}$$

where additional power from incident radiation has been introduced: P_{FIR}. The voltages and currents above are in phase. Eq. 10 for the phonon NEP, Eq. 15 for the approximate zero-frequency responsivity, and the expression of the thermal conductance above then give the approximate TES phonon current noise:

$$\begin{aligned} I_{TFN} &= NEP_{TFN} \cdot s_I(0) \\ &\approx \frac{\sqrt{4\gamma k_B T_c^2 G}}{V_{TES}} \\ &\approx \sqrt{4\gamma k_B n T_c \left(\frac{I_{TES}}{V_{TES}} + \frac{P_{FIR}}{V_{TES}^2}\right)} \\ &= \sqrt{\frac{4\gamma k_B n T_c}{R_{TES}}} + \sqrt{\frac{4\gamma k_B n T_c P_{FIR}}{V_{TES^2}}} \end{aligned}$$

The first term is equal to Eq. 16 and the second term is zero if there's no optical loading.

B Additional data

B.1 I/V curves

Figs. 31 to 33 present the I/V responses of pixels 2 to 4 together with the power plateaus in a dark environment for various bath temperatures like in Fig. 19. Lastly, Figs. 34 and 35 presents the I/V measurements from the photon noise experiment of section 7.2, the last one is from Audley et al. 2022. These were necessary to produce the feedback voltage noise spectral density measurements from Fig. 26 at a fixed point in the transition. For the 70 mK measurements, the following was retrieved at 50% R/R_N: (V_{TES} [nV], P_{TES} [fW]) = (40.9, 21.0), (40.9, 20.9), (40.9, 21.0), (40.9, 20.9), (39.5, 19.5), (35.6, 15.8), (33.5, 14.1), (27.1, 9.2), (20.5, 5.3), and (12.6, 2.0) for the given power levels in increasing order. Similarly from the 90 mK data set: (V_{TES} [nV], P_{TES} [fW]) = (29.5, 10.9), (28.9, 10.4), (28.3, 10.0), (27.0, 9.1), (25.0, 7.8), (20.7, 5.4), and (16.4, 3.4).

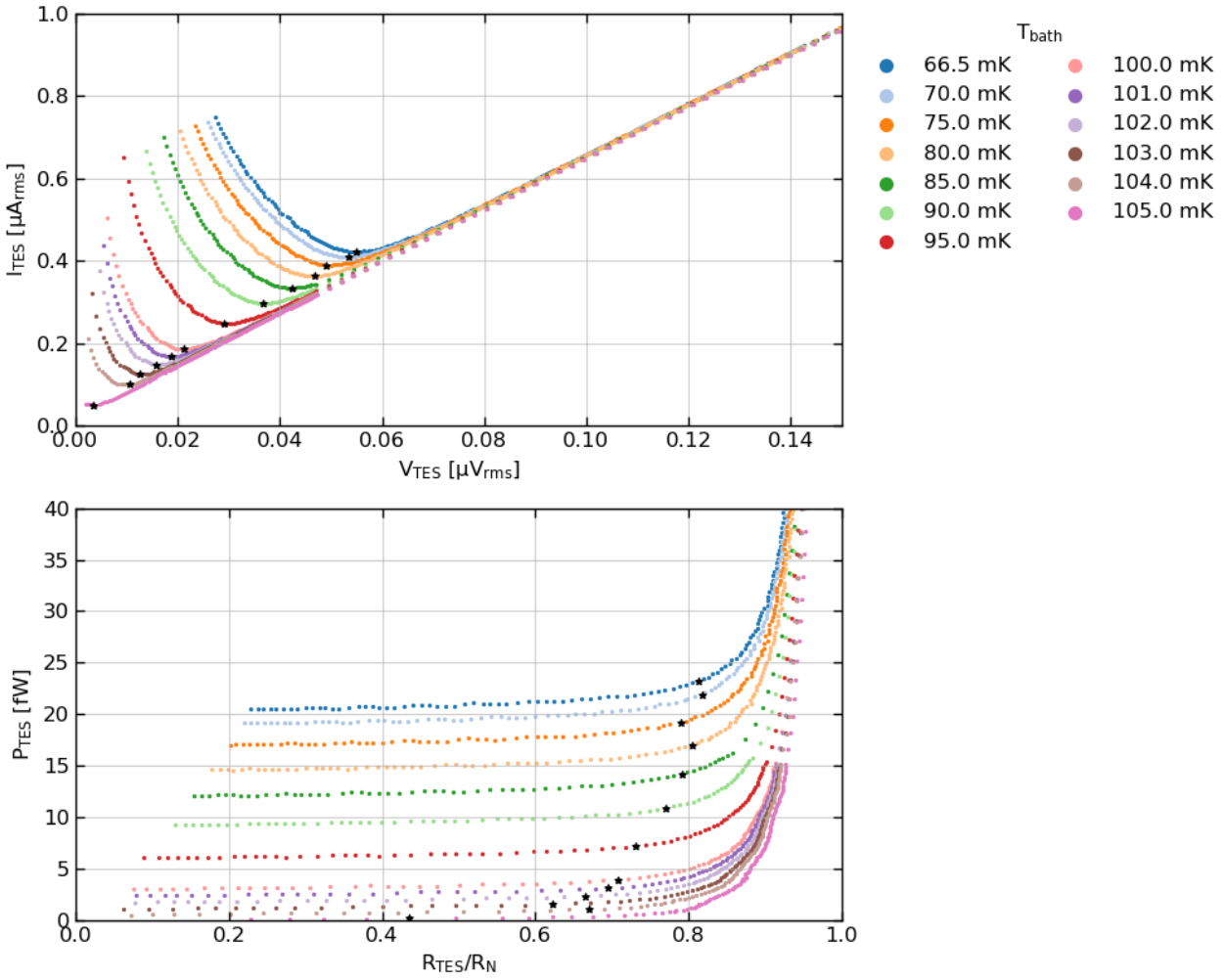

Figure 31: *Pixel 2 current-voltage response and power plateaus for various bath temperatures. The black stars indicate the I/V minima and the corresponding location on the power plateaus. A suppressing magnetic field of 10^{-5} μA was applied. SQUID operating point: (I_b, I_{fb}) = (13.0, 18.0) μA. LNA settings: gain = 5000 and R_{in} = 112.6 Ω. Normal resistance: $R_N = 160$ $m\Omega$.*

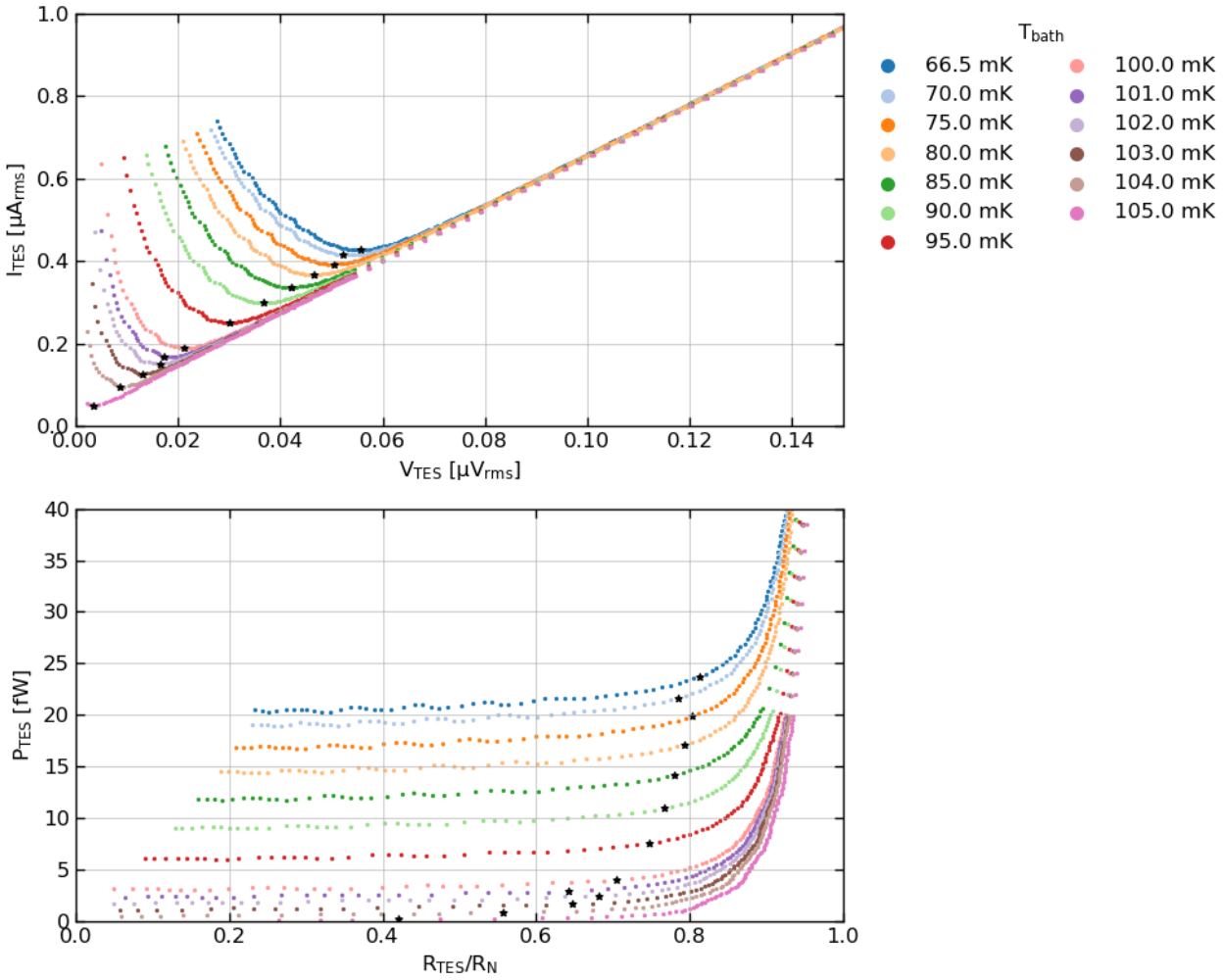

Figure 32: *Pixel 3 current-voltage response and power plateaus for various bath temperatures. The black stars indicate the I/V minima and the corresponding location on the power plateaus. A suppressing magnetic field of 10^{-5} μA was applied. SQUID operating point: $(I_b, I_{fb}) = (13.0, 18.0)$ μA. LNA settings: gain = 5000 and $R_{in} = 112.6$ Ω. Normal resistance: $R_N = 160$ $m\Omega$.*

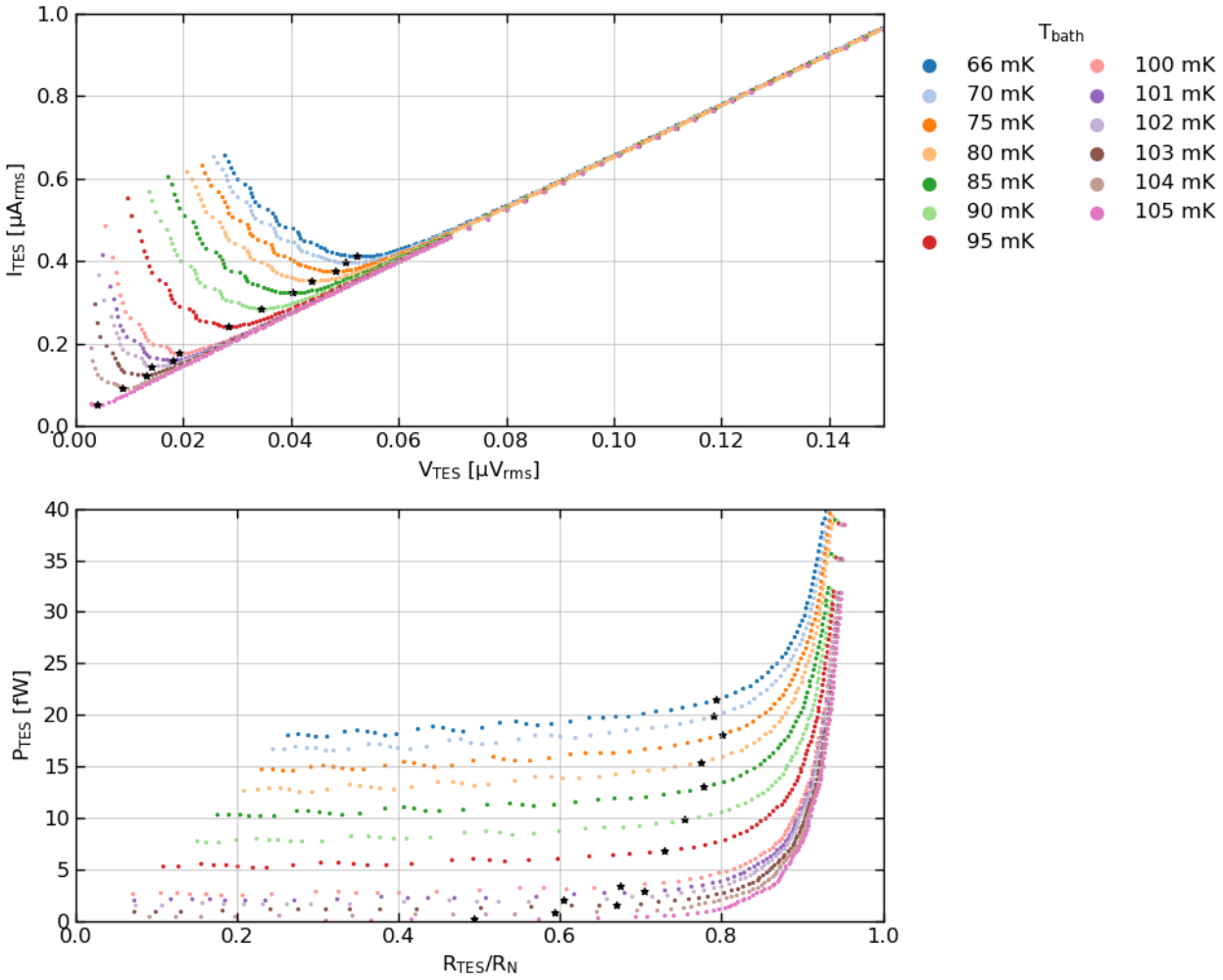

Figure 33: *Pixel 4 current-voltage response and power plateaus for various bath temperatures. The black stars indicate the I/V minima and the corresponding location on the power plateaus. A suppressing magnetic field of 10^{-5} μA was applied. SQUID operating point: $(I_b, I_{fb}) = (13.0, 18.0)$ μA. LNA settings: gain = 5000 and $R_{in} = 112.6$ Ω. Normal resistance: $R_N = 160$ $m\Omega$.*

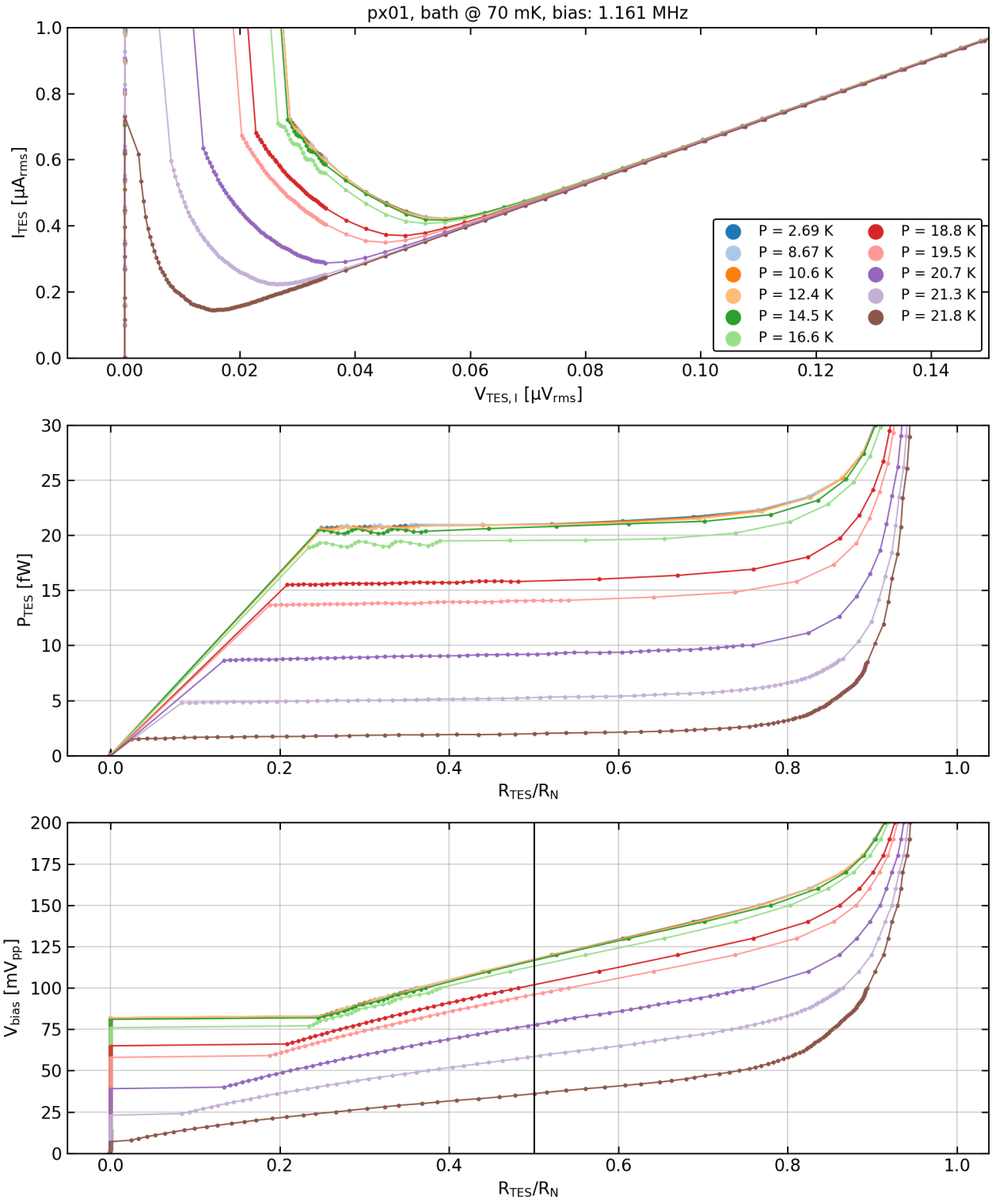

Figure 34: *I/V responses of pixel 1 subject to different levels of optical power loading as provided by the cryogenic blackbody source inside the light cavity of the cryostat. From the power plateaus it can be seen how much optical power is absorbed by the pixel. The bottom figure illustrates how the bias voltage is determined so that the transition location is fixed at 50% R/R_N for different levels of optical loading. SQUID operating point: $(I_b, I_{fb}) = (12.5, 20.0)\ \mu A$. LNA settings: gain = 5000 and $R_{in} = 112.6\ \Omega$. Normal resistance: $R_N = 160\ m\Omega$.*

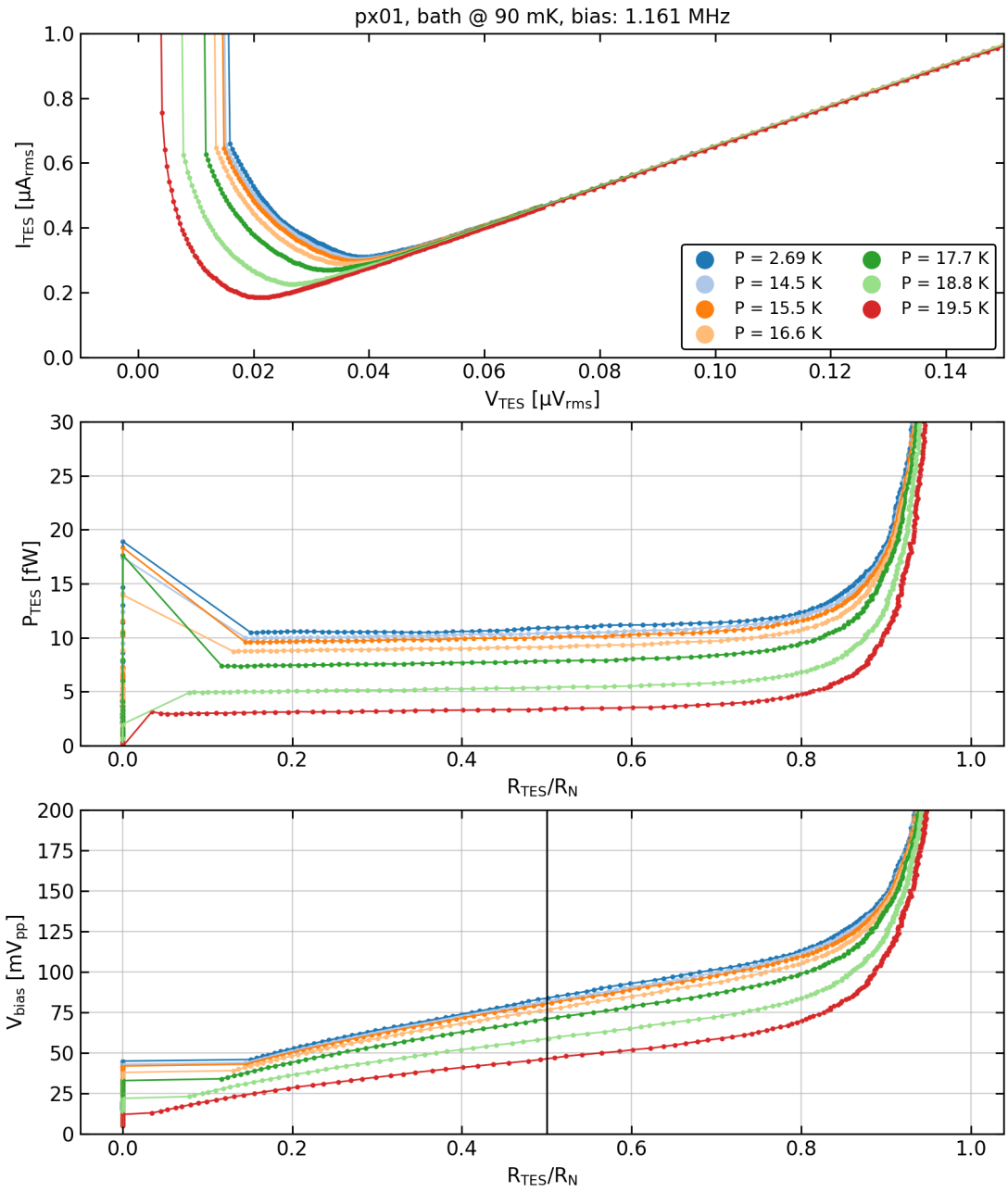

Figure 35: *Same as Fig. 34, but here $T_{bath} = 90$ mK. Data from Audley et al. 2022.*

B.2 Interferogram calibration

This section outlines the measurements performed in order to calibrate the interferograms.

Figs. 36 to 39 show feedback voltage time series at a 1 mm distance from the Michelson interferometer zero-point deflection (ZPD) (with the notable exception for pixel 2 for which the time series is *at* ZPD). From these time series it can be seen how the 25 Hz signal increases the noise level by a factor 20, 28, 23, and 27, respectively, for pixels 1 to 4. The spectra are shown together with the noise time series. From the V_{fb} time series it is possible to calibrate the lock-in output voltage to the corresponding peak-to-peak modulation in the feedback voltage. This is illustrated with the red dots in the time series, indicating the peaks and troughs from which the mean difference is computed. This mean difference gives an accurate result of the modulation of the feedback voltage. Note that the roll-off in the feedback voltage spectra are due to the DEMUX' internal decimation filter. As a reminder, pixel operation during measurements were at 100 mK with bias points at 22 mV, 25 mV, 20 mV, and 14 mV for pixels 1 to 4, respectively. The signal was chopped at 25 Hz between 295 K and 540 K.

C Uncertainty calculations

The general method of uncertainty propagation in this thesis follows the *Gaussian error propagation rule*.

The thermal conductance, G is given by $G = KnT_c^{n-1}$ as written in Eq. 5. The Gaussian variance in the thermal conductance, assuming independence in the variables, is given by

$$\sigma_G^2 = \left(nT_C^{n-1}\sigma_K\right)^2 + \left(KT_C^{n-1}\left[\ln(T_C)n + 1\right]\sigma_n\right)^2 + \left(Kn\left[n-1\right]T_C^{n-2}\sigma_{T_C}\right)^2$$

The TES phonon NEP is given by Eq. 10. Like above, the variance is then as follows:

$$\sigma_{NEP}^2 = \left(\frac{4\gamma k_B T_C G}{NEP}\cdot\sigma_{T_C}\right)^2 + \left(\frac{2\gamma k_B T_C^2}{NEP}\cdot\sigma_G\right)^2$$

The 1σ uncertainties simply follow from the square root of the expressions above.

The total noise equivalent power from Eq. 32 is

$$NEP_{\text{total}} = \sqrt{NEP_{\text{read-out}}^2 + NEP_{\text{phonon}}^2 + NEP_{\gamma}^2}$$

Let $NEP_{floor} \equiv \sqrt{NEP_{\text{read-out}}^2 + NEP_{\text{phonon}}^2}$, the uncertainty in this noise floor value is taken from the least-squares fit. The only uncertainty in the photon noise is the TES absorptivity, η. The Gaussian variance then becomes

$$\sigma_{NEP_{\text{total}}}^2 = \left(\frac{NEP_{floor}}{NEP_{total}}\cdot\sigma_{NEP_{floor}}\right)^2 + \left(\frac{1}{2}\frac{(NEP_{\gamma})^2}{NEP_{\text{total}}}\frac{\sigma_\eta}{\eta}\right)^2$$

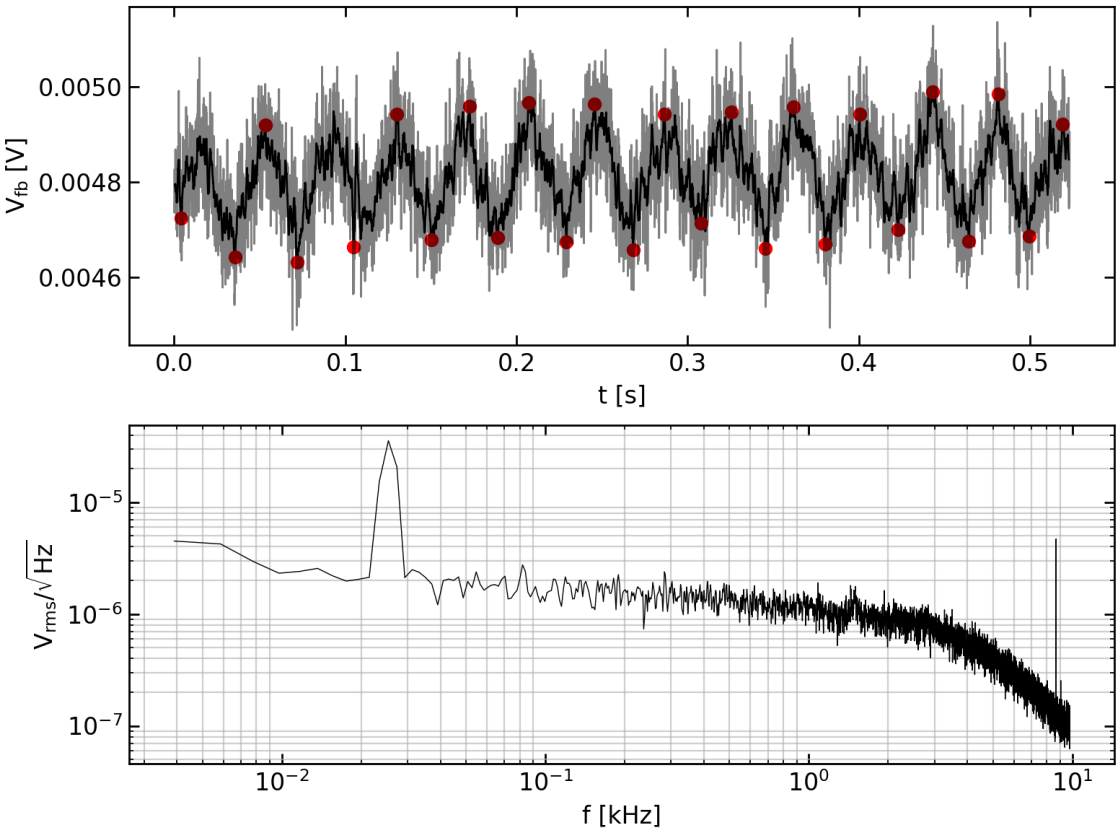

Figure 36: *Pixel 1 feedback voltage response 1 mm from ZPD.* $\Delta V_{fb} = 277\ \mu V$

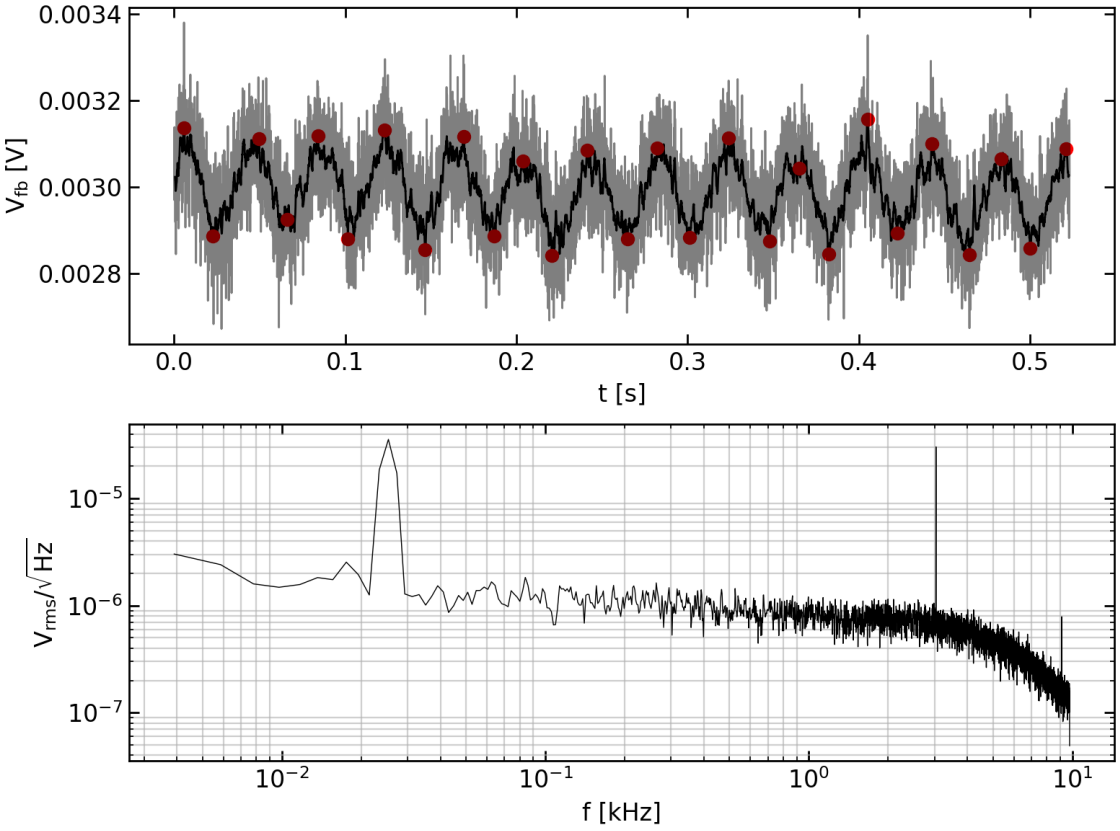

Figure 37: *Pixel 2 feedback voltage response at ZPD.* $\Delta V_{fb} = 228\ \mu V$

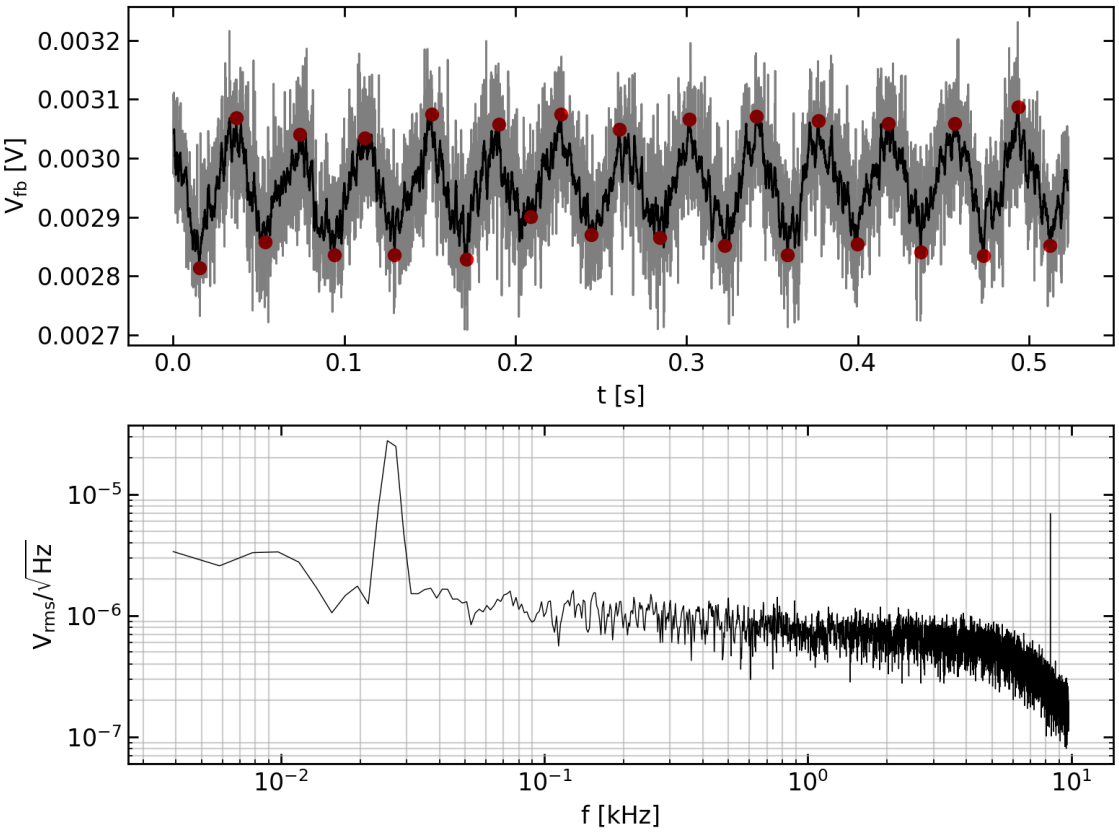

Figure 38: *Pixel 3 feedback voltage response 1 mm from ZPD.* $\Delta V_{fb} = 213\ \mu V$

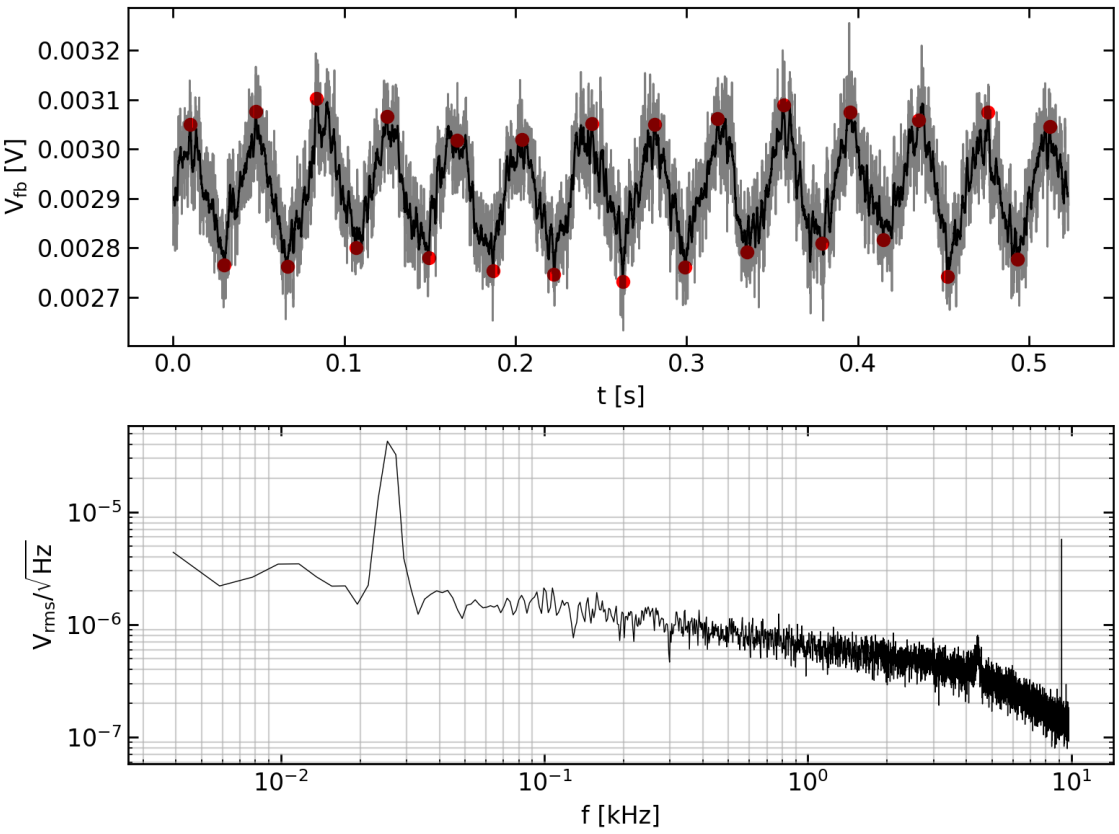

Figure 39: *Pixel 4 feedback voltage response 1 mm from ZPD.* $\Delta V_{fb} = 288\ \mu V$